Magnetic Resonance Rheology on Phantoms and Human Brains

Dissertation

zur

Erlangung des Doktorgrades (Dr. rer. nat.)

der

Mathematisch-Naturwissenschaftlichen Fakultät

der

Rheinischen Friedrich-Wilhelms-Universität Bonn

vorgelegt von

Anna-Lisa Kofahl

aus

Lindlar

Bonn 2016

Angefertigt mit Genehmigung der Mathematisch-Naturwissenschaftlichen Fakultät der Rheinischen Friedrich-Wilhelms-Universität Bonn

1. Gutachter: Prof. Dr. Carsten Urbach

2. Gutachter: Prof. Dr. Karl Maier

Tag der Promotion: 27.01.2017

Erscheinungsjahr: 2017

Contents

Introduction

"Dr. Robert Lerner, a radiologist at the University of Rochester, was intrigued by the ability of palpation to detect some prostate cancers that were undetectable by ultrasound" [1] wrote Parker *et al.* in their review paper on imaging elastic properties of tissue. For Lerner and Parker, this lead to the development of vibration amplitude sonoelastography, one of the earliest techniques for imaging the elastic properties of tissue and imitating manual palpation [2].

Manual palpation, as a means to examine the elastic properties of tissue, has been one of the oldest medical examination techniques used even by physicians in ancient Egypt or Mesopotamia [3] and was also held in high regard by the modern, scientific physicians emerging after the French Revolution: "There was, quite aside from the world of sight, an entire world of touch which we had never perceived before." [4] wrote Karl Stern, a resident physician in Fankfurt even in the early 1930s [5, 6].

In the 1980s an impressive arsenal of medical imaging modalities had emerged: Beginning 1895 with the discovery of x-rays by Röntgen [7] and including the introduction and development of modalities like ultrasound (US) pioneered by Wild in 1949 [8–12], nuclear or molecular imaging, starting in the 1950s and leading to techniques like SPECT (single photon emission computed tomography) and PET (positron emission tomography) [12–15], or CT (x-ray based computer tomography) with its first clinical scanner developed by Hounsfield and EMI Ltd in 1971 [12, 16–18]. In the 1970s and 1980s magnetic resonance imaging (MRI) was developed [19–21] - a technique that is based on the interaction between the nuclear spins in the human body, strong magnetic fields and radio waves. MRI forms a basis for this thesis. All these radiological methods traditionally provide structural (x-ray, CT, MRI, US) or dynamic information (Doppler US, nuclear imaging, measurements with contrast agents, diffusion/perfusion images).

To complement the arsenal of imaging techniques, in the 1980s and 1990s multiple techniques emerged which aimed at measuring also the mechanical properties of tissue and provide an objective, high resolution and sensitive imaging modality that imitated palpation [1, 6, 22]. After early attempts in the 1950s by Oestreicher and von Gierke to study the behavior of human tissue by exciting surface waves [23, 24], now different techniques based on US imaging were investigated [25, 26]. They induce either a dynamic, transient or static strain in the tissue (using mostly external sources or acoustic radiation force) and use different US imaging techniques to measure this strain in order to infer the mechanical properties of the tissue. Some examples include (but are not limited to) the above mentioned vibration amplitude sonoelastography which uses Doppler US to measure the amplitude of low frequency vibration ($20 - 1000\,\mathrm{Hz}$) [2, 27], compression elastography which compares US images before and

after a static compression [28], transient shear wave imaging [29–31], radiation force vibration acustography [32], supersonic shear imaging [33] or acoustic radiation force imaging [34]. In the mid 1990s dynamic magnetic resonance elastography (MRE) emerged, a technique that uses MR phase-contrast to image the propagation of low frequency shear waves [35, 36]. Later other techniques using MR phase-images to investigate the influence of acoustic radiation force were developed [37–40].

Elastography has meanwhile been applied to various clinical issues. Both US and MR elastography show promising results for example in breast and liver examinations, while especially US elastography is also applied to various other areas (including both thyroid and prostate). Overviews of the applications can be found for example in [1, 6, 41–43].

One area, however, where neither manual palpation nor US elastography can be used non-invasively to access the mechanical properties of tissue is the brain since it is protected from most outside influence by the skull. MRE, on the other hand, can give access to the brain's properties [44, 45], and it has been shown that it can deliver interesting insights, for example on the consistency of brain tumors [46–49], multiple sclerosis [50, 51], neurodegenerative diseases [52, 53] or normal pressure hydrocephalus [54, 55].

However, MRE still faces some challenges in the investigation of the brain. On the one hand, multiple approaches and algorithms exist to extract mechanical properties for the tissue [56] and they can yield inconsistent results [57, 58]. Also, studies trying to differentiate different kinds of tissue inside the brain vary in their results for the shear modulus over one order of magnitude [59]. Another challenge concerns the form of the excitation: since the skull protects the brain against direct access, the shear waves measured are typically excited from the outside by vibrating the skull and have to travel inwards through the brain. Brain tissue, however, is a lossy medium [44] which might lead to locally different excitations depending on how strong the waves are attenuated from the outside in and thus may cause different sensitivity in the inner regions of the brain.

The aim of this thesis is to show the feasibility of an alternative method to image the mechanical properties of brain tissue, which we call MR rheology (MRR) [60–62]. In its excitation it is similar to the work done by Bayly *et al.* [63], who use MRI tagging [64] to measure the strain after acceleration of the head to investigate deformations associated with traumatic brain injuries. MRR uses a short fall ($\approx 1\,\mathrm{mm}$) of the human head as a global excitation of the entire brain volume aiming for an equal sensitivity in the inner and outer regions of the brain. The response of the brain tissue to this shock excitation is measured using motion sensitive MR phase imaging. The technical development of this method has been described by Ulucay in [65].

In this thesis first systematic measurements on phantoms and healthy volunteers are presented and means to evaluate the acquired data are investigated. Homogeneous phantoms are used as a model system for the human brain to investigate the response to the shock excitation and to determine the influence of size, stiffness and boundary

conditions of the probe. An oscillation in the phase can be observed in response to the excitation and its frequency allows to distinguish between different phantom configurations. Inhomogeneous phantoms are then measured to learn about the feasibility to resolve substructures using MRR, for example to resolve a cube inside a substrate with different mechanical properties and an edge length of approx. 15 mm. The insights gained from the phantom measurements are then transferred to the measurements of human volunteers to evaluate the experimental set-up under real conditions and the comparability of *in vivo* MRR measurements of healthy brains are.

In chapter 1 the theoretical background for this thesis is explained, including the basic principles of MRI and rheology as well as an introduction to the constitution and mechanical properties of the human brain. The experimental methods used are described in chapter 2: The main principle and the experimental realization of MRR as a creep relaxation experiment are explained as well as the phantom realizations and the measuring protocols for both phantoms and human volunteers and the basic data processing steps. The results of the measurements are shown in chapter 3. This chapter is divided into sections for homogeneous phantoms, inhomogeneous phantoms and the human volunteers. In chapter 4 the results are discussed according to the analysis approach that was applied. Additionally, the technical realizations of these field tests are evaluated.

Some parts of the content of this thesis have been published in [62].

1 Theory

1.1 Magnetic Resonance Imaging

Living tissue consists to $60 - 80\,\%$ of water. Each hydrogen proton contained in the water molecules provides a spin and an associated magnetic moment through which the nucleus interacts with external magnetic fields. By using short radio frequency(RF)-pulses the magnetic moments can be manipulated to emit RF-signals whose magnitude and temporal behavior include information about the environment of the nucleus and thus about the tissue itself. This phenomena is called nuclear magnetic resonance (NMR) and was first discovered by Rabi [66] in molecular beams and later by Bloch [67] and Purcell [68] in liquids and solids respectively. Rabi received the Nobel Prize in Physics in 1944 for his work while Bloch and Purcell shared the prize in 1952. NMR is the basis for the magnetic resonance imaging (MRI) technique developed in the nineteen seventies mainly by Lauterbur, Mansfield and Damadian [19–21]. For their work Lauterbur and Mansfield were awarded with the Nobel prize in Physiology or Medicine in 2003.

The aim of the first part of this section is to give a short overview of the physical principles of NMR - more detailed descriptions can be found for example in the references [12, 69, 70]. Furthermore, the fundamentals of the image generation are described as they are explained for example in references [12, 71–73].

1.1.1 Nuclear Magnetic Resonance

Protons have a nuclear spin $\mathbf{I}$ and a corresponding magnetic moment $\boldsymbol{\mu} = \gamma\,\mathbf{I}$ (gyromagnetic ratio for a proton: $\gamma = 2.675 \times 10^8\,\mathrm{rad\,s^{-1}\,T^{-1}}$). The absolute value of $\mathbf{I}$ can be derived from $|\mathbf{I}| = \hbar\sqrt{I\,(I+1)}$, where I is the nuclear spin quantum number, which is $I = 1/2$ for a proton. From the uncertainty relation follows that not all components of $\mathbf{I}$ can be derived simultaneously, so that the direction of the nuclear spin and, thus, also of the magnetic moment cannot be measured with equal precision. The z-component of the nuclear spin, however, can be defined by $I_z = \hbar\,m_z$, with m_z as the magnetic quantum number which runs in $2\,I + 1$ steps through $-I, -(I-1), ..., +I$. In a magnetic field $\mathbf{B_0} = B_0\,\mathbf{e_z}$ aligned in z-direction the magnetic moment $\boldsymbol{\mu}$ couples to its field and for the potential energy follows

$$E = -\boldsymbol{\mu}\cdot\mathbf{B_0} = -\mu_z\,B_0 = \gamma\,I_z\,B_0. \tag{1.1}$$

Thus, the afore degenerate energy eigenstates are split into $2\,I + 1$ (in the case of the proton into 2) levels (Nuclear Zeemann effect). These levels are associated with the

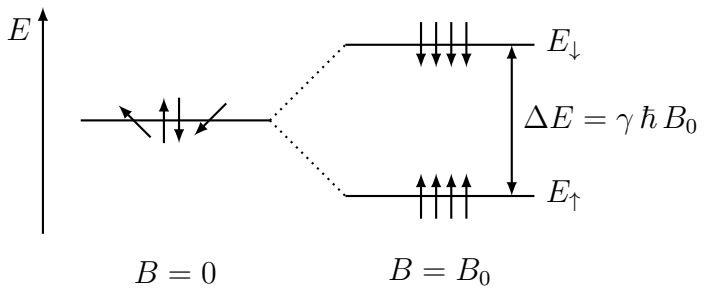

Figure 1.1: *Nuclear Zeemann Effect:*
The orientation of the nuclear spins without a magnetic field is arbratrary and the energy states are degenerated. When a magnetic field is applied the degeneration is suspended and in a proton the energy levels split up into a favorable one where the spins are aligned parallel to the magnetic field ($E_\uparrow$) and one where the spins are aligned anti-parallel ($E_\downarrow$). The difference between these states is given by $\Delta E = \gamma \hbar B_0$.

spin being aligned parallel or anti-parallel to the magnetic field, where the parallel state is energetic favorable: $E_{\uparrow/\downarrow} = \mp\frac{1}{2}\gamma\hbar B_0$ (cf. fig. 1.1). From this follows that the energy difference between these states is:

$$\Delta E = \gamma \hbar B_0 = \hbar \omega_L, \tag{1.2}$$

where ω_L is called Larmor frequency. The relation

$$\omega_L = \gamma B_0 \tag{1.3}$$

is fundamental for NMR since by applying a resonant RF-pulse with the frequency $\boldsymbol{\omega_L}$ transitions between these energy states can be induced.

The number of protons in $1\,\mathrm{mm}^3$ of water is of the order of 10^{20}. According to the Boltzmann statistic the population excess of the energetic favorable state at $T = 310\,\mathrm{K}$ (typical value for a living body) in a magnetic field of $B_0 = 1.5\,\mathrm{T}$ (typical magnetic field in a medical MRI scanner) is in the order of 10^{-5}. Hence, in $1\,\mathrm{mm}^3$ of water there are about 10^{14} more protons aligned parallel to the magnetic field than anti-parallel and it is thus justified to change from the quantum mechanical description to a quasi classical one and sum up the single magnetic moments of a spin ensemble to a quasi classical magnetic moment $\mathbf{m}$. Multiple spin ensembles inside a volume yield a macroscopic magnetization $\mathbf{M} = \sum_i \mathbf{m_i}$ which is a continuous quantity. It follows from quantum mechanical considerations that when the orientation of the z-component of the spin is precisely oriented along the axis of the magnetic field, the orientation of the x- and y-component are completely uncertain so that the magnetization $\mathbf{M}$ precesses about the z-axis with the frequency $\boldsymbol{\omega}_L$. In a reference frame that rotates with the frequency $\boldsymbol{\omega}_L$ $(x', y', z' = z)$ the magnetization $\mathbf{M}'$ becomes a stationary quantity. The component of the magnetization vector $\mathbf{M}$ parallel to the z-axis $\mathbf{M_z}$ ($\mathbf{M'_z}$ in the rotating reference frame) is called longitudinal magnetization and is a measure of

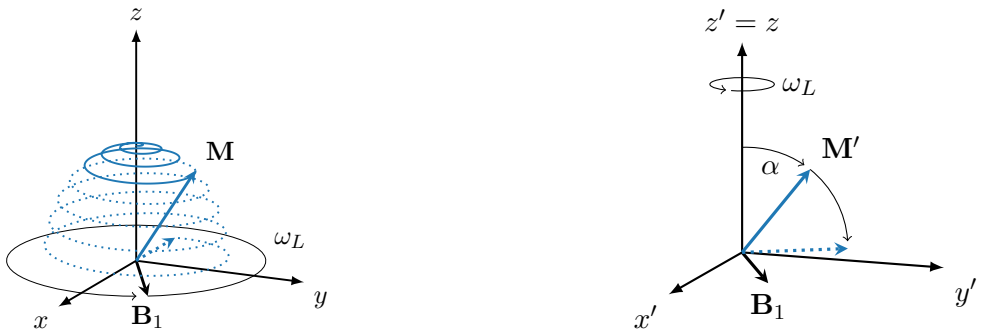

(a) Laboratory frame of reference *(b) Rotating reference frame*

Figure 1.2: *Reference Frames:*
When considering a great number spins, the single magnetic moments with their discrete energy levels add up to a continuous quantity and a macroscopic magnetization $\mathbf{M}$*(*$\mathbf{M}'$ *in the rotating reference frame) can be defined. An RF-pulse moves the magnetization* $\mathbf{M}$*/*$\mathbf{M}'$ *from its equilibrium state aligned to the* z/z'*-axis. In the Laboratory frame of reference (a) the magnetization spirals towards the* $x-y$*-plane. In a reference frame that rotates with* ω_L *(b) the angle* α *between the* z'*-axis and* $\mathbf{M}'$ *increases with the duration and strength of the RF-pulse. [74]*

how many magnetic moments are aligned with the magnetic field. The components $\mathbf{M_x}$ and $\mathbf{M_y}$ are jointly called transversal magnetization $\mathbf{M_T}$ ($\mathbf{M'_T}$ respectively). The transversal magnetization describes the phase coherence of the magnetic moments.

After the magnetization has aligned itself along $\mathbf{B_0}$, the temporal behavior of the magnetization $\mathbf{M}$ can be described by the equation of motion

$$\frac{\mathrm{d}\mathbf{M}}{\mathrm{d}t} = \gamma\,\mathbf{M} \times \mathbf{B}. \tag{1.4}$$

When an RF-Pulse in the form of an additional alternating magnetic field $\mathbf{B_1}$ that rotates with the Larmor frequency is applied in the x-y-direction, transitions between the two energy levels can be induced and the magnetization spirals from its state of equilibrium into the x-y-plane. In the rotating reference frame the magnetization $\mathbf{M}'$ moves towards the x'-y'-plane (cf. fig. 1.2). The longer the time $\tilde{t}$ the transversal field is applied the larger the cone angle α between the z-axis and the magnetization $\mathbf{M}$ becomes:

$$\alpha = \gamma\, B_T\, \tilde{t}. \tag{1.5}$$

An RF-pulse that moves the magnetization from the z-direction into the x-y-plane is called a 90°-pulse. A pulse that flips the magnetization into the $-z$-direction is called a 180°-pulse.

When the magnetization has been moved from its thermal equilibrium, M_z regains its original state $M_z(0)$ through interaction with its surrounding with the rate

$$\frac{\mathrm{d}M_z}{\mathrm{d}t} = \frac{M_z(0) - M_z(t)}{T_1} \tag{1.6}$$

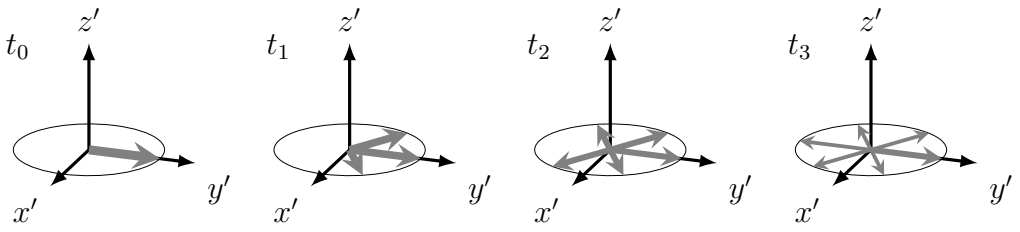

(a) *Decay of phase coherency*

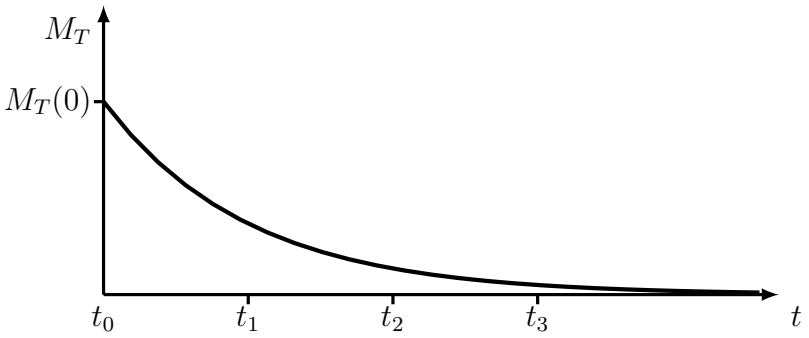

(b) *Exponential decay of transversal magnetization*

Figure 1.3: *Transversal Relaxation:*
(a) Due to locally different magnetic fields, the phase coherency of the transversal magnetization decays. (b) The magnitude of M_T after a 90°-pulse also decays exponentially with the time constant T_2.

where T_1 is the longitudinal (or spin-lattice) relaxation time. Simultaneously to the longitudinal magnetization a transversal magnetization develops when an RF-pulse moves the magnetization from its equilibrium as many magnetic moments perform a precession in phase with the frequency $\boldsymbol{\omega_L}$. However, the phase coherency decays through different local magnetic fields caused by spin-spin-interaction (cf. eq. 1.3, fig. 1.3). The time constant that describes the decay of the transversal magnetization is the transversal relaxation time T_2. Considering these effects one can describe the movement of the magnetization using the Bloch-equations for each component of $\mathbf{M}$ with $\mathbf{B} = B_0\,\mathbf{e}_z + B_1\,(\mathbf{e}_x + \mathbf{e}_y)$

$$\begin{aligned}
\frac{\mathrm{d}\mathbf{M_x}}{\mathrm{d}t} &= \gamma\,(\mathbf{M}\times\mathbf{B})_x + \frac{\mathbf{M_x}}{T_2} \\
\frac{\mathrm{d}\mathbf{M_y}}{\mathrm{d}t} &= \gamma\,(\mathbf{M}\times\mathbf{B})_y + \frac{\mathbf{M_y}}{T_2} \\
\frac{\mathrm{d}\mathbf{M_z}}{\mathrm{d}t} &= \gamma\,(\mathbf{M}\times\mathbf{B})_z + \frac{\mathbf{M_0}-\mathbf{M_z}}{T_1}.
\end{aligned} \tag{1.7}$$

For the longitudinal magnetization after a 90°-pulse (cf. fig. 1.4) follows for example:

$$M_z(t) = M\,(1-\exp(-t/T_1)). \tag{1.8}$$

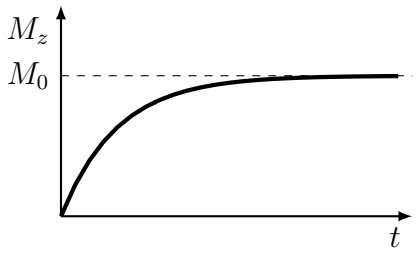

Figure 1.4: *Longitudinal Relaxation: After a 90°-pulse the magnetization is flipped into the x-y-plane, thus rendering the longitudinal magnetization zero. Due to interaction with the surrounding M_z recovers exponentially with the time constant T_1.*

For the transversal magnetization a similar equation can be drawn (cf. fig. 1.3):

$$M_T(t) = M_T(0)\,\exp(-t/T_2). \tag{1.9}$$

Aside from the aforementioned spin-spin-interaction which yield the relaxation time T_2 inhomogeneities of the external magnetic field cause the spin ensembles to lose their coherency. Thus, the decay of M_T proceeds with time coefficient T_2^*, which is always less than T_2:

$$\frac{1}{T_2^*} = \frac{1}{T_2} + \frac{1}{T_{2i}} \tag{1.10}$$

with T_{2i} as the time coefficient for the inhomogeneities.

The relaxation times reflect the surrounding of the spin ensembles and therefore by measuring the times T_1 and T_2 conclusions can be drawn about the composition of the probe. For medical imaging the fact is utilized that different tissues can be distinguished by their relaxation times or by the magnitude of the magnetization as a measure for the proton density (cf. table 1.1).

In order to measure the behavior of the magnetization, an antenna whose surface normal stands perpendicular to the static field can be used. When the magnetization is flipped in the x-y-plane and assumed to rotate there undisturbed with the frequency $\boldsymbol{\omega}_{textbf L}$ a magnetic flux Φ occurs in the antenna. Thus, the flux is proportional to the transversal magnetization $\Phi \propto M_T \cos(\omega_L\, t)$ and a measurable voltage $U(t) \propto M_T\, \omega_L \sin(\omega_L\, t)$ is induced.

To be more precise, considering the transversal magnetization decays with the above mentioned time constant T_2^* (cf. eq. 1.9, 1.10) and simultaneously the longitudinal magnetization builds up again with T_1 (cf. eq. 1.8), the resulting signal in the antenna

Tissue	Proton Density [%]	T_1 [ms]	T_2 [ms]
Liquor	100	>4000	>2000
Gray Matter	70	780	90
White Matter	85	920	100
Meningioma	90	400	80
Metastasis	85	1800	85
Adipose Tissue	100	260	80

Table 1.1: *Relaxation times and proton density for different tissues for $B_z = 1.5\,\mathrm{T}$ [75]*

decays exponentially with T_2':

$$\frac{1}{T_2'} = \frac{1}{T_2} + \frac{1}{T_{2i}} + \frac{1}{T_1}. \tag{1.11}$$

The thus decaying signal after an excitation pulse is called free induction decay (FID).

1.1.2 Tomography

As mentioned before, the aim of MRI is to generate images which give spatial resolved information about the distribution of proton spins and their respective relaxation behavior. MRI is a tomographic imaging technique which means that multiple sections of a volume can be recorded and not just a projection of the whole volume. The word tomography comes from the Greek words $\tau o \mu \acute{\eta}$ (*tome*, "section") and $\gamma \rho \acute{\alpha} \varphi \omega$ (*grapho*, "to write").

In order to achieve this, a single FID is insufficient so that pulse sequences are used for spatial encoding. A sequence consists of a time-ordered set of basically four operations: the transmission of an RF-pulse, the application of a magnetic gradient pulse, the reception of the NMR signal and the use of delays to observe the time dependent development of the spin ensembles.

Some basic sets of operations and sequences are explained in the following.

1.1.2.1 Spin Echo

Due to field inhomogeneities the time constant for the decay of the transversal magnetization is much decreased from T_2 to T_2^* (cf. eq. 1.10). To compensate for this effect a combination of a 90°- and a 180°-pulse can be used to recover some of the signal in a so called spin echo. Its principle is illustrated in fig. 1.5.

After a 90°-pulse is applied at t_0 the spin ensembles that rotate in the x-y-plane will dephase since each ensemble precesses with a different Larmor frequency due to inhomogeneities (cf. eq. 1.3). Thus, after a time $t_1 > T_2^*$ the net magnetization in the transversal plane is much decreased (cf. fig. 1.5a - (t_1)). Suppose a 180°-pulse is applied at a time $T_E/2$ after the 90°-pulse (T_E is called echo time) (cf. fig. 1.5b). Any magnetization in the x-y-plane would be rotated by 180° about the y-axis (cf. fig. 1.5a - (t_2)). Those spin ensembles which have a higher precession frequency and are ahead of the average ensembles by a certain angle are now flipped so that they run behind the average ensembles by the same angle. The same applies for those spin ensembles which are subjected to a slightly lower magnetic field and have gotten behind a certain amount. They are now rotated so they run ahead the average ensemble by the same amount. Since the ensembles do not change their spatial position their respective precession frequency depending on the local field inhomogeneities stays the same. As a consequence, following the 180°-pulse the rapid spin ensembles catch up with the slower ones and at T_E the ensembles refocus again and a transversal magnetization becomes measurable as a spin echo which itself builds up and decays with T_2^* (cf. fig. 1.5a - (T_E)). The maximal amplitude of the echo, however, decays with T_2 due to the irreversible transversal relaxation.

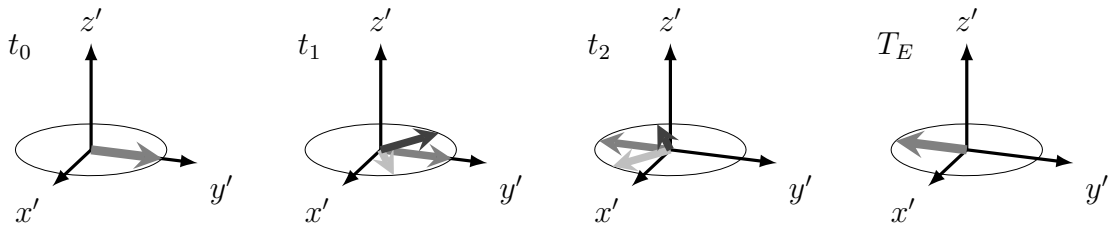

(a) *Spin ensembles during a spin echo*

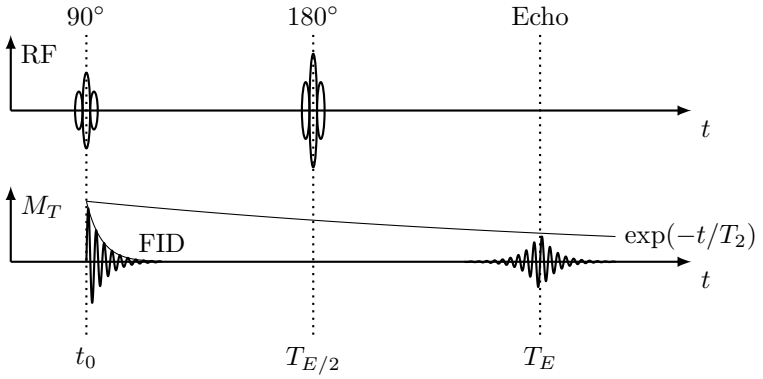

(b) *RF-pulses and transversal magnetization of a spin echo*

Figure 1.5: *Spin Echo:*
After a 90°-pulse the magnetization is turned into the transversal plane and all spin ensembles are in phase (a - t_0). After a time $t_1 > T_2^*$ the coherency is lost since some ensembles rotate with a higher (light gray) and other with a lower (dark gray) frequency than the Larmor frequency. The signal resulting from M_T has decayed. When a 180°-pulse is applied at a time $T_E/2$ the ensembles are flipped along the x'-axis. Now, the faster ensembles run behind and the slower ones run ahead (a - t_2). At the time T_E the ensembles are coherent again and an echo signal from M_T can be measured. The amplitude of the echo declines with T_2 b.

1.1.2.2 Gradient Echoes

By combining a 90°-RF-pulse with a bipolar magnetic gradient a gradient echo is created. When a magnetic field gradient which varies B_0 along one spatial axis (e.g. $G_z = \frac{\partial B_0}{\partial z}$) is superimposed on the static field for a time $T_E/2$ following the 90°-pulse all spin ensembles along the gradient axis have a different precession frequency due to eq. 1.3. Thus, the ensembles dephase and the transversal net magnetization decays to zero even faster than with T_2^*. To restore the transversal magnetization the polarity of the gradient is reversed - again for a time $T_E/2$ - and the spin ensembles catch up with each other until at a time T_E when they are in phase again and an echo is produced. In contrast to the spin-echo-technique, gradient echoes do not compensate for field inhomogeneities and thus the amplitude of the gradient echo decays with T_2^*. In order to use gradient echoes a magnetic field with high homogeneity is needed as well as the

possibility to apply gradients very fast.

1.1.2.3 Selective Excitation

There are different operations to achieve a spatial resolution. One common operation to encode a spatial direction is the selective excitation of a single slice inside the volume. This can be realized by applying a gradient of B_0 in one direction (e.g. in z-direction: $G_z = \frac{\partial B_0}{\partial z}$) simultaneously to an exciting 90°-pulse. The resulting magnetic field in z-direction is now $B' = B_0 + G_z$ and according to eq. 1.3 the Larmor frequency is now dependent on the position of the spin ensemble along the z-axis. Since a typical RF-pulse has a finite bandwidth, the Larmor resonance condition (cf. eq. 1.2 and 1.3) is only satisfied in a certain area along the z-axis. Thus, only spin ensembles in this slice are turned into the x-y-plane and create a signal. The width of the slice is dependent on the steepness of the gradient (a steeper gradient allows for a narrower slice) and on the bandwidth of the RF-pulse. A widely used pulse form is a cropped *sinc*-pulse ($\mathrm{sinc}(x) = \frac{\sin(x)}{x}$) which yields a quasi rectangular slice shape.

1.1.2.4 Frequency Encoding

When a gradient (e.g. in x-direction ($G_x = \frac{\partial B_0}{\partial x}$)) is applied during the signal readout (when an echo is generated) the spin ensembles at different locations along the x-axis will give signals with different frequencies. By analyzing the amplitudes of each frequency in the spectrum of the received signal through a Fourier transformation the amplitude of the signal at each location can be deduced. Thus, space is mapped onto frequency through the gradient.

1.1.2.5 Phase Encoding

Finally, the phase of the received signals can be modulated so that it is dependent on the location. By applying a magnetic field gradient along one axis (e.g. $G_y = \frac{\partial B_0}{\partial y}$) for a time T_y between the excitation and the signal readout each spin ensemble rotates for this time with a different precession frequency that is dependent on its position along the y-axis. After the gradient is turned off a phase angle $\phi(y) = \gamma\, G_y\, T_y\, y$ is retained by each ensemble. Since the received signal is a superposition of the signals of all ensembles, a proper spatial resolution along the y-axis cannot be achieved by applying only one phase encoding gradient. Instead, to achieve a spatial resolution of N pixels along the y-axis N signals with N different gradients G_y need to be received. This way, the amplitude of the signal of each ensemble can be extracted from a linear system of equations.

1.1.2.6 Spin Echo Sequence

In order to generate an image, all three spatial directions have to be encoded. A basic sequence which is not very demanding on the scanner hardware is the spin echo (SE) sequence (cf. fig. 1.6). It consists of a 90°-pulse during which a gradient provides a

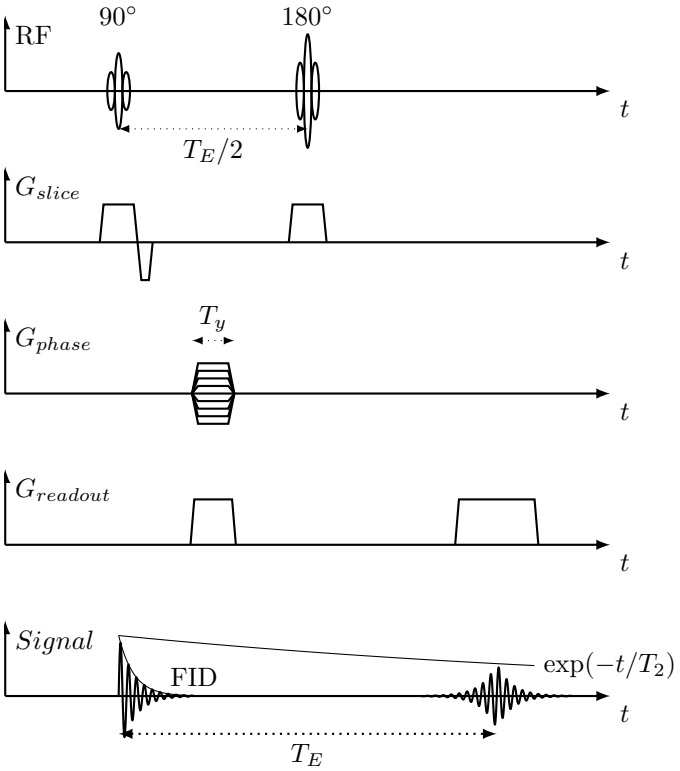

Figure 1.6: *Spin Echo Sequence: During a 90°-pulse a slice selecting gradient is applied. The lobe with opposite polarity and half the area ensures the phase coherency of the transversal magnetization. The 180°-pulse at a time $T_E/2$ generates an echo at a time T_E. During the 180°-pulse a second slice selecting gradient ensures, that only the previously excited spins are flipped. Between the two RF-pulses the phase encoding gradient is applied for a time T_y- at each of the N cycles of the sequence the amplitude is varied in order to generate N phase encoding steps. During the echo signal readout a gradient is used for frequency encoding. [72]*

selective excitation of one slice (cf. sec. 1.1.2.3). As the name suggests, after a time $T_E/2$ a 180°-pulse follows which generates a spin echo at a time T_E (cf. sec. 1.1.2.1) to eliminate magnetic field inhomogeneities. During the 180°-pulse another slice selective gradient is applied in order to only generate a spin echo in the previously excited slice. By means of this 180°-pulse there is more time to apply the phase encoding gradients between the 90°- and 180°-pulse (cf. sec. 1.1.2.5). Finally, during the echo signal readout the frequency encoding gradient is applied to encode the third spatial direction (cf. paragraph 1.1.2.4). Beforehand, a second gradient in the frequency encoding direction can be used to shorten the T_2 time in order to accelerate the sequence. The sequence is repeated with a repetition time T_R with different phase encoding gradients N-times to achieve a spatial resolution in phase encoding direction.

The sequence is relatively slow due to the time consuming phase encoding but on the other hand it is comparatively robust against imaging artifacts.

1.1.2.7 Echo Planar Imaging

An echo planar imaging (EPI) sequence is a gradient echo based imaging sequence (cf. sec. 1.1.2.2) that can image one slice with a single selective excitation 90°-pulse and thus has a very short acquisition time. The FID signal, which decays with T_2^* (cf. eq. 1.10), is modified with a train of bipolar oscillating gradients in the readout direction to create a series of gradient echoes and simultaneously encode the readout direction in the frequency of the signal. In between the echoes an additional gradient

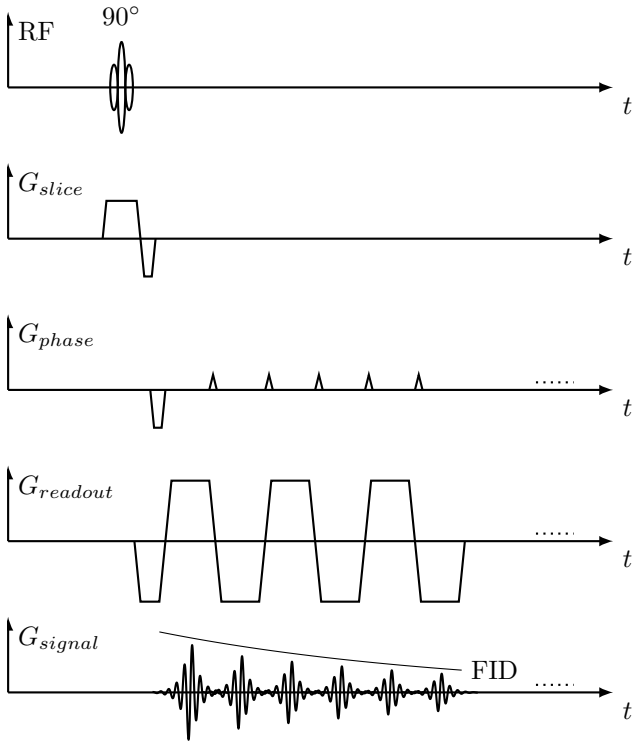

Figure 1.7: *Echo Planar Imaging Sequence:*
A slice selecting gradient is applied during the 90°-pulse. A series of alternating gradient lobes in readout direction generates multiple gradient echoes and also are used for frequency encoding. Between each echo a short phase encoding gradient is applied. Before the first echo, a prephasing gradient in phase encoding direction is used to determine the origin in Fourier space. [72]

in the other spatial direction is applied for phase encoding. The gradients have to be applied fast and precise to ensure that sufficient phase encoding steps are recorded before the signal amplitude has decayed.

1.1.2.8 Motion Encoding

A magnetic field gradient cannot only be used to encode space but also motion in the phase of a signal. This becomes apparent when considering the general relation between a gradient $G(t)$ and the phase ϕ a spin ensemble acquires due to the variation of the Larmor frequency:

$$\phi(t) = \int_0^t \Delta\omega(u)\,\mathrm{d}u = \gamma \int_0^t G(u)\,x(u)\,\mathrm{d}u. \tag{1.12}$$

When gradient moments $m_n(t) = \int_0^t G(u)\,u^n\,\mathrm{d}u$ are introduced, the phase can be expressed in relation to the initial displacement x_0 and velocity v_0 of the ensemble:

$$\phi(t) = \sum_n \gamma \left(m_0\,x_0 + m_1\,v_0 + \ldots + \frac{1}{n!} m_n \left(\frac{\mathrm{d}^n x}{\mathrm{d}t^n} \right)_{t=0} + \ldots \right). \tag{1.13}$$

The zeroth gradient moment m_0 yields the area of the gradient $m_0 = \int_0^t G(u)\,\mathrm{d}u = A$ and thus it becomes clear that a rectangular gradient applied for a certain time can encode the position x_0 of a spin ensemble as described in sec. 1.1.2.5.

In order to encode velocity, the zeroth moment has to vanish. This can be realized by applying two gradient lobes with equal area but opposite polarity as additional velocity encoding gradients. The net area for both lobes is zero but the first moment yields $m_1 = A\,\Delta$ (Δ: time between the beginning of the lobes). Thus, from eq. 1.13 the phase shift can be obtained as

$$\phi = \gamma\, A\, \Delta\, v_0 \tag{1.14}$$

which depends on the - as constant assumed - velocity.

By nulling further gradient moments higher moments of motion can be observed. For example, a gradient with four lobes would encode acceleration when both the zeroth and first moment vanish.

For arbitrary trajectories of spin ensembles with relevant higher moments of motion eq. 1.12 and eq. 1.13 still hold true, however, calculating the trajectory from the phase shift becomes complex.

1.2 Rheology

Rheology is an interdisciplinary area of research with the aim to describe the relation between force and deformation for a multitude of realistic materials. The name rheology originates from the Greek word *ρέω* (*rheo*, "to flow") and it emerged as a independent field around 1928 through the collaboration of Bingham and Reiner combining physics, chemistry, engineering, material sciences and biomechanics. With the emergence of the chemical industry and polymer production it became apparent that the simple models of an ideal elastic solid and an ideal viscose liquid as described by Hooke and Newton respectively are not sufficient and that most materials are much more complex. This led to the need for more complex constitutive equations.

Rheology includes Macro-Rheology with the aim to describe the behavior of materials and to formulate constitutive equations from there and Micro-Rheology with the objective of explaining the observed behavior from the structure of the material. Rheometry as a subfield engages in the task of developing measuring procedures for different classes of materials while the Applied Rheology researches the influence of rheological properties on the processing of materials.

The aim of this section is to introduce some of the basic constitutive equations and models used in rheology to describe more complex materials. It is based on the much more detailed explanations in [76–78].

1.2.1 Basic Constitutive Equations

Before describing more complex material models the two basic models of an ideal elastic solid and an ideal viscose liquid are described.

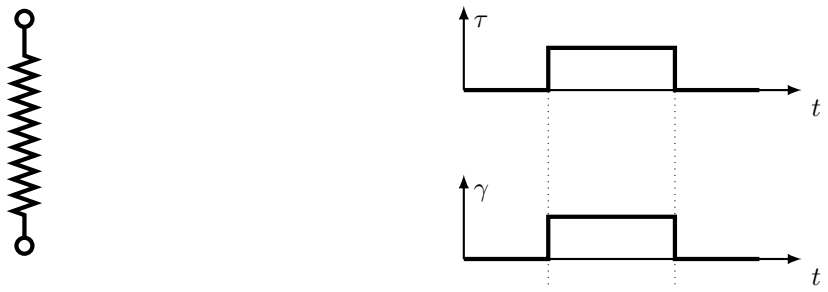

(a) *Hooke Element* **(b)** *Creep Relaxation Experiment*

Figure 1.8: *Elastic Solid:*
An elastic solid can be represented by a spring or Hooke element (a). Under a creep relaxation experiment, where the stress is given in a step function and the strain is observed, in an elastic solid the strain follows the stress immediately to a value that is inversely proportional to the shear modulus. After the stress is removed the deformation is reversed instantaneously (b). [77]

1.2.1.1 Elastic Solid

One of the basic material models is the elastic solid which is characterized by the facts that it can only store energy and that its deformation is instantaneous but finite. When the stress is removed, the solid returns instantaneously to its original state - the deformation is reversible. It can be symbolized as a spring or a Hooke element (cf. fig. 1.8a) and is described by Hooke's law

$$\sigma(t) = E_H \, \epsilon(t), \tag{1.15}$$

where the deformation or strain ϵ is proportional to the normal stress σ. The coefficient E_H is called the elastic or Young's modulus and is a material property. A similar coefficient - the shear modulus G_H - can be defined for a shear stress τ with the shear strain γ

$$\tau(t) = G_H \, \gamma(t). \tag{1.16}$$

Here, the principle holds also true that when a shear stress is applied the strain follows instantaneously and when the stress is removed the strain returns to its original value (creep relaxation experiment, cf. fig. 1.8b). These coefficients for the spring symbol should not be equalized with the coefficients of a real solid (shear modulus G, Young's modulus E and bulk modulus K). For those the relations

$$E = 3\,K\,(1 - 2\,\mu) = 2\,G\,(1 + \mu) \tag{1.17}$$

hold true. μ is here the Poisson's ratio. For incompressible materials where $\mu = 0.5$ and $K = \infty$ this yields

$$E = 3\,G. \tag{1.18}$$

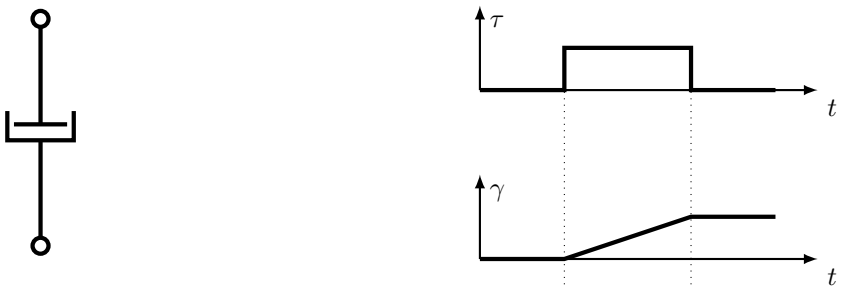

(a) *Newton Element* ***(b)*** *Creep Relaxation Experiment*

Figure 1.9: *Newtonian Liquid:*
A liquid can be symbolized by a Newton element (a). This damper represents the attribute of a Newtonian liquid to dissipate energy and to allow for a delayed strain in a creep relaxation experiment (b). The slope of the strain function is proportional to $1/\eta_N$*. After the stress is removed there remains an irreversible deformation. [77]*

1.2.1.2 Newtonian Liquid

The simplest description of a liquid is given by Newton's law of viscosity

$$\tau(t) = \eta_N \, \dot{\gamma}(t) \tag{1.19}$$

where the shear stress τ is proportional to the rate of straining $\dot{\gamma} = \mathrm{d}\gamma/\mathrm{d}t$. The constant of proportionality η_N is called viscosity and is a measure for the friction in the liquid. In contrast to an elastic solid a Newtonian liquid dissipates energy and, thus, is symbolized by a liquid filled damper or a Newton element (cf. fig. 1.9a). In a viscous material the deformation is delayed with respect to the onset of the stress but unlimited and irreversible (cf. fig. 1.9b).

1.2.2 Viscoelastic Materials

Though these ideal material models are quite successful for a wide range of materials at small strains, there is a wide range of relevant materials that exhibit mixed (for example both elastic and viscous) behavior. They show a time dependent response such as an instantaneous deformation followed by a continuous creeping motion. These materials are called viscoelastic and can be described by a linear superposition of elements that store energy and those that dissipate it. Depending on whether the stresses or the strains are superimposed this yields both viscoelastic fluids or viscoelastic solid.

1.2.2.1 Kelvin-Voigt-Model

The consideration of the superposition of elastic and viscose stresses under a collective strain yields

$$\tau = \tau_H + \tau_N = G_H \, \gamma + \eta_N \, \dot{\gamma}. \tag{1.20}$$

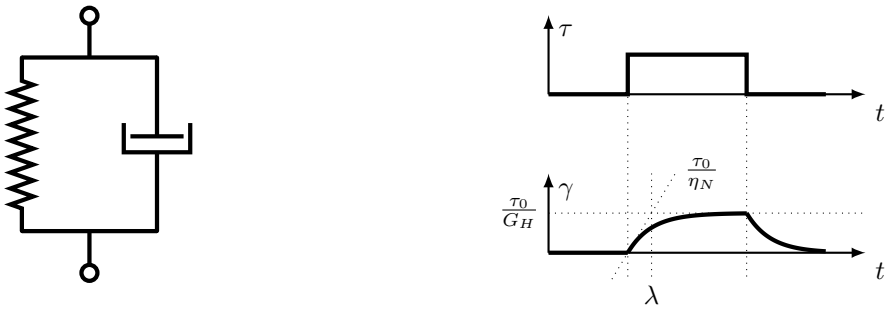

(a) *Kelvin-Voigt Element* ***(b)*** *Creep Relaxation Experiment*

Figure 1.10: *Kelvin-Voigt-Model:*
(a) A Kelvin-Voigt model consists of a spring and a damper in parallel connection. (b) When a stress is imposed the deformation of the spring is slowed down by the damper. For short times $t << \lambda$ a Kelvin-Voigt body acts as a fluid. For longer times it creeps into a steady deformation determined by the Hooke element. When the stress is removed the material recovers through a exponential decay back into its original state. [77]

This is a model for a viscoelastic solid since for a constant strain this equation turns into Hooke's law (cf. eq. 1.16). It can be symbolized by putting a Hooke and a Newton element in parallel, so that both elements suffer the same strain (cf. fig. 1.10a).

Consider a creep relaxation experiment, where an instantaneous stress τ_0 is applied (cf. fig. 1.10b). The spring deforms but is slowed down by the Newton element so that the deformation is not instantaneous but converges to a finite value given by the Hooke element. For a creep experiment the deformation can be deduced from eq. 1.20 to read

$$\gamma(t) = \frac{\tau_0}{G_H}\left[1 - \exp\left(\frac{-t}{\lambda}\right)\right]. \tag{1.21}$$

Here, $\lambda = \eta_N/G_H$ is the retardation time and determines the time response of the material. For long times $t > \lambda$ the Kelvin-Voigt-Model behaves as a solid (cf. sec. 1.2.1.1), for $t << \lambda$ as a fluid (cf. sec. 1.2.1.2).

When the external stress is removed the material returns from a deformation $\gamma_0 = \tau_0/G_H$ into its original state - the deformation is reversible:

$$\gamma(t) = \gamma_0 \exp(-t/\lambda). \tag{1.22}$$

1.2.2.2 Maxwell-Model

The Maxwell model is the connection of a Hooke and a Newton element in series (cf. fig. 1.11a), this means that both elements experience the same stress and the deformations are superimposed resulting in the constitutive law

$$\dot{\gamma} = \dot{\gamma_H} + \dot{\gamma_N} = \frac{1}{G_H}\dot{\tau_N} + \frac{1}{\eta_N}\tau. \tag{1.23}$$

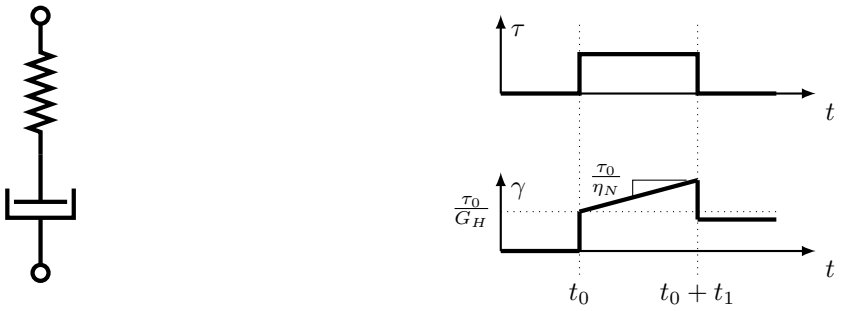

(a) *Maxwell Element* ***(b)*** *Creep Relaxation Element*

Figure 1.11: *Maxwell Model:*
(a) A Maxwell model consists of a spring and a damper in serial connection. (b) When a stress is applied, the spring deforms instantaneously while the damper moves delayed. When the stress is removed only the deformation due to the spring in reversed. [77]

For a constant stress this turns into Newton's law (cf. eq. 1.19). This means that a Maxwell material behaves as a viscoelastic fluid since due to the Newton element the deformation is infinite and irreversible. The Hooke element provides the possibility of an instant deformation while the Newton element reacts delayed. When the stress is removed, the deformation due to the Hooke element is reversed instantaneously while the built-up deformation due to the Newton element remains (cf. fig. 1.11b). The behavior of the Maxwell-model under a creep-recovery experiment can be described by

$$\gamma(t) = \frac{\tau_0}{G_H} + \frac{\tau_0}{\eta_N}\, t. \tag{1.24}$$

1.2.2.3 Voigt-Maxwell-Model

It is also possible to combine three or more elements. With an additional Newton element (cf. sec. 1.2.1.2) put into series with a Kelvin-Voigt model (cf. sec. 1.2.2.1) it is already possible to describe a more realistic fluid with retarded elasticity (cf. fig. 1.12). Here, the principle of linear superposition yields the following equations for the single Newton element and the Kelvin-Voigt element, respectively

$$\begin{aligned} \tau &= \eta_1\, \dot{\gamma_1}, \\ \tau &= \eta_2\, \dot{\gamma_2} + G_H\, \gamma_2. \end{aligned} \tag{1.25}$$

The deformations are added to the total deformation $\gamma = \gamma_1 + \gamma_2$.

1.2.3 Plastic Behavior

In order to describe irreversible plastic deformation a third element aside from the Hooke and the Newton element is introduced: the St.-Venant element (cf. fig. 1.13). It is symbolized by a sliding block which cannot be moved until the static friction

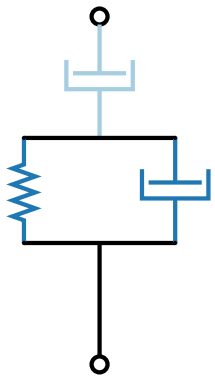

(a) *Voigt-Maxwell Element*

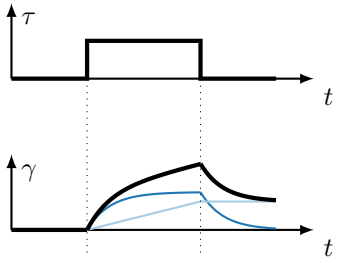

(b) *Creep Relaxation Experiment*

Figure 1.12: *Voigt-Maxwell Model:*
(a) A Voigt-Maxwell fluid can be represented by the serial connection of a Newton element (light blue) and a Kelvin-Voigt element (dark blue). (b) In a creep relaxation experiment the strains of the two elements can be superimposed to receive the complete strain function of the Voigt-Maxwell element (black). [77]

is overcome. More precisely, for a stress smaller than a yield stress $\tau < \tau_y$ there is no deformation while for $\tau \geq \tau_y$ the material flows readily and the deformation is irreversible. Hence, an ideal plastic material acts as a rigid body for stresses below the yield stress and otherwise like a liquid with infinitesimal viscosity.

A St.-Venant element can also be put in connection with a Hooke or a Newton element. Put into a series connection with a Hooke element, it describes an elastoplastic solid that shows - like many real material like steal - an elastic behavior up to τ_y and then a plastic deformation. This is called a Prandtl-Reuß element (cf. fig. 1.14).

It remains to note, that the Prandtl-Reuß-element is only a model for elastoplastic of zeroth order since most materials (also steel) show the phenomenon of a strengthening due to plastic deformation, the so called work hardening. This means that the material does not begin to simply flow (parallel part of the stress strain relation in fig. 1.14b) but since the material hardens during the deformation the stress strain relation has still a finite but continuously changing slope.

Figure 1.13: *St.-Venant Model:*
Plastic behavior can be represented by a sliding block. Until a yield stress τ_y is overcome it behaves as a rigid solid. For $\tau \geq \tau_y$ it flows readily and deforms irreversibly. [77]

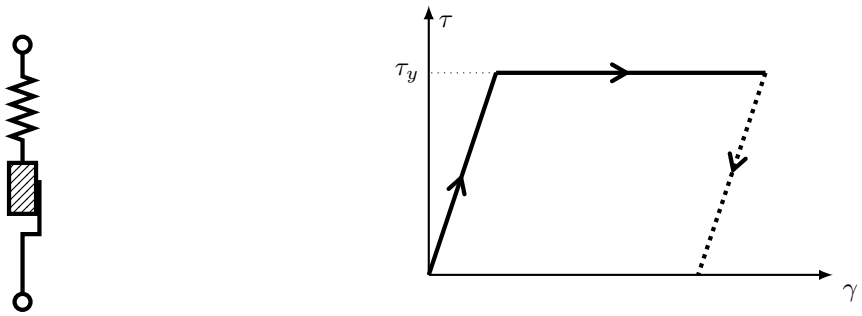

(a) Prandtl-Reuß Element *(b) Stress Strain Relation*

Figure 1.14: *Elastoplastic Solid:*
A serial connection of a Hooke and a St.-Venant element is called a Prandtl-Reuß element and represents a elastoplastic material. Up to the yield stress τ_y it behaves like a solid where the stress is proportional to the strain. When the yield stress is reached the material begins to flow and deforms plastically. [77]

In a similar fashion the Bingham fluid can be conceived. Here, a St.Venant element is put in a parallel connection with a Newton element adding up to a viscoplastic behavior of a fluid that only starts to flow after the yield stress is overcome (like tooth paste or mayonnaise).

For a good description of most realistic materials usually even more complex connections of three or more elements are necessary. Elastoplastic materials for example show a finite deformation and strain hardening for $\tau \geq \tau_y$. This can be modeled by putting a second Hooke element in parallel connection to a Prandtl-Reuß element. With the convention that parallel connection means a superposition of stresses and a series connection a superposition of strains a multitude of complex material models can be created. However, it has to be kept in mind that the here introduced material models are part of a linear theory and can also be expanded to include non-linear relations between stress and strain.

1.2.4 Dynamic modulus

Creep-recovery experiments where the effect of a given stress is observed are merely one of several experimental arrangements to measure viscoelastic properties. Relaxation experiments where the deformation is given or experiments with a given deformation velocity are also common. Measuring the appropriate variables leads to the corresponding moduli. Another approach is to use an oscillating deformation

$$\gamma = \hat{\gamma} \sin(\omega t) \tag{1.26}$$

and to measure the phase difference between strain and stress (cf. fig. 1.15). For a Hooke element the stress follows an imposed strain instantaneously and both oscillate in phase:

$$\tau_H = G_H \hat{\gamma} \sin(\omega t). \tag{1.27}$$

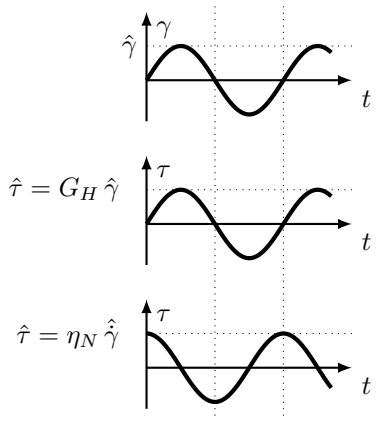

Figure 1.15: *Dynamic Modulus:*
For an oscillating strain excitation $\gamma(t)$ (upper panel) the stress of a Hooke element $G_H\,\gamma(t)$ follows the strain in phase (middle) while for a Newton element the stress $\eta_N\,\gamma(t)$ is shifted by $\pi/2$ (lower). [77]

For a Newton element on the other hand the stress is - according to eq. 1.19 - proportional to the strain velocity $\dot{\gamma}$, thus yielding for the stress a phase difference of $\pi/2$

$$\tau_N = \eta_N\,\dot{\gamma} = \eta_N\,\omega\,\hat{\gamma}\,\cos(\omega\,t) = \eta_N\,\omega\,\hat{\gamma}\,\sin\left(\omega\,t + \frac{\pi}{2}\right) = \hat{\tau}\,\sin\left(\omega\,t + \frac{\pi}{2}\right). \quad (1.28)$$

The behavior of a viscoelastic material can be deduced likewise (cf. fig. 1.16), for example for the Kelvin-Voigt-model from eq. 1.20 with the complex modulus $G_K^* = G_H + i\,\omega\eta_N$:

$$\tau = G_H\,\hat{\gamma}\,\sin(\omega t) + \eta_N\,\omega\,\hat{\gamma}\,\cos(\omega t) = \hat{\gamma}\,|G_K^*|\,\sin(\omega t + \delta_K). \quad (1.29)$$

The phase difference δ_K between stress and strain depends on the ratio between viscosity and shear modulus

$$\delta_K = \tan^{-1}\left(\frac{\omega\,\eta_N}{G_H}\right). \quad (1.30)$$

In a similar way a complex modulus can be defined for a general viscoelastic material. Here, a frequency depending storage modulus $G'(\omega)$ for the elastic component and

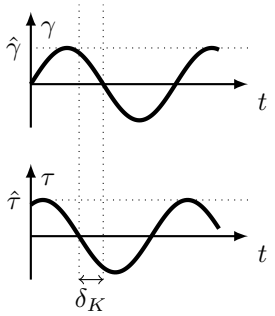

Figure 1.16: *Dynamic modulus for Kelvin-Voigt Element:*
The phase shift δ_K between strain and stress is determined by the ratio between Newtonian viscosity and Hooke shear modulus. [77]

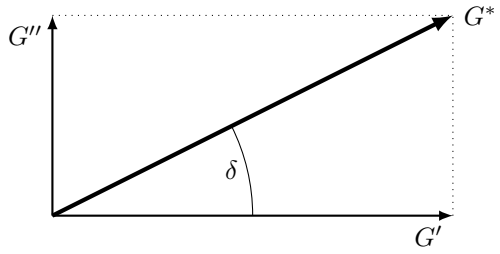

Figure 1.17: *Complex Shear Modulus: For arbitrary viscoelastic materials a frequency depending complex modulus $G^*(\omega)$ can be defined. The phase shift δ describes the ratio between storage and loss modulus $G'(\omega)$ and $G''(\omega)$. [77]*

a loss modulus $G''(\omega) = \eta(\omega)\,\omega$ for the energy dissipating viscose component can be defined. By measuring the frequency dependence between stress and strain (cf. eq. 1.29)

$$\tau = \hat{\gamma}\,|G^*(\omega)|\,\sin(\omega t + \delta) \tag{1.31}$$

the phase shift δ can be obtained and from it the relation between storage and loss modulus (cf. fig. 1.17)

$$\delta(\omega) = \tan^{-1}\left(\frac{G'(\omega)}{G''(\omega)}\right). \tag{1.32}$$

1.3 The Human Brain

The brain as part of the central nervous system is in many aspects one of the most complex and also one of the most important organs of the human organism. The brain tissue itself is also one of the most sensitive organs with its texture resembling a stiff pudding [79, 80], which is why it is specially protected inside the skull through several layers of connective tissue. In this section a brief overview of the anatomy of the brain is given with a focus on its coupling to the skull.

The second aspect of this section is to describe some hitherto existing methods to measure and to model the mechanical properties of brain tissue.

1.3.1 Anatomy of the human brain

Together with the spinal cord the brain forms the central nervous system. The brain itself can be divided from a developmental point of view into five parts (cf. fig. 1.18):

- the myelencephalon (or medulla oblongata which connects the brain to the spinal cord)
- the metencephalon (consisting of the cerebellum ("little brain") and the pons)
- the mesencephalon ("midbrain", first part of the brain stem)
- the diencephalon ("interbrain", with the thalamus and hypothalamus)

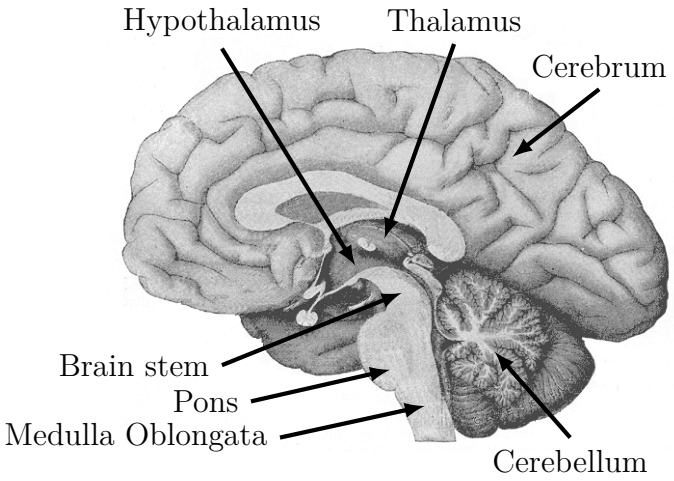

Figure 1.18: *Human brain with characteristic structures. [81]*

- and the telencephalon or cerebrum (consisting of the cerebral cortex as well as subcoratical structures like the hippocampus).

The cerebrum is divided into two hemispheres and folds characteristically into gyri (elevations) and sulci (depressions) in order to increase its surface. The surface of the hemispheres - called the cerebral cortex - consists of an accumulation of neuronal cell bodies which process signals (gray matter). Gray matter can also be found in the inside of the cerebrum as nuclei (e.g. the hippocampus) or in the diencephalon (e.g. in the thalamus and hypothalamus). The bulk of the cerebrum is white matter, which is composed of nerve fiber tracts which relay the signals from the cortex and the nuclei. Aside from neuronal cells the brain tissue consists of about ten times more glia cells which support and protect the neuronal cells and fulfill further tasks. Further information about the anatomy of the human brain can be found for example in the references [82, 83].

1.3.1.1 Meninges and Cerebrospinal Fluid

The brain is surrounded by several membranes, the meninges (cf. fig. 1.19). The outermost layer is the dura mater made of dense, tough connective tissue, which is firmly connected to the skull. The dura mater forms also septa - dividing layers - which run deep into the inside of the skull, for example between the hemispheres of the cerebrum (falx cerebri) or separating the cerebrum from the cerebellum (tentorium cerebelli). The dura mater stabilizes the soft brain tissue. The pia mater - a very flimsy and sensitive membrane - lies directly on the brain tissue and follows all elevations and depressions of the brain. Between the dura and the pia mater lies the arachnoidea. It is a spiderweb-like and thin membrane which lies on the dura mater but is not tightly connected to it. The space between the pia mater and the arachnoidea is called subarachnoid space and is traversed by arachnoid trabeculae - formed from collagen

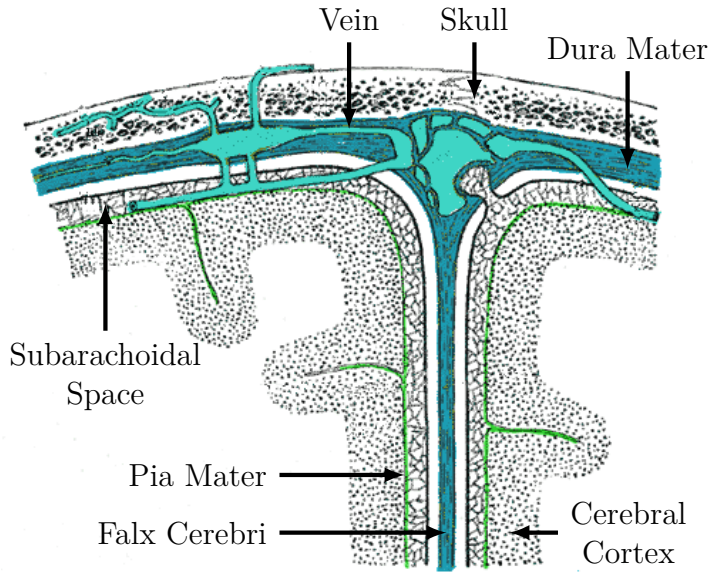

Figure 1.19: *Meninges of the Human Brain:*
The brain (here the cerebral cortex) is protected by the skull and several layers of meninges as well as by the CSF flowing in the subarachnoidal space. [81]

and fibroblast fibers - connecting the pia mater and thus the brain to the arachnoidea and preventing excessive motion of the brain in relation to the skull.

The subarachnoid space itself is filled with cerebrospinal fluid (CFS), thus, resembling a biphasic structure [84] which acts as an additional mechanical protection of the brain against e.g. jolts. CFS is also found in the ventricular system - a set of four interconnected cavities deep inside of the brain. Here, the CFS is produced - daily about 500 ml. The CFS circulates from the ventricles to the subarachnoid space where it is reabsorbed, so that at a given point of time there are about 30 ml of CFS inside the ventricle system and about 120 ml in the subarachnoid space. The CSF in the ventricle system serves primarily as a stabilization of the brain from the inside. Since the brain - so to speak - floats in the CFS its effective weight is reduced from an actual weight of approx. 1500 g to about 50 g with which it presses against the skull [85].

1.3.2 Mechanical Properties of Brain Tissue

Measuring the elastic properties of brain tissue and characterizing it has been an active area of research since the middle of the last century. In the 1950s first experiments where done on mammals before in 1969 Fallenstein *et al.* and in 1970 Galford and McElhaney did first *in vitro* experiments on human brain [86, 87].

Since then a multitude of different rheological experiments on animal and human brain tissue have been conducted [59, 88]. However, due to a large disparity in experimental protocols and results (Chatelin *et. al* mention that the scatter of results for the shear modulus can be as high as 10-20 times from the mean) it remains difficult to clearly characterize the mechanical properties of brain tissue [59, 84]. One issue with comparing results from different studies comes from the fact that when using different experimental set-ups different mechanical properties are measured (like shear, compression or relaxation modulus) and the relation between these parameters depends

Tissue	Density [g cm^{-3}]
CSF	1.007(9)
Gray/White Matter	1.081(3)
Dura Mater	1.133(10)
Pia Mater & Arachnoidea	1.171(77)

Table 1.2: *Density for different brain tissues [95]*

highly on the underlying material model (regarding for example homogeneity, isotropy or incompressibility). Also, when comparing results of different studies for the same mechanical parameters like storage and loss moduli (cf. 1.2.4), they can vary in the order of magnitude, since effects of preconditioning, boundary conditions or sample size can influence the results as well.

In order to overcome some of the challenges presented with *in vitro* measurements efforts are made to measure the mechanical properties of human brain tissue *in vivo*. One approach is to perform rheometry on the open brain during surgery [89, 90]. These highly invasive techniques are, however, not suitable for scientific research.

A non-invasive *in vivo* method to measure elastic properties of human tissue is magnetic resonance elastography (MRE) which has emerged in the 1990s [35]. It uses MR phase imaging to measure the propagation of induced shear waves through tissue in order to calculate its mechanical properties and is an active field of research - an overview can be obtained for example from the references [42, 43]. MRE is also used for brain examinations [44, 45], where the motion is induced by various external actuators (for example head cradles [91], bite bars [92, 93] or the MR table [94]) or by the intrinsic blood vessel pulsation [57].

1.3.2.1 Overview of Mechanical Properties in Literature

Even though precise values for the mechanical properties of brain tissue cannot be given, there is a consent in the literature that for strains inside the linear viscoelastic limit (in the order of $0.1 - 0.3\%$, though a limit of up to 1% can also be found in the literature) brain tissue is a very soft solid material with a complex shear modulus in the order of a few kilopascal, with the storage modulus G' being larger than the loss modulus G'' (cf. sec. 1.2.4). In the linear range the shear modulus increases with the loading frequency following a power-law. Beyond that regime the shear modulus decreases with applied strain. A broader overview can be found for example in [59, 84, 88].

There are indications for variations in the shear modulus of gray and white brain matter as well as for regional variations within the brain, though these differences are not very large [43, 45, 84, 92].

Brain tissue can with good approximation be assumed to be incompressible ($\mu \approx 0.5$) [96] and has a density of about $1\,\mathrm{g\,cm^{-3}}$ with the meninges being slightly denser than the CSF and white and gray matter (cf. table 1.2) [95]. As an example for values for the shear modulus, different MRE studies yield values between 1 to 13 kPa [43].

1.3.2.2 Mechanical Models of the Human Brain

In order to interpret the results from different measuring techniques as well as for the use in computer simulations a constitutive model for brain tissue is needed. However, since brain tissue shows a very complex, non-linear viscoelastic behavior it is not easy to find a model that captures all the responses to different loading rates and types or a wide range of strain rates.

In the literature, different types of models are used which often depend also on the application. A widely used approach are non-linear hyperelastic models like the Odgen model combined with a linear viscoelastic relaxation modulus or special cases of the Odgen model for incompressible materials like the Mooney-Rivlin or neo-Hookean model [84]. Also multi-mode Maxwell models (cf. sec. 1.2.2.2) are used to simulate non-linear viscoelasticity [97]. They try to capture the behavior of brain tissue during larger deformations like in traumatic brain injuries but also the response of brain tissue in small areas in neurosurgical simulations. In MRE, often linear elasticity models are used [56, 57, 98, 99], but also other models are investigated, for example poroelasticity [57, 100], which is also proposed for studying slow, large deformations (like hydrocephalus) [96].

2 Methods

The aim of this chapter is to explain the experimental methods, called magnetic resonance rheology (MRR), used in this thesis. At first, the basic measuring technique is introduced - a creep relaxation experiment after a shock excitation inside an MRI machine [60, 61, 65] - used to investigate the rheological properties of samples like the human brain *in vivo* or tissue mimicking phantoms. Afterwards, the details of measurements of human subjects and the properties and production of tissue mimicking phantoms are explained, before at last the basic steps of data processing are presented.

2.1 Creep Relaxation Experiment in the Brain

In this section the concept and implementation of an *in vivo* creep relaxation experiment for the human brain is presented. The concept can be explained in a gedankenexperiment, before the actual set-up of the experiment is described.

2.1.1 Main Principle

In this thesis a non-invasive creep relaxation experiment after a shock excitation is performed *in vivo* on a human brain while the subject lays in an MRI machine, which is used to observe the response of the tissue. The main principle can be drawn from a gedankenexperiment which is illustrated in figure 2.1:

Consider a head, where the hard skull (dark blue) encloses the brain (cf. fig. 1.19). The brain tissue can be envisioned as a viscoelastic material - in the case depicted in figure 2.1 as a Kelvin-Voigt material (cf. sec. 1.2.2.1) - coupled to the skull. Different volume elements of the brain (light blue and green cubes) can have different mechanical properties represented by different springs and dampeners. For a head at rest at a small height ΔH the gravitational force F_G and the inner restoring forces are in equilibrium and no net force is acting on the system (left). Now the center of mass reference frame of the head is considered. When the head is dropped, the gravitational force is reduced - in the case of a free fall even reduced to zero (middle) - while the inner forces remain. Therefore, the equilibrium of forces is disturbed and the volume elements suffer an acceleration. Since the inner forces depend on the local viscoelastic properties and the coupling of the volume elements to each other and to the skull, the rate of acceleration consequently reflects upon those properties. When the head has landed (right), the gravitational force acts again, and consequently, the brain tissue relaxes back into its original state - each volume element once again on a trajectory determined by the local material properties.

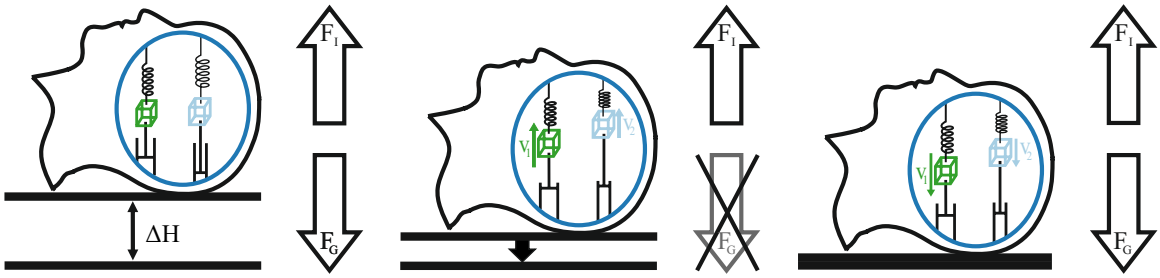

Figure 2.1: *Creep Relaxation Experiment in the Brain:*
The main principle of the method used in this thesis can be explained with the help of a gedankenexperiment of a creep relaxation experiment.
On the left, a head at rest lifted to a height ΔH is considered. The hard skull (dark blue) encloses the brain tissue, symbolized by different Kelvin-Voigt elements (light blue and green cubes) representing volume elements of the brain with different viscoelastic properties. As long as the head is at rest, the inner restoring forces F_I are in equilibrium with the gravitational force F_G.
In the middle, the head is considered during a free fall, so that in the center of mass reference frame of the head, F_G vanishes. This leads to an acceleration of the brain tissue, where each volume element is accelerated depending on the local distribution of F_I. Since the inner forces depend aside from the boundary conditions on the local viscoelastic properties, the trajectory of each volume element under the influence on F_I reflects upon those properties.
On the right, the head has landed and - remaining in the center of mass reference frame - F_G acts again. Consequently, the brain tissue tries to move back into its original state, each volume element once again on a trajectory determined by the local material properties.

To image the thus induced motion of each volume element inside the brain, a motion encoding MRI sequence (cf. sec. 1.1.2.8) is used.

Since in reality both the mass and the inertia of the brain factor into the response of the system, the response will be complex. The changes of the forces during the short time at the beginning of the fall and during the landing excite oscillations with a broad band of frequencies. Since the brain tissue as a viscoelastic medium possesses dampening properties, all but the resonance frequencies of the system (which will depend on its elastic properties and the boundary conditions) will quickly die out (cf. spring pendulum).

2.1.2 Experimental Setup

One challenge of the proposed method is the realization of such an excitation inside the head coil of a clinical MRI machine under the consideration of three aspects: First of all, the experiment has to be safe and feasible for human subjects. That means for example that the accelerations must be restricted to an acceptable level. Secondly, the setup has to be compatible with the high magnetic field and the RF-pulses of an MRI and must not disturb the imaging quality. Consequently, the materials that can be used

for the setup are limited to materials that are not magnetic and have a low electrical dissipation factor. And finally, there should be no structural changes to the MRI system which means particularly that the setup had to be integrated into the existing space of the head coil which is limited. Accommodating these requirements the experiment shall yield reproducible data from which differences in the viscoelastic properties of the measured material can be deduced. During the course of this dissertation a setup has been developed in Professor Maier's and Professor Urbach's research groups and is now evaluated.

In the following, the setup will be described - a schematic of the setup is shown in figure 2.2. For details of the development and construction see [65].

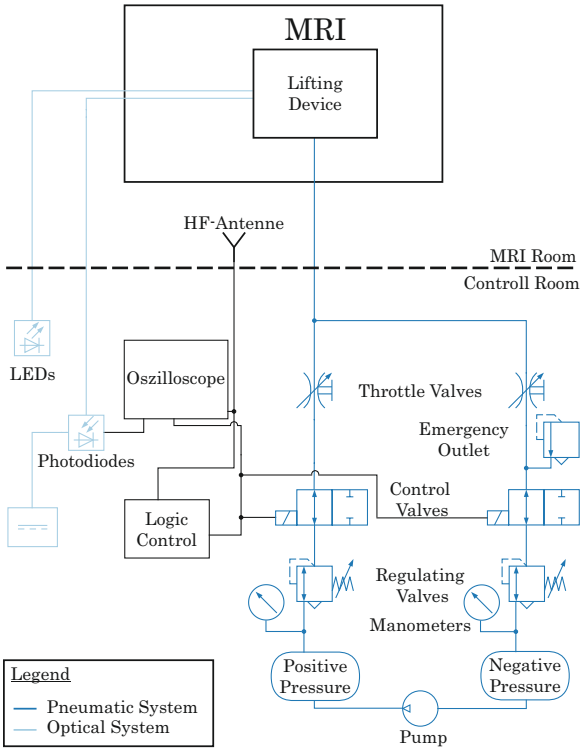

Figure 2.2: *Schematics of the experimental setup:*
The actual lifting device is located inside the head coil of a clinical MRI machine. It is driven pneumatically, while the macroscopic motion of the device is monitored optically. In order to synchronize the motion of the lifting device to the MRI sequence, either the RF-pulses of the sequence detected by an antenna or an optical trigger issued by the sequence are used to control the pneumatic. For a detailed description of each component see the corresponding sections.

As mentioned above, the experiment takes place inside an MRI head coil. To induce a fall, a lifting device is placed inside the coil. The lifting device is driven pneumatically in order to avoid components that disturb the imaging process. The pressure and the control system are located in the control room from which the actual MRI machine is electromagnetically shielded. The motion of the lifting device is monitored in real time using an optical system. Since the induced motion of the brain tissue is imaged with a motion encoding sequence, the fall has to be synchronized to the sequence which is realized by electronically processing either an optical trigger pulse or the RF-pulses issued by the sequence to control the pneumatic.

All these components will be described in further detail in the next sections. The MRI system used was a clinical 1.5 T MAGNETOM Avanto scanner equipped with a Head Matrix Tim coil (both Siemens Healthcare, Erlangen, Germany) located at the Life & Brain research center (Life & Brain GmbH, Bonn, Germany).

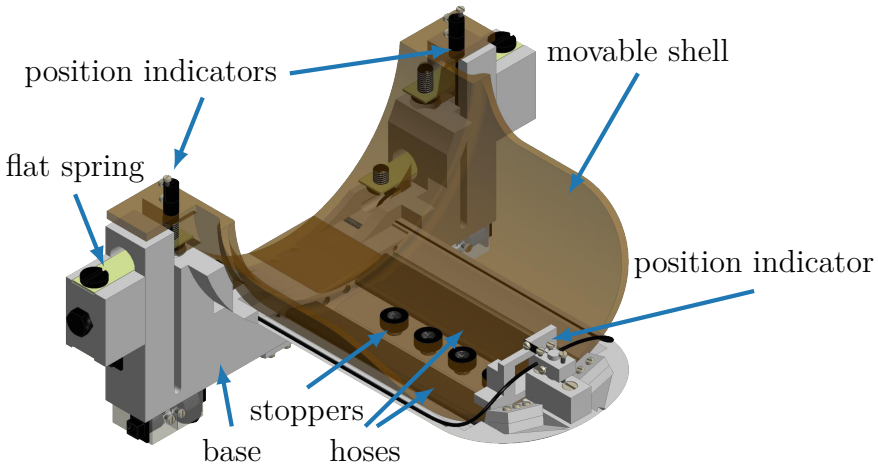

Figure 2.3: *Lifting Device:*
The base (gray part) is made of POM and fits tightly into the base of the head coil. The movable shell is made of a sandwich-structured composite made out of an aramid honeycomb and two layers of aramid-fiber reinforced laminate. Between the base and the shell two hoses are attached to the base which are connected to the pneumatic system and elevate the shell when inflated. When the hoses are evacuated the shell is allowed to fall. The shell is connected to the base through four flat springs and four screws which act as stoppers. The movement of the shell can be monitored at three points with an optical positioning system.

2.1.2.1 Lifting Device

The lifting device consists of a base (cf. fig. 2.3 - gray part) which fits tightly in the base of the head coil, and a movable shell (cf. fig. 2.3 - brown part) on which the subject's head is fixated.

The base is made out of polyoxymethylene (POM), a thermoplastic polymer which is distinguished both by its high stiffness and Young's modulus as well as by its low dielectric loss coefficient. The shell is constructed as a sandwich-structured composite made out of a 3 mm thick aramid honeycomb and two 1 mm thick layers of aramid-fiber reinforced laminate. This ensures that the shell is both very rigid and very light while still MRI-compatible.

Between the base and the shell two hoses are attached to the base which are connected to the pneumatic system. When they are filled with air, they lift up the shell and when they are evacuated, they allow the shell to fall.

For the purpose of impeding any rotating motion the shell is suspended from the base at four points by means of flat springs made of 0.9 mm thick fiberglass reinforced epoxy plates (GFK). To limit and adjust the lifting height, four screws in the middle of the shell act as stoppers. They limit the lifting height to maximal 1.5 mm. For the experiments discussed in this thesis, however, the height was set between 1.0 mm and 1.4 mm which was owned to the fact that the flat springs did not allow for a larger range of motion while still supporting the weight of the shell.

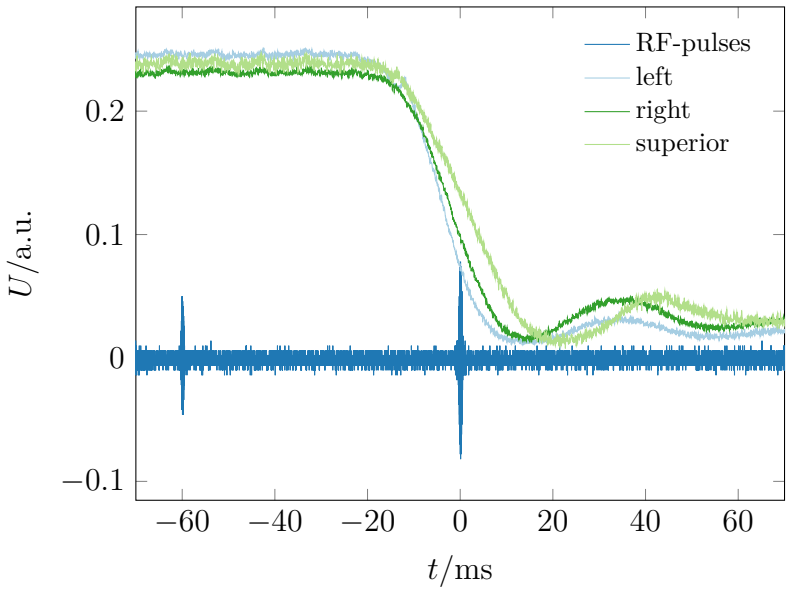

Figure 2.4: *Exemplary Positioning Curve:*
*The data displayed here is form a measurement on volunteer id*9 *for* $\tau = 35\,\text{ms}$ *(cf. fig. 2.6). The antenna detects the RF-pulses from the MRI sequence, here, both the* 90°*- and the* 180°*-pulse are shown. The signal from the positioning indicators located on either side of the subject's neck are plotted as left and right while the signal form the indicator located at the top of the subject's head is plotted as superior. At the beginning of the sequence, the signal of the positioning indicators is high, indicating that the shell resides steadily in the upper position. Approximately* 20 ms *before the 180°-pulse the shell starts to fall at all three points simultaneously. However, the slope of the signal is slightly different for the three indicators. After the landing (*$\approx 20\,\text{ms}$ *after the 180°-pulse) the shell apparently does not come fully to rest but bounces.*

The movement of the shell can be monitored at three points with an optical positioning system integrated into the base and located on both sides of a subject's neck and at the top of their head.

2.1.2.2 Optical Positioning System

The optical positioning system allows for a real time survey of the relative movement between base and shell. Light from three light emitting diodes (LEDs) located in the control room is guided through optical fibers to slits in the base and then picked up again by optical fibers and guided back into the control room. There, photodiodes register the light signal and convert it into an electronic signal that is displayed on an oscilloscope. In the slit a blind connected to the shell screens off a fraction of the light and the intensity transmitted is proportional to the vertical position of the shell.

In fig. 2.4 examples of the measured signals are plotted. In dark blue the RF-pulses of the MRI sequence detected by the antenna is shown. Both the excitatory 90°-

and the spin-echo generating 180°-pulse can be seen. The signal from the positioning indicators located on either side of the subject's neck (left and right) are plotted in light blue and dark green, respectively, while the signal from the indicator located at the top of the subject's head is plotted in light green (superior). The data displayed here comes from a measurement of a healthy volunteer. At the beginning of the sequence, the signal of the positioning indicators is high, indicating that the shell resides steadily in the upper position. Approximately 20 ms before the 180°-pulse the shell starts to fall at all three points simultaneously. However, the slope of the signal is slightly different for the three indicators. After the landing ($\approx$ 20 ms after the 180°-pulse) the shell apparently does not come fully to rest but bounces. In [65] it is shown that the light signal can be regarded as linear proportional to the vertical position of the shell, however, the data here is not calibrated so that no absolute statement about the trajectory of the shell can be made.

2.1.2.3 Pneumatic System

The pneumatic system is located in the control room and consists of two 10 L containers in which a vacuum membrane pump creates a positive and a negative pressure respectively. For the course of this thesis the values were set to positive 26.0 kPa and negative 16.0 kPa with an accuracy of 0.2 kPa compared to the ambient pressure. Both containers are connected via throttle and regulating valves to the same supply pipe connected to the hoses in the lifting device. To raise the device one control valve closes the low pressure circuit while another opens the overpressure one so that air can flow into the hoses. When a fall shall be induced the control valves are switched and the overpressure circuit is closed off while the air is sucked out of the hoses into the low pressure container. The switching of the control valves can be synchronized to the MRI sequence.

2.1.2.4 MRI Imaging Sequence

The relative movement between different volume elements (voxel, from *volume* and *pixel*) of brain tissue induced by the aforementioned excitation is expected to be in the micrometer scale. This can be imaged using a motion encoding MRI sequence (cf. sec. 1.1.2.8). For the work presented here, a modified single shot spin echo EPI sequence with two added gradients in phase encoding direction was used (cf. fig. 2.5) which was provided by Dr. Jürgen Finsterbusch (Universitätsklinikum Hamburg-Eppendorf, Department of Systems Neuroscience) [101]. This sequence is a composition of the concepts presented in section 1.1.2:

The image generation works basically like in an EPI sequence where a 90°-pulse and a slice selecting gradient are used for excitation while the frequency and phase encoding happens during a train of gradient echoes (cf. sec. 1.1.2.7). In this sequence, however, a spin echo generating 180°-pulse is added (cf. sec. 1.1.2.1). This allows for the echo train to start later so that the center of the echo train coincide with the center of the spin echo. The time gained by applying the spin echo is used to place

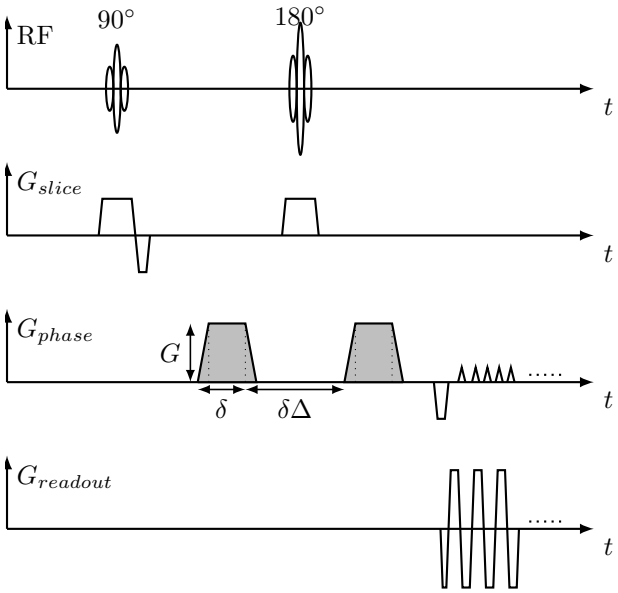

Figure 2.5: *Motion Encoding Spin Echo EPI Sequence:*
The sequence used is basically an EPI sequence with an additional spin echo generating 180°-pulse placed between the excitatory 90°-pulse and the beginning of the gradient echo train. To make the sequence motion sensitive, two identical trapezoidal gradients are placed around the 180°-pulse. The amplitude of the gradients is G, the time between the start of a gradient pulse and the end of the plateau δ, and the time between the end of the plateau of the first gradient and the start of the second δΔ. The first gradient imposes a phase shift on each spin ensemble. If the ensembles remain stationary, they are flipped by the 180°-pulse and the second gradient pulse cancels out the phase shift. However, if the spins have changed their position they do not see the exact same field during the second gradient and a phase offset remains, which can be visualized in a phase image. [72]

two motion encoding gradients around the 180°-pulse (cf. sec. 1.1.2.8). When the spin ensembles in a voxel do not move between the beginning of the first gradient and the end of the second one, any phase shift caused by the first one will be canceled out by the second one, since the polarity of the gradients are the same but the 180°-pulse flips the spin system. Have the spin ensembles though changed their position along the phase encoding axis, the second gradient cannot cancel out the phase shift imposed by the first one and a phase offset according to equation 1.12 remains which can be displayed in a phase image. The phase data extracted from these images form the basis for the work of this thesis.

The phase offset acquired depends according to eq. 1.12 - beside of the trajectory - on the shape of the gradients. In the sequence used the gradients were of trapezoidal form. The length of the gradients is defined as the time δ between the beginning of the rising ramp and the end of the plateau and could be chosen in the sequence settings additionally to the amplitude G of the gradients (cf. fig. 2.5). When there is motion during both gradients, the time $\delta\Delta$ between the lobes plays a role as well and this can also be adjusted in the sequence settings.

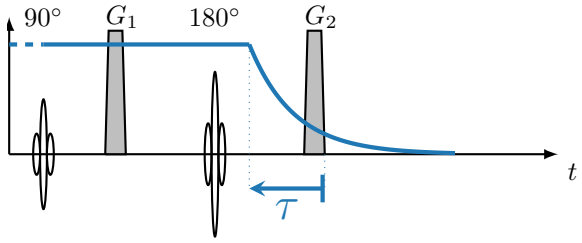

Figure 2.6: *Definition of τ:*
In order to define the synchronization between the MRI sequence (represented here by the 90°- and 180°-pulse and the two motion sensitizing gradient G_1/G_2) and the motion of the of the head (blue curve) the parameter τ is used. It is defined as the time between the end of the second motion encoding gradient and the beginning of the fall of the head. For $\tau \leq 0$, the fall only stars after the motion sensitive part of the sequence.

In order to synchronize the sequence and the motion of the lifting device so that specific parts of the system's response to the excitation can be encoded in the phase images two approaches were used. For earlier measurements a loop antenna was used to receive the RF-pulses of the sequence. These pulses were converted into a TTL(transistor-transistor logic)-pulse which was used to trigger the control valves of the pneumatic system. For later measurements the sequence was modified to issue a trigger pulse which could be read out optically. Using a photodiode it was converted into an electric pulse which was then also transformed into a TTL-pulse to operate the control valves. Both pulses could be digitally delayed so that the beginning of the fall of the shell can be shifted in relation to the sequence. The position of the optical trigger pulse issued by the sequence in relation to the 90°-pulse can also be changed by adjusting the sequence settings, thus changing the timing of the fall without changing the digital delay.

For the purpose of describing when the fall of the shell occurs in relation to the sequence the parameter τ is used. Its definition is explained in figure 2.6 as the time between the end of the second motion encoding gradient and the beginning of the fall. A negative value or a value of zero for τ implies that the shell starts moving only after the motion encoding part of the sequence so that no relevant information can be encoded in the phase images. A small positive value of τ implies that the beginning of the fall is observed as the shell is stationary in the upper position during the first gradient and begins to fall during the second gradient, while a large value of τ can mean that the shell moves during both gradients or even that the shell has landed before the first gradient and the development fo the system's response to the excitation in encoded in the phase images. This also means, that by taking a series of measurements with different values for τ basically the entire response of the brain tissue during the fall experiment can be sampled.

2.2 Human Subjects and Phantoms

In the course of this thesis, measurements were taken both on tissue mimicking phantoms and on healthy volunteers in order to assess the potential and limits of the

proposed method.

2.2.1 Human Subjects

The measurements on human subjects were taken on a group consisting of two females and eight males ranging in age from 26 to 32 years (mean: 28.9 years). The study was approved by the ethics committee of the University Hospital Bonn (directive 139/12) and written informed consent was obtained from all volunteers.

For the experiment the head of the subject was fixated in the lifting device inside the head coil with the use of a vacuum cushion (made by Sylvia Napiletzki in the course of her master's thesis) to minimize both voluntary and involuntary head motion (cf. fig. 2.7). For each subject a series of structural images were taken from which a transversal slice (a slice perpendicular to the longitudinal axis of the human body) lying only slightly above the ventricles and cutting through the cerebrum (cf. sec. 1.3.1 and 1.3.1.1) was selected. Using the motion sensitive sequence described in section 2.1.2.4 two time series were recorded where τ was varied.

For the first series the gradient values were chosen to be $\delta = 5.36\,\mathrm{ms}$, $\delta\Delta = 40\mathrm{ms}$ and $G = 25.4\,\mathrm{mT\,m^{-1}}$ with the gradient length δ being set to its minimal value. The τ-values sampled are listed in table 2.1. The sampling steps were mostly set to $\Delta\tau = 5\,\mathrm{ms}$. For the second time series the length of the gradients was increased to $\delta = 10.36\,\mathrm{ms}$ while the amplitude was decreased to $G = 17.3\,\mathrm{mT\,m^{-1}}$ to test how different gradient settings influence the results. Unfortunately, with the sequence version used it was not possible to change δ while keeping $\delta\Delta$ and G constant. In order to keep the time the subject had to stay inside the MRI to an acceptable level, the second time series was sampled more coarsely. The details can be found in table 2.2. For both series the additional sequence parameters (cf. sections 1.1.2.1 and 1.1.2.6) were chosen as follows: repetition time $T_R = 3000\,\mathrm{ms}$, echo time $T_E = 120\,\mathrm{ms}$, voxel size between $1.3\,\mathrm{mm} \times 1.3\,\mathrm{mm} \times 5\,\mathrm{mm}$ and $1.6\,\mathrm{mm} \times 1.6\,\mathrm{mm} \times 5\,\mathrm{mm}$. For each value of τ ten measurements were taken. Ten measurements were also taken while the head was at rest and no motion occurred during the sequence.

Figure 2.7: *Volunteer Inside the Head Coil: The head of the human subjects was fixated using a vacuum cushion to minimize voluntary and involuntary head motion.*

Volunteer	$\Delta\tau$ [ms]	$\tau_{\max}$ [ms]	τ_{missing} [ms]	N_τ	N_{total}	t_{total} [min]
id01a	5.0	115.0	90.0 - 95.0	22	345	17
id01b	5.0	105.0		22	345	17
id02	5.0	90.0	85.0	18	285	14
id03	5.0	125.0	80.0 - 95.0	22	345	17
id04	5.0	135.0	80.0 - 100.0	23	360	18
id05	5.0	135.0	75.0 - 95.0	23	360	18
id06	5.0	135.0	75.0 - 95.0	23	360	18
id07	5.0	140.0	80.0 - 100.0	24	375	19
id08a	5.0	140.0	80.0 - 100.0	24	375	19
id08b	1.0/2.0	100.0/140.0		121	1245	62
id09	5.0	140.0	80.0 - 100.0	24	375	19
id09	5.0	140.0	80.0 - 100.0	24	375	19

Table 2.1: *Measuring Protocols for Healthy Volunteers for First Gradient Setting: $\Delta\tau$ is the sampling interval used for the measurements, which was always 5 ms except for **id08b** for whom two different intervals were used. All measurements were taken from $\tau_{min} = 0$ ms to τ_{max}. The first τ_{max}-value for **id08b** denotes the change of the sampling interval. $\tau_{missing}$ indicates the data points in between that were not sampled in order to reduce the total scan time t_{total}. N_τ is the total amount of time points measured while N_{total} is the total number of acquisitions. These include also preparation scans of the EPI sequence that were not used to reconstruct an image as well as the acquisitions required for an image without induced motion.*

Volunteer	$\Delta\tau$ [ms]	$\tau_{\max}$ [ms]	τ_{missing} [ms]	N_τ	N_{total}	t_{total} [min]
id03	5.0/10.0	15.0/135	75.0 - 105.0	13	195	10
id04	5.0/10.0	15.0/145	75.0 - 105.0	15	240	12
id05	5.0/10.0	20.0/140	70.0 - 100.0	15	240	12
id06	5.0/10.0	20.0/140	70.0 - 100.0	15	240	12
id07	5.0/10.0	20.0/140	70.0 - 100.0	15	240	12
id08a	5.0/10.0	20.0/140	70.0 - 100.0	15	240	12
id09	5.0/10.0	20.0/140	80.0 - 110.0	15	240	12
id09	5.0/10.0	25.0/145	75.0 - 105.0	16	255	13

Table 2.2: *Measuring Protocols for Healthy Volunteers for Second Gradient Setting: The measuring protocol is described correspondingly to table 2.1. The sampling interval used for the measurements was 5 ms up to the first τ_{max} and 10 ms for the measurements after $\tau_{missing}$.*

2.2.2 Tissue mimicking Phantoms

In order to validate and to better understand measurements taken on human subjects phantoms where produced and measured that were supposed to mimic the brain tissue inside the hard skull. Different phantoms were used but they all had the same basic setup. The skull was imitated by a cylindrical container made out of polymethyl methacrylate (PMMA, a transparent thermoplastic) while an agar based hydrogel simulated the soft brain tissue.

First the basic design and the material is described in more detail before the different phantom realizations are introduced.

2.2.2.1 Phantom Container and Material

To investigate the boundary effect of the size of the probe, containers with six different diameters were used: $d = 85\,\text{mm}, 90\,\text{mm}, 100\,\text{mm}, 110\,\text{mm}, 127\,\text{mm}, 144\,\text{mm}$. All cylinders had a height of $h = 100\,\text{mm}$ and could fit accurately inside the shell of the lifting device (cf. fig. 2.8). To protect them from sliding during the experiment they were fixated with tape. Since even the largest container has only a volume of about 1.6 L, yielding a weight of about 1.6 kg when filled with hydrogel, they were weighed down with sandbags to approximate the weight of a human head (which lies in the order of 3.5 kg-4.7 kg [102]) and the vacuum cushion used (2 kg).

The material used to simulate the brain tissue was chosen with regards to mainly two aspects. It should be possible to produce the phantom material easily and to vary its rheological properties. The agar based hydrogel chosen is a material which fulfills these criteria and is also widely used for elastography experiments in the literature [103–106]. Agar is a substance derived from certain red seaweeds and consists of different polysaccharides which can be divided into agarose - the polysaccharide fraction with high gelling potential - and agaropectin - the poor or non-gelling charged polysaccharides. Since agar is composed in fact of an heterogeneous population of molecules, different kinds of agar can vary in their physico-chemical and rheological properties [107]. In the course of this thesis Agar-Agar, Kobe I (Carl Roth GmbH & Co. Kg, Karlsruhe, Germany) was used which has a gelling temperature of 35 to 42 °C

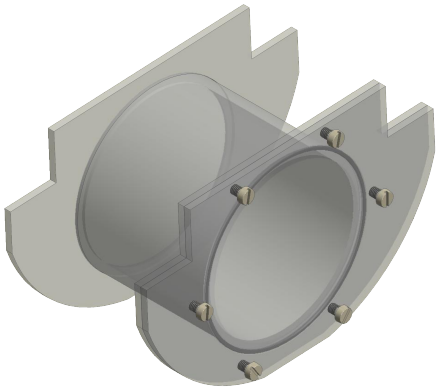

Figure 2.8: *Phantom Container:*
Phantom container with different diameters were used. They all had the same basic setup and were made out of a PMMA tube with a length of $h = 100\,\text{mm}$ covered with two plates which allowed the container to fit accurately inside the shell of the lifting device.

and a gel strength of $\geq 1000\,\mathrm{g\,cm^{-2}}$ (for a 1.5 % gel). The gel was prepared by adding the agar into water and boiling the mixture for 2.5 min while stirring. It was then cooled down in a water quench to about 45 °C at which point the mixture was poured into the phantom container and allowed to cool down further until the gelling process was completed. In order to change the shear modulus of the gel the agar concentration was varied [103, 108]. The relation between agar concentration and shear modulus follows a power law [109] and for the work presented here, the relation observed by Hall *et al.* was used for orientation:

$$E \approx 0.349\,\mathrm{kPa} \cdot \left(\frac{C}{\mathrm{g\,L^{-1}}}\right)^{1.87} \tag{2.1}$$

with E the Young's modulus in kPa and C the agar concentration in $\mathrm{g\,L^{-1}}$ [110]. From this and the relation between shear and Young's modulus given in equation 1.18 (which can be justified since the loss modulus of agar gel is much lower than its storage modulus, thus it behaves almost fully elastic [103, 109], and since it is nearly incompressible) the shear modulus can be estimated to be

$$G = E/3 \approx 0.116\,\mathrm{kPa} \cdot \left(\frac{C}{\mathrm{g\,L^{-1}}}\right)^{1.87} . \tag{2.2}$$

Since brain tissue is assumed to be quite soft (cf. sec. 1.3.2.1) agar concentrations between 0.422 ± 0.009 % and 0.927 ± 0.020 % were used for the phantoms. This corresponds to shear moduli between $1.87 \pm 0.03\,\mathrm{kPa}$ and $7.5 \pm 0.3\,\mathrm{kPa}$ according to equation 2.2.

The errors for the agar concentrations arise from uncertainties in both measuring the mass of the agar and of the water as well from water evaporating during the cooking procedure.

2.2.2.2 Phantom Realizations

Both homogeneous and inhomogeneous phantoms were tested. All phantoms used are listed in the following tables 2.3, 2.4, 2.5, 2.6.

With the use of homogeneous phantoms the influence of the agar concentration and of the diameter of the container was investigated. Six different container sizes and seven different agar concentrations were used (phantoms α_1 to ζ_7, table 2.3). For each kind of phantom between one and six (67 phantoms overall) realizations were produced.

To investigate the effect of the coupling between the homogeneous hydrogel and the container different spongy interlinings loosely based of the coupling between the brain tissue and the skull through the meninges (cf. sec. 1.3.1.1) were used (constructed by Birgit Schu-Schätter in the course of her diploma's thesis). Three different kind of sponges were used as interlinings: a coarsely pored and a fine pored rubber sponge as well as medium pored cellulose sponge. From each sponge a lining for a 144 mm container was constructed with a thickness of $x \approx 16\,\mathrm{mm}$. In order to prevent the

liquid hydrogel to soak the sponges, they were sealed using UHU Poly Max®Glasklar Express, a waterproof, silyl modified polymer sealant [111]. Hydrogels with two different agar concentrations were used here (phantoms λ_1 to ν_2, table 2.6).

Inhomogeneous phantoms were used to assess the possibility to distinguish different agar concentrations inside one phantom as well as small substructures. Therefore, both phantoms with two layers of hydrodgel with different agar concentrations as well as a phantom consisting of two small cubes of hydrogel embedded into a homogeneous hydrogel with a different concentration were used. Additionally, a cyst was simulated by embedding a water filled spherical balloon inside an agar phantom. For the two layered phantoms, three 110 mm containers were lined with a 9 mm thick fine pored rubber sponge, which was sealed again with UHU Poly Max®. The interlining was used to prevent the hydrogel from turning inside the container, so that a fixed orientation of the two layers could be ensured. One half of each container was filled with a still liquid 0.640 % hydrogel. During the gelling process the containers were turned on the side. After the gelling was completed the rest of the container was filled with a second hydrogel. Three different concentrations were used (ϑ_1 to ϑ_3, table 2.5). After the measurements the container was opened and it was manually ensured that the two layers were still connected and could not slide against each other. For the phantom with the cubic inclusions η (cf. table 2.4) first the 0.442 % hydrogel for the cubes was cooked and allowed to cool down. From this two cubes with an edge length of $e_c \approx 15\,\mathrm{mm}$ were cut. Then a 127 mm container was filled with a 0.640 % liquid hydrogel. During the gelling process the cubes were carefully placed to float in the surrounding hydrogel while it cooled down completely. For the phantom simulating a cystic inclusion κ (cf. table 2.6) a 85 mm container was used. A balloon filled with water to a diameter of $d = 33\,\mathrm{mm}$ was hung inside the container, which was then filled with an 0.736 % hydrogel.

For all but the κ phantom with the fluid filled inclusion time series were measured alike those for the human subjects. The parameters were chosen as follows: $\delta = 5.36\,\mathrm{ms}$, $\delta\Delta = 40\,\mathrm{ms}$, $G = 25.4\,\mathrm{mT\,m^{-1}}$, $0\,\mathrm{ms} \leq \tau \leq 120\,\mathrm{ms}$, $\Delta\tau = 2\,\mathrm{ms}$, $T_R = 3000\,\mathrm{ms}$, $T_E = 120\,\mathrm{ms}$, voxel size between $1.3\,\mathrm{mm} \times 1.3\,\mathrm{mm} \times 5\,\mathrm{mm}$ and $1.6\,\mathrm{mm} \times 1.6\,\mathrm{mm} \times 5\,\mathrm{mm}$. For each value of τ ten measurements were taken. Ten measurements were also taken while the phantom was at rest and no motion occurred during the sequence. For each kind of homogeneous phantom multiple realizations of the phantoms were produced. One phantom realization of a β_4, a γ_4 and a δ_4 phantom were measured twice on the same day, respectively, in order to estimate how the positioning of the phantom container and the additional sandbags on the lifting device influence the measurements.

In a proof of principle measurement, for the phantoms with fluid filled inclusion only one τ-value was measured for $\tau = 50\,\mathrm{ms}$. The imaging parameters were chosen as follows: $\delta = 5.36\,\mathrm{ms}$, $\delta\Delta = 20\,\mathrm{ms}$, $G = 34.6\,\mathrm{mT\,m^{-1}}$, $T_R = 3000\,\mathrm{ms}$, $T_E = 120\,\mathrm{ms}$, voxel size $1.4\,\mathrm{mm} \times 1.4\,\mathrm{mm} \times 5\,\mathrm{mm}$.

Phantom	d[mm]	c[%]	G[kPa]
α_1	85	0.422(9)	1.87(7)
α_2	85	0.529(11)	2.63(10)
α_3	85	0.640(14)	3.73(13)
α_4	85	0.705(15)	4.5(2)
α_5	85	0.795(17)	5.6(2)
α_6	85	0.850(18)	6.37(27)
α_7	85	0.927(20)	7.5(3)
β_4	90	0.705(15)	4.5(2)
β_5	90	0.795(17)	5.6(2)
β_6	90	0.850(18)	6.37(27)
γ_4	100	0.705(15)	4.5(2)
γ_5	100	0.795(17)	5.6(2)
γ_6	100	0.850(18)	6.37(27)
δ_1	110	0.442(9)	1.87(7)
δ_2	110	0.529(11)	2.63(10)
δ_3	110	0.640(14)	3.73(13)
δ_4	110	0.705(15)	4.5(2)
δ_5	110	0.795(17)	5.6(2)
δ_6	110	0.850(18)	6.37(27)
ϵ_3	127	0.640(14)	3.73(13)
ϵ_4	127	0.705(15)	4.5(2)
ϵ_5	127	0.795(17)	5.6(2)
ϵ_6	127	0.850(18)	6.37(27)
ζ_4	144	0.705(15)	4.5(2)
ζ_5	144	0.795(17)	5.6(2)
ζ_6	144	0.850(18)	6.37(27)
ζ_7	144	0.927(20)	7.5(3)

Table 2.3: *Homogeneous Phantoms:*
List of the homogeneous phantoms measured sorted by the diameter of the container. For each container size, phantoms with different agar concentration c (yielding corresponding shear moduli G) were produced. For each kind of phantom multiple realizations were produced.

Phantom	Surroundings		Cube		
	c_s[%]	G_s[kPa]	c_c[%]	G_c[kPa]	e_c[mm]
η	0.640(14)	3.73(13)	0.442(9)	1.87(7)	15

Table 2.4: *Phantom with Two Cubic Inclusions:*
A container with a diameter of $d = 127\,\mathrm{mm}$ was used. Two inclusions with the same mechanical properties and edge lengths e_c were placed inside the surrounding hydrogel.

Phantom	Layer 1		Layer 2	
	c_1[%]	G_1[kPa]	c_2[%]	G_2[kPa]
ϑ_1	0.640(14)	3.73(13)	0.795(17)	5.6(2)
ϑ_2	0.640(14)	3.73(13)	0.705(15)	4.5(2)
ϑ_3	0.640(14)	3.73(13)	0.529(11)	2.63(10)

Table 2.5: *Phantoms Consisting of Two Layers:*
A container with a diameter of $d = 110\,\text{mm}$ *lined with a fine pored rubber sponge of thickness* $x = 9\,\text{mm}$ *was used.*

Phantom		c[%]	G[kPa]
κ	fluid filled inclusion	0.736(16)	4.9(3)
λ_1	coarsely pored rubber sponge	0.795(17)	5.6(2)
λ_2	coarsely pored rubber sponge	0.850(18)	6.37(27)
μ_1	fine pored rubber sponge	0.795(17)	5.6(2)
μ_2	fine pored rubber sponge	0.850(18)	6.37(27)
ν_1	medium pored cellulose sponge	0.795(17)	5.6(2)
ν_2	medium pored cellulose sponge	0.850(18)	6.37(27)

Table 2.6: *Phantom with Fluid Filled Inclusion and Homogeneous Phantoms with Interlining:*
The container diameter for the phantom with the fluid filled inclusion was $d = 85\,\text{mm}$ *and for the phantoms with an interlayer it was* $d = 144\,\text{mm}$.

2.3 Data Processing

The MR magnitude and phase images were available in the Digital Imaging and Communications in Medicine (DICOM) standard. It includes the 12 bit image data as well as additional information (for example imaging parameters). The images can be viewed and edited using various software programs. For the analysis presented here ImageJ, a Java based image processing and analysis program (U.S. National Institutes fo Health, Bethesda, Maryland, USA, http://imagej.nih.gov/ij/) [112, 113], and a Python (Python Software Fondation, Version 2.7) based package written by Theilenberg [114] were used.

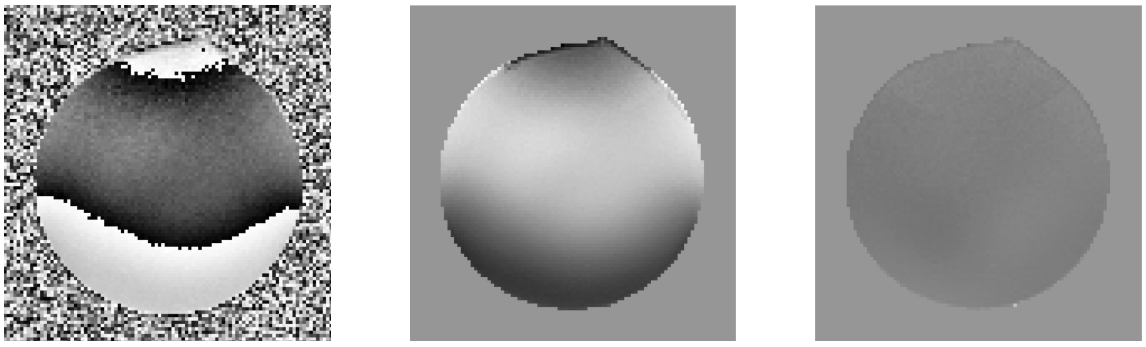

(a) *single image with motion*

(b) *averaged and unwrapped with motion*

(c) *averaged and masked without motion*

Figure 2.9: *Exemplary Phase Images:*
In (a) a raw phase image of a homogeneous γ_5 phantom taken with induced motion is shown. The noise around the circular cut through the phantom results from the fact that there is no signal coming from this area and thus, the phase is not well defined. Since the phase is only defined from $0-2\pi$, values exceeding this range result in a phase discontinuity in the image - the abrupt transition from white to black. For further analysis the area around the phantom is masked and the phase is unwrapped (b). Then a masked average over ten measurements without motion is taken (c). This is subtracted from the average of ten masked and unwrapped images with motion to correct for unwanted motion as well as magnetic field inhomogeneities, resulting in the right image.

In figure 2.9 exemplary phase images from a homogeneous phantom are shown to illustrate the basic data processing steps taken with all images. On the left side a single raw phase image with motion is shown. In the area around the circular phantom there is noise due to the fact that there is no MR signal in this area and thus a phase cannot be defined (cf. fig. 2.9a). During the further analyzing steps this area is always masked. The mask was created from a magnitude image at rest using ImageJ. Since the phase is defined periodically in the interval $[0; 2\pi)$ a motion exceeding the range of 2π leads to a phase jump - a value of $2\pi + \delta$ is perceived as identical to δ. In the image this is visualized by a jump from white $(2\pi - \epsilon)$ to black (0). These phase jumps can be unwrapped by unfolding the data onto an interval with a length of multiple times of 2π using a quality guided [115] or the Goldstein [115, 116] algorithm implemented

in the Python package that was used for all further data processing. The unwrapping can produce an offset of 2π between two images which have originally been measured in reference to the same master phase, since it is not unambiguously defined in which direction the phase interval is expanded. After masking and unwrapping all phase images - with and without motion - an average over the ten measurements taken for one τ was generated (cf. fig. 2.9b). Then the averaged image without induced motion (cf. fig. 2.9c) was subtracted from each average with induced motion to correct for effects due to unwanted motion (like vibrations from the MRI table) or due to magnetic field inhomogeneities.

Because a technique to reconstruct the true trajectory of each voxel from the phase data is still a subject of research and requires up to now substantial additional measurement time, a goal of this thesis is to investigate whether significant information can be extracted just from the phase data.

The absolute phase of a voxel is not suitable for analysis since in it both the macroscopic motion of the whole ensemble of shell, container and phantom material is encoded while physical relevant and comparable for different τ is the relative motion of the phantom material in the center of mass reference frame. However, measuring the phase accumulating only through the macroscopic motion was not possible. Alternative approaches are investigated and described in the following chapter.

3 Results

In this chapter, the results of measurements of phantoms and human volunteers are presented.

3.1 Homogeneous Phantoms

In this section measurements of different homogeneous phantoms are presented. By means of these measurements the response of a simple system to the in the previous chapter described excitation (cf. sec. 2.1) is investigated. A method to extract information and compare measurements is developed and the influence of the agar concentration (and thus of the stiffness of the material) as well as of the size of the phantom is investigated. Additionally, the influence of the boundary between hydrogel and container is briefly examined.

3.1.1 Response to excitation

After a shock excitation, it is expected that a broad band of frequencies is excited, which are increasingly dampened the higher the frequency until only the lowest resonance frequency of the system remains. It is assumed that this frequency should depend both on the geometry and the elastic properties of the system, while the viscose properties should be reflected mainly in the dampening of the oscillation.

In order to verify this assumption a series of phase images is acquired which measures the time response of a homogeneous phantom to the excitation of a fall. After these images are processed as described in sec. 2.3 (phase unwrapping and background correction), the time series of images shows an oscillatory behavior in the phase as can be seen for exemplary measurements on a γ_5 ($100\,\mathrm{mm}, 5.6\,\mathrm{kPa}$) phantom in fig. 3.1. For $\tau = 0\,\mathrm{ms}$ the phase image exhibits a homogeneous phase since the fall only begins after the motion encoding part of the MRI sequence (cf. fig. 2.6). For higher values of τ it can be seen that the center of the phantom moves differently than the border region which is surrounded by the container. For some τ-values in these images the center of the phantom is lighter (corresponding to a higher phase), thus indicating a displacement relative to the border region (cf. fig. 3.1d, 3.1f, 3.1h) while for other the center is darker (corresponding to a lower phase), indicating a displacement in the opposite direction (cf. fig. 3.1e, 3.1g).

In order to illustrate this oscillation more clearly and investigate it further the phase along a horizontal line through the center of the phantom is plotted for different values of τ in fig. 3.2. Here, the oscillation becomes apparent very clearly but there is also a

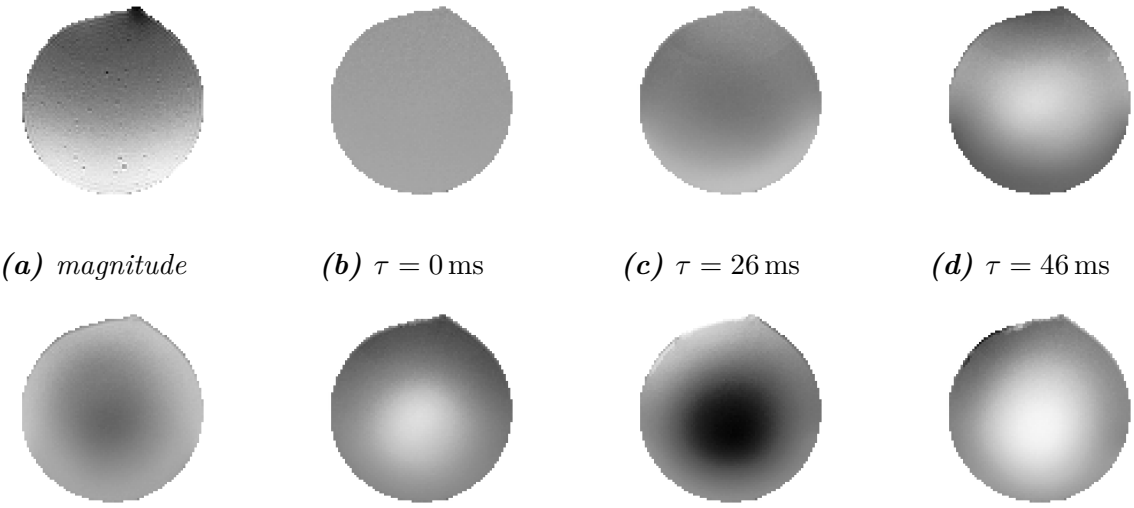

(a) *magnitude* **(b)** $\tau = 0\,\mathrm{ms}$ **(c)** $\tau = 26\,\mathrm{ms}$ **(d)** $\tau = 46\,\mathrm{ms}$

(e) $\tau = 62\,\mathrm{ms}$ **(f)** $\tau = 80\,\mathrm{ms}$ **(g)** $\tau = 94\,\mathrm{ms}$ **(h)** $\tau = 110\,\mathrm{ms}$

Figure 3.1: *Exemplary Magnitude and Phase Images:*
(a) shows a magnitude image of a γ_5 phantom ($100\,\mathrm{mm}, 5.6\,\mathrm{kPa}$*). Some small air bubbles can be seen. (b) to (h) show phase images for different τ-values. For $\tau = 0\,\mathrm{ms}$ the phantom has a homogeneous phase since the fall begins only after the motion encoding. For higher values of τ it can be seen that the center of the phantom moves differently than the border region connected to the container. For some τ-values ((d), (f), (h)) the center is lighter - corresponding to a higher phase and thus a motion - compared to the border region while for other τ-values it is darker (corresponding to a lower phase and thus a motion in the opposite direction) ((e), (g)). Overall, a oscillatory behavior of the phase can be observed.*

phase offset between the plots for different τ-values which can be attributed to the macroscopic movement or to the unwrapping procedure (cf. sec. 2.3).

When considering the response of a single voxel to the excitation these offsets prove to be an obstacle. In fig. 3.3 the phase of the central voxel of the γ_5 phantom is plotted against τ. The phase exhibits discontinuities, which cannot be removed if the phase difference between two points exceeds π.

In order to overcome the influence of the macroscopic motion and reduce the probability of discontinuities the relative phase $\Delta\phi$ in relation to a reference phase inside the phantom is calculated. For the phantoms, the reference is chosen as the mean between the phase of the outer left and outer right voxel in the central line (ϕ_L, ϕ_R), thus leading for the relative phase $\Delta\phi_i$ for a voxel i to:

$$\Delta\phi_i = \phi_i - \frac{\phi_L + \phi_R}{2}\,. \tag{3.1}$$

When the cuts through the phantom and the temporal behavior of the central voxel are plotted using the relative phase $\Delta\phi$, continuity does not provide a problem anymore (cf. fig. 3.4) and the oscillation can be examined easily for a single voxel (cf. fig. 3.5).

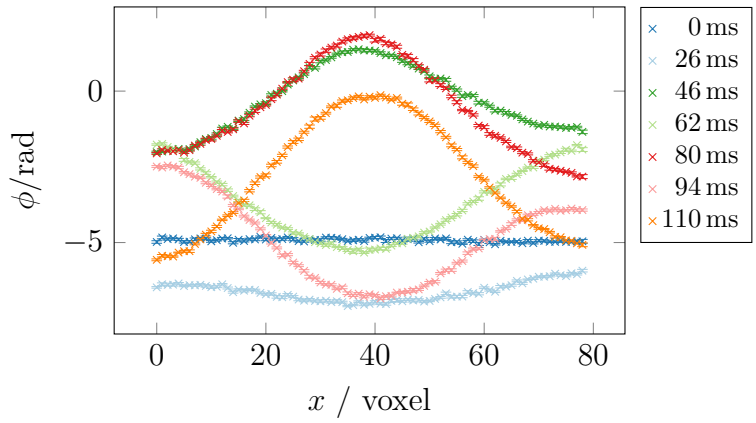

Figure 3.2: *Phase ϕ vs. Voxel:*
ϕ is plotted along a horizontal cut through the middle of a γ_5 phantom for several τ-values. Here, the oscillation in the phase becomes apparent very clearly. However, a phase offset between the plots for different τ-values can also be observed.

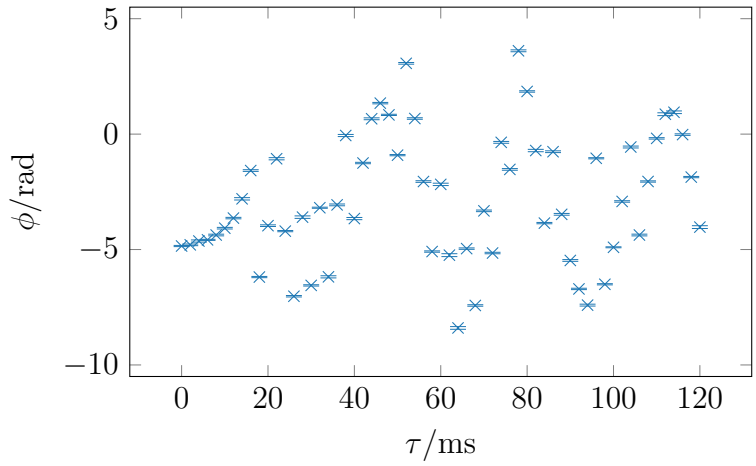

Figure 3.3: *Discontinuous Temporal Behavior of a Single Voxel:*
The phase ϕ of the central voxel of the γ_5 phantom is plotted versus τ. The phase exhibits discontinuities which prohibit an interpretation of this data.

After the transient effect during the roughly first 30 ms it is possible to extract the frequency f of the oscillation from the data. This is done by interpolating the data using a weighted spline of third order and determining the value of τ_n for each of the spline's n extrema (cf. fig. 3.5). Then the τ_n are plotted against the number n of the extrema and via a weighted line fit (cf. fig 3.6) the frequency is calculated from the slope a as

$$f = \frac{1}{T} = \frac{1}{2a}. \tag{3.2}$$

In order to estimate errors on the frequency, firstly the statistical errors for $\Delta\phi$ are computed from the ten measurement repetitions (cf. sec. 2.2.2.2) which are also shown in the plots in fig. 3.2 to 3.5. Those statistical errors are then propagated to the frequency using a parametric bootstrap procedure with 1500 bootstrap samples. For the bootstrap procedure simulated data sets are drawn from the normal distribution of the original data set. The width of the distribution is determined by the statistical errors of the original data points. For each simulated data set a frequency is calculated as described above, yielding a distribution of 1500 frequencies. The standard deviation of this frequency distribution corresponds then to the standard error of the frequency extracted from the original data set.

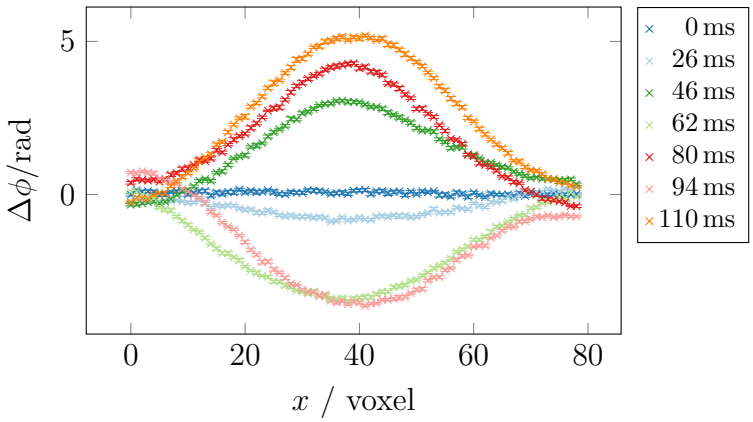

Figure 3.4: *Relative Phase $\Delta\phi$ vs. Voxel:*
$\Delta\phi$ is plotted on a horizontal cut through the middle of a γ_5 phantom for several τ-values. Here, the oscillation in the phase can be seen nicely while also no phase discontinuities are present and the outer voxel are in a narrow range of values. (Already published in [62].)

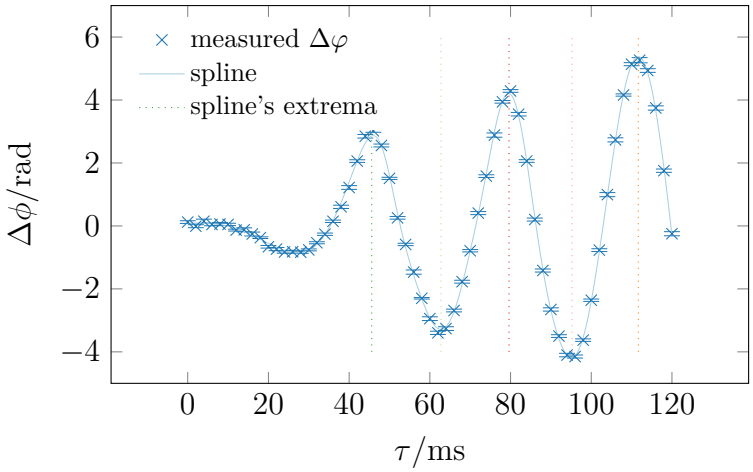

Figure 3.5: *Continuous Temporal Behavior of a Single Voxel:*
The relative phase $\Delta\phi$ of the central voxel of the γ_5 phantom is plotted versus τ. After a transient phenomenon up to about 30 ms an oscillation can be observed. Additionally, the interpolating spline and the spline's extrema used for calculating the frequency are plotted. (Already published in [62].)

3.1.1.1 Disturbed Measurements

The validity of this method to calculate the frequency is based on the quality of the oscillation data of the relative phase and its conformity to the hypothesis that the data can be characterized by a single frequency. Fig. 3.5 shows a very good example. However, also deviations could be observed - examples of the different problems that can occur are shown in fig. 3.7. Sometimes a measurement has to be rejected and sometimes only a part of the measurement can be used to determine the frequency, reducing the confidence of the frequency value.

In figure 3.7a the influence of artifacts can be seen which occur when the border of a phase discontinuity is slightly blurred (which is a motion artifact). Then the phase cannot be correctly unwrapped which leads to extremely high errors and discontinuities for some τ-values and can make it difficult to correctly determine the position of the extrema (in the example given here the third extrema at approximately $\tau = 80\,\text{ms}$ is not well defined due to unwrapping artifacts).

In fig. 3.7b the relative phase data displays two challenges to extract the frequency

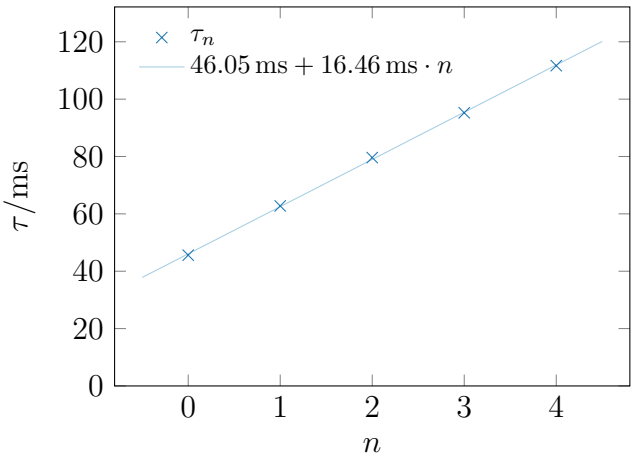

Figure 3.6: *Line Fit to Determine the Frequency:*
The τ_n-values of each extrema n are plotted. From the slope of the weighted line fit, which represents half of the periodic time T, the frequency is determined according to eq. 3.2.

with good precision. On the one hand the time measured allowed only for two extrema to develop and on the other hand the second extrema is not well defined but quite broad.

In the case of fig. 3.7c a clear oscillation can be seen up to $\tau = 84\,\text{ms}$. Between $84\,\text{ms} < \tau < 108\,\text{ms}$ a plateau forms, which cannot be explained up to now, and then it seems as if another maximum develops. Here, only the measured points up to $\tau = 80\,\text{ms}$ are considered for extracting the frequency.

In fig. 3.7d the determination of the frequency is hampered by the double peak around 100 ms which occurs in the data of some phantoms while the data displayed in fig. 3.7e shows a somehow erratic and diminished oscillation for $\tau > 60\,\text{ms}$.

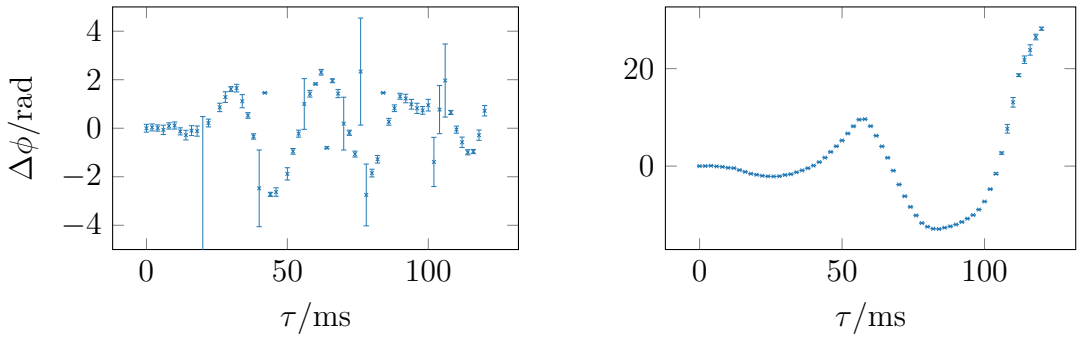

(a) α_7, *(*85 mm, 7.5 kPa*)*

(b) δ_2, *(*110 mm, 2.63 kPa*)*

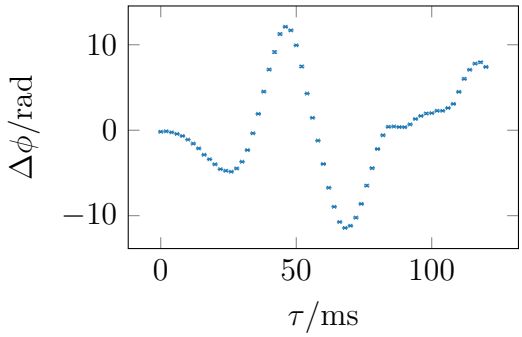

(c) ϵ_5, *(*127 mm, 5.6 kPa*)*

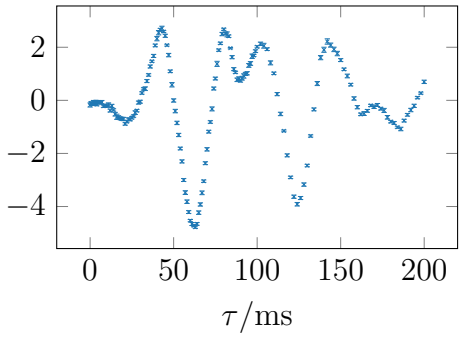

(d) α_6, *(*85 mm, 6.37 kPa*)*

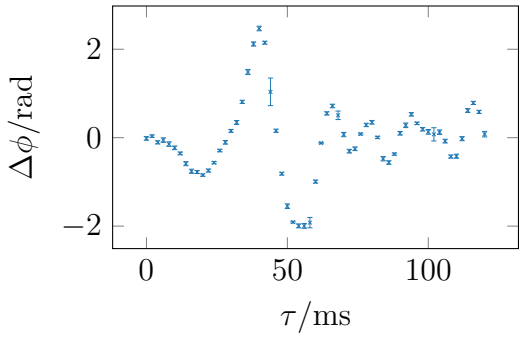

(e) β_5, *(*90 mm, 5.6 kPa*)*

Figure 3.7: *Examples of Disturbed Phase Oscillations:*
These plots illustrate the different challenges that can occur when extracting the frequency from the phase oscillation. In (a) the errors for some τ-values are extremely high. This is the influence of a motion artifact which blurs the border of a phase discontinuity slightly. The phase can then not be correctly unwrapped, which leads to these high errors and residual discontinuous data points. In (b) two challenges can be observed: the time measured allowed only for two extrema to develop and the second extremum is not well defined but quite broad. Both facts make it difficult to extract the frequency precisely. In (c) a plateau forms between $84\,\text{ms} < \tau < 108\,\text{ms}$ *which cannot be explained up to now. Here, only the measured point up to* $\tau = 80\,\text{ms}$ *are considered for extracting the frequency. In (d) the determination of the frequency is hampered by the double peak around* 100 ms *which occurs in the data of some phantoms while the data displayed in (e) shows a somehow erratic and diminished oscillation for* $\tau > 60\,\text{ms}$.

3.1.1.2 Comparison with spatial oscillation

Using the previously presented findings, a way to characterize a phantom through the frequency f of the oscillation of the relative phase $\Delta\phi$ is proposed. However, before it is used to compare phantoms it is worth to consider how the thus determined frequency relates to the spatial frequency f_s of the oscillation a voxel performs in space coordinates. Since determining the trajectory in space of a voxel was not possible for the data presented here (cf. sec. 2.3), a theoretical trajectory is used to examine the correlation between the phase and the spatial frequency.

A spatial oscillation with a transient part at the beginning was used as an example. In fig. 3.8 two realizations of a trajectory $y(\tau)$ are shown for frequencies $f_{s1} = 15\,\mathrm{Hz}$ and $f_{s2} = 30\,\mathrm{Hz}$. Using eq. 1.12 the trajectories were converted into the phase $\phi(\tau)$ for the gradients $G(u)$ as they were used in the measurements ($\delta\Delta = 45\,\mathrm{ms}, \delta = 5\,\mathrm{ms}, |G| = 25.397\,\mathrm{mT\,m^{-1}}$) which was then plotted together with the corresponding trajectory. When comparing both curves it can be seen that for approximately the time of the gradients ($\delta\Delta + 2\,\delta = 55\,\mathrm{ms}$) the frequency of the phase does not match the frequency of the spatial oscillation. After an appropriate time, however, the frequencies align with each other. When the frequency is determined from the whole time series as described in the previous part of this section it can be illustrated that the deviations between the spatial frequency f_s' and the phase frequency f extracted from the slope of the fits (cf. eq. 3.2) are acceptable small as they result to $f_{s1}' = 15\,\mathrm{Hz}$ vs. $f_1 = 14.4\,\mathrm{Hz}$ and $f_{s2}' = 30.3\,\mathrm{Hz}$ vs. $f_2 = 30.1\,\mathrm{Hz}$ (cf. fig. 3.9). When comparing these results to the theoretical values, the slight influence of the transient part of the curve becomes apparent for the higher frequency.

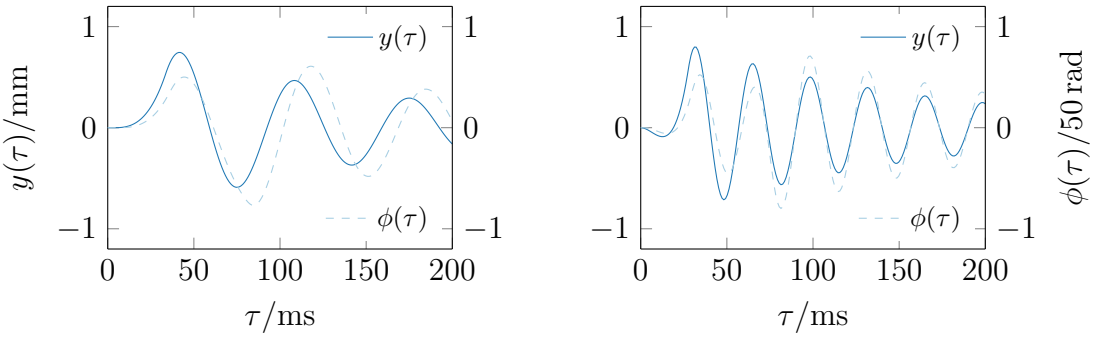

(a) $f_{s1} = 15\,\mathrm{Hz}$ ***(b)*** $f_{s2} = 30\,\mathrm{Hz}$

Figure 3.8: *Comparison between Spatial and Phase Oscillation:*
Two theoretical spatial oscillations with a transient part at the beginning are compared to their respective phase oscillations determined using eq. 1.12. The following parameters were used: $f_{s1} = 15\,\mathrm{Hz}$ *(a),* $f_{s2} = 30\,\mathrm{Hz}$ *(b),* $\delta\Delta = 45\,\mathrm{ms}, \delta = 5\,\mathrm{ms}, |G| = 25.397\,\mathrm{mT\,m^{-1}}$. *When comparing both curves it can be seen that for approximately the time of the gradients* ($\delta\Delta + 2\,\delta = 55\,\mathrm{ms}$) *the frequency of the phase does not match the frequency of the spatial oscillation. After an appropriate time, however, the frequencies align with each other. In the case of the lower frequency (a) a phase offset remains.*

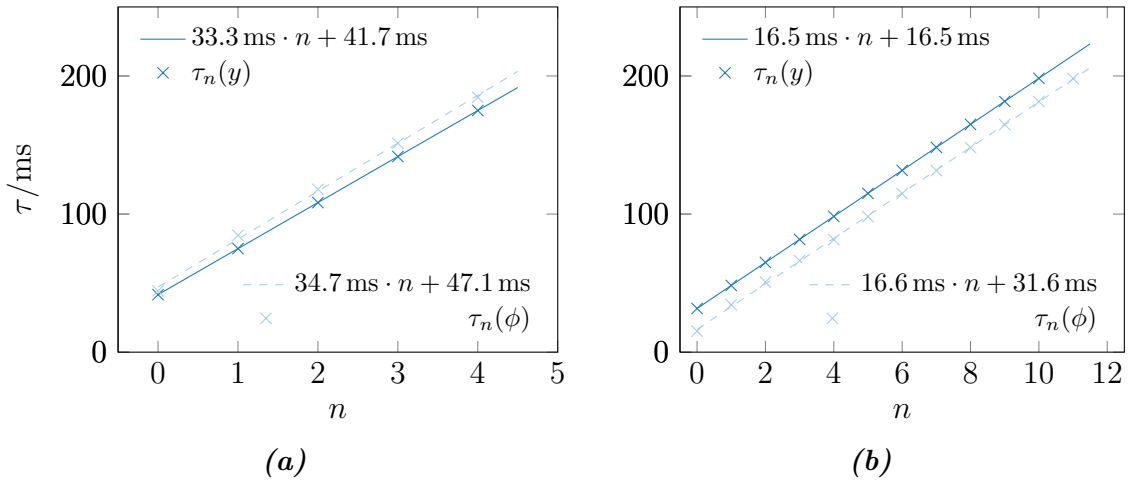

Figure 3.9: *Comparison of Line Fits for Spatial and Phase Oscillation:*
Here, the line fits used to determine the frequency of both the spatial as well as the phase oscillation are compared for the two examples presented in fig: 3.8. The slopes differ more for the lower frequency in (a), but the differences in the frequency are in both cases acceptably small: $f'_{s1} = 15\,\mathrm{Hz}$ *vs.* $f_1 = 14.4\,\mathrm{Hz}$ *for (a) and* $f'_{s2} = 30.3\,\mathrm{Hz}$ *vs.* $f_2 = 30.1\,\mathrm{Hz}$ *for (b).*

3.1.1.3 Frequency distribution

In a last step, it is investigated how f depends on the choice of the individual voxel (up to now the central voxel of a slice was used) and on the slice measured. In a cylindrical phantom it is expected that the frequency determined for a phantom is consistent over most of the volume - apart from regions where boundary conditions predominate the behavior of the material. The frequency was calculated in the manner described above for 25 different voxel on a 5×5 grid spaced equally over the area of the phantom with the central voxel also in the center of the grid. For each voxel the relative phase $\Delta\phi$ was calculated as for the central voxel in reference to $(\phi_L + \phi_R)/2$. In fig. 3.10 the spread of the frequency for the γ_5 phantom considered before is shown. Apart from the outer voxel the frequencies lie in a range of $33.56 \pm 0.14\,\mathrm{Hz}$ to $29.13 \pm 0.04\,\mathrm{Hz}$.

Two other examples of frequency distributions are shown in fig. 3.11. On the left, fig. 3.11a shows one of the smoothest distribution found in the phantoms measured. It was derived from an α_6 phantom and displays a frequency range between $31.14 \pm 0.15\,\mathrm{Hz}$ and $33.06 \pm 0.22\,\mathrm{Hz}$, while fig. 3.11b shows one of the more disturbed distribution. For this β_4 phantom the frequency distribution does not only show extreme values at the outer voxels but also an uneven distribution along the x-axis with frequency values ranging from $24.24 \pm 0.18\,\mathrm{Hz}$ to $30.38 \pm 0.22\,\mathrm{Hz}$.

On average, however, the frequency extracted from the central voxel is relatively representative for the entire slice measured and, furthermore, for phantoms the central voxel can easily be found.

In order to investigate the influence of the slice chosen, different slices were measured in two phantoms. In a relatively small and stiff β_6 phantom six slices and in a relatively

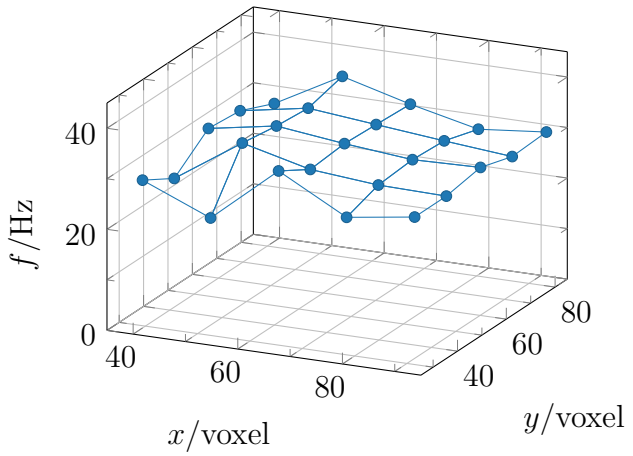

Figure 3.10: *Frequency for Different Voxels:*
The frequency f was determined for 25 different voxels in a γ_5 phantom (100 mm, 5.6 kPa) on a 5×5 grid. Apart from some outer voxel the frequencies lie in a range of 33.56 ± 0.14 Hz to 29.13 ± 0.04 Hz.

large and soft ζ_4 phantom five slices were measured. In both phantoms a central slice was selected (whose position is defined as $z = 0$ mm) - as would have been for a normal measurement - and the other slices were placed with a spacing of 10 mm respectively above and below that slice. An exception is the sixth slice in the β_6 phantom which is only 5 mm apart from the fifth slice. For each slice the frequency of the central voxel was calculated and the results are shown in fig. 3.12. Although six slices were measured for the β_6 phantom, only five could be evaluated, the measurements of the first slice were too distorted to extract a frequency. The frequencies for the β_6 phantom lie in a range of 31.27 ± 0.12 Hz to 32.92 ± 0.13 Hz and for the ζ_4 phantom in a range of 15.07 ± 0.27 Hz to 18.24 ± 0.10 Hz. For later measurements this is encouraging, since - even though it was not possible to choose the exact same slice in different measurements - all selected slices lay in a range of about 15 mm around the middle of the phantom.

Taking the results presented in fig. 3.10 and 3.12 into account, the frequency which is determined in the above explained manner can be considered as a quantity that is relatively stable over the volume of the phantom over the range of about 3 Hz. Additionally, in fig. 3.12 it can be observed that the small and stiff β_6 phantom displays frequencies that are almost twice as high as those in the large and soft ζ_4 phantom, which gives an indication that the hypothesis formulated at the beginning of this section - that the frequency should depend both on the geometry and on the elastic properties of the system - is valid. To investigate this further, the influence of the diameter and of the agar-concentration (thus the elastic properties) on the frequency are presented in the following two sections.

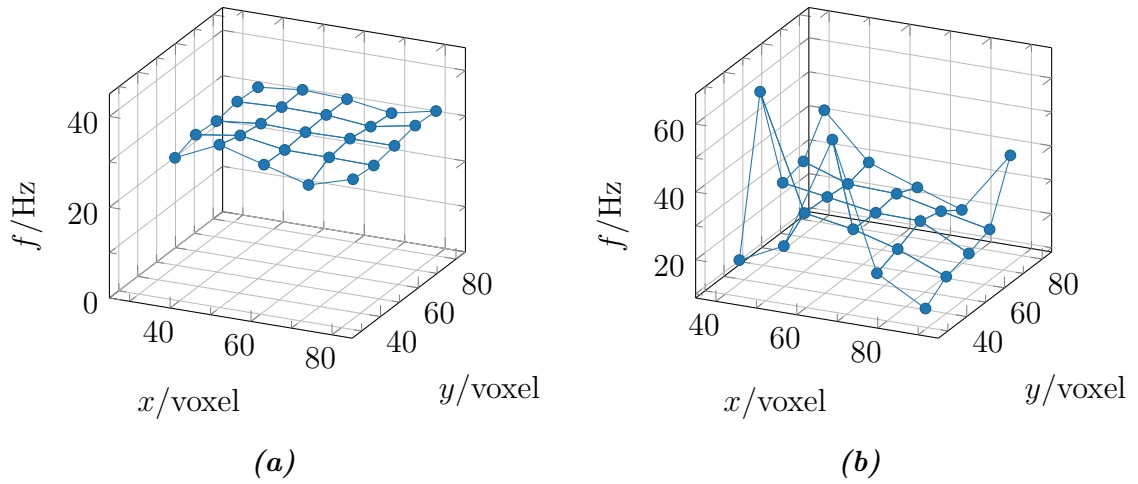

Figure 3.11: *Further Examples of Frequency Distributions in Phantoms:*
(a) shows one of the smoothest distributions found in the phantoms measured with a frequency range between $31.14 \pm 0.15\,\mathrm{Hz}$ *and* $33.06 \pm 0.22\,\mathrm{Hz}$*. This data comes from an* α_6 *phantom (*$85\,\mathrm{mm}, 6.37\,\mathrm{kPa}$*). (b) shows one of the most disturbed distributions with a frequency range between* $24.24 \pm 0.18\,\mathrm{Hz}$ *to* $30.38 \pm 0.22\,\mathrm{Hz}$ *and extreme values at the outer voxels from a* β_4 *phantom (*$90\,\mathrm{mm}, 4.5\,\mathrm{kPa}$*).*

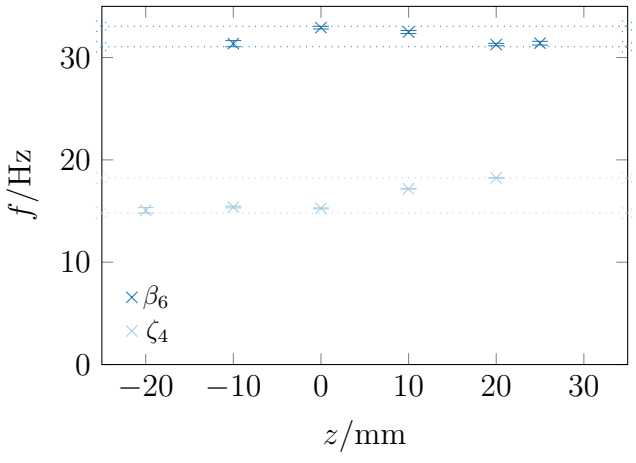

Figure 3.12: *Frequency for Different Slices in Two Phantoms:*
For a small and stiff β_6 *(*$90\,\mathrm{mm}, 6.37\,\mathrm{kPa}$*) and a large and soft* ζ_4 *(*$144\,\mathrm{mm}, 4.5\,\mathrm{kPa}$*) phantom for slices around the central one at* $z = 0\,\mathrm{mm}$ *were measured and the frequency for each slice is plotted here. The frequencies for the* β_6 *phantom lie in a range of* $31.27 \pm 0.12\,\mathrm{Hz}$ *to* $32.92 \pm 0.13\,\mathrm{Hz}$ *and for the* ζ_4 *phantom in a range of* $15.07 \pm 0.27\,\mathrm{Hz}$ *to* $18.24 \pm 0.10\,\mathrm{Hz}$*.*

3.1.2 Influence of size and stiffness

In order to investigate the influence of the size of the phantom, containers with six different diameters were used (phantoms α to ζ, cf. table 2.3). These were filled with hydrogel of different agar concentration to investigate the influence of the diameter for different stiffnesses. For each type of phantom between one and five realizations were produced and a central slice was measured. After the post processing described in section 2.3 the frequency was determined as describes in section 3.1.1.

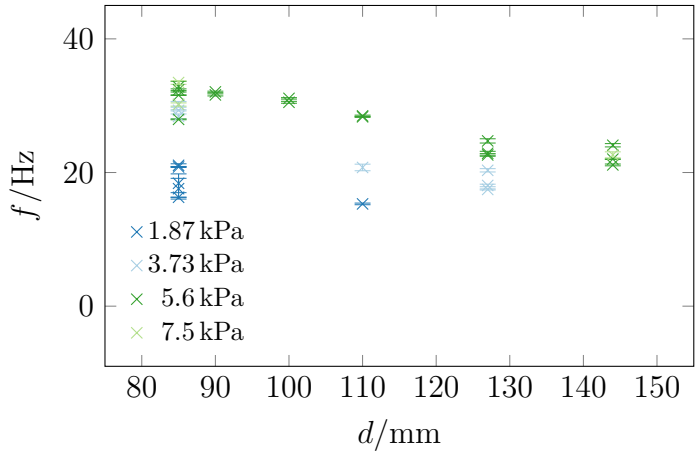

Figure 3.13: *Overview of Frequency vs. Container Size - part one:*
The frequency f is plotted against the diameter d of the container for hydrogels with four different shear moduli (G = 1.87 kPa, 3.37 kPa, 5.6 kPa, 7.5 kPa). The frequencies for different phantom realizations are plotted.

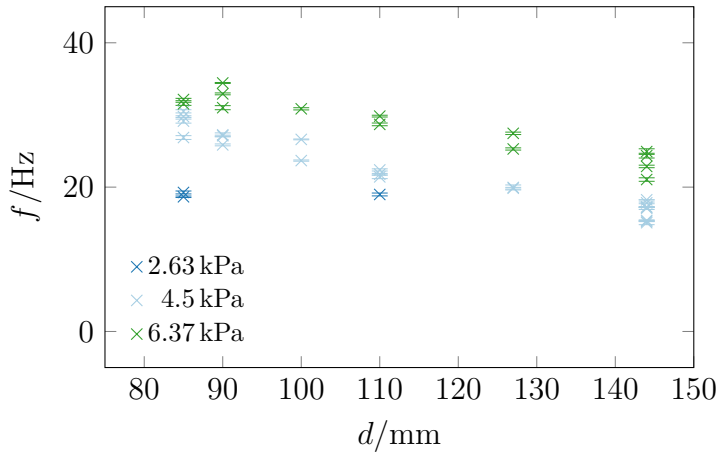

Figure 3.14: *Overview of Frequency vs. Container Size - part two:*
The frequency f is plotted against the diameter d of the container for hydrogels with the three remaining different shear moduli (G = 2.63 kPa, 4.5 kPa, 6.37 kPa). The frequencies for different phantom realizations are plotted.

In fig. 3.13 and 3.14 an overview of the frequencies measured is given. The measurements are split into two plots for better clarity. The frequency f is plotted against the diameter d of the phantom container for hydrogels with different agar concentration and shear moduli. The multiple data points for each kind of phantom represent the different phantom realizations. Not all combinations of diameter and concentration were produced.

It can be seen that the frequencies decline for higher diameters and that softer phantoms tend to exhibit lower frequencies. The error of the individual data points is relatively small since it is propagated from the quite small statistical error on the

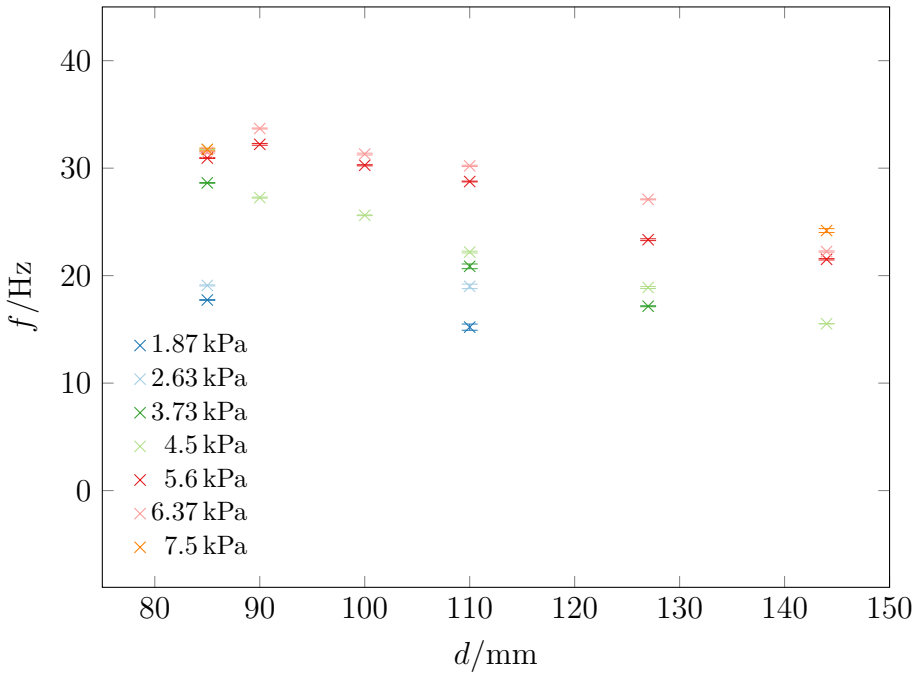

Figure 3.15: *Mean Frequency vs. Container Size:*
The weighted mean of the frequency is calculated over the different phantom realizations and plotted against the diameter of the container for the seven shear moduli. For larger phantom diameters the frequency decreases with exceptions for the smallest diameter of 85 mm *at higher shear moduli. Phantoms with lower shear moduli show also lower frequencies. (In parts already published in [62].)*

phase of each voxel (cf. sec. 3.1.1) and is mostly < 1 Hz and at most 1.5 Hz. The spread between the individual phantom realizations is in the order of around 3 Hz, with a maximum of 5 Hz, which is considerably larger.

The results from the different phantom realizations can be combined by calculating the weighted mean of the frequencies and its error. This is shown in fig. 3.15 where the mean frequency is plotted against the diameter for the seven different shear moduli. For larger diameters the frequency decreases with an exception for the phantoms with relatively high shear moduli of 5.6 kPa and 6.37 kPa at the smallest diameter of 85 mm. Here, the frequency is smaller than for the next larger phantom. Additionally, for this container size the frequencies of the four stiffer phantoms (4.5 kPa − 7.5 kPa) lie very closely together, rendering them virtually indistinguishable.

No analytical solution of oscillations excited in a phantom with the given geometry and boundary conditions to compare these results to. However, in [117] solutions for the resonance frequency of simpler models are given and from those it can be deduced that the frequency in theses phantoms should be inversely proportional to a power of the diameter:

$$f \propto \frac{1}{d^{\gamma}} \tag{3.3}$$

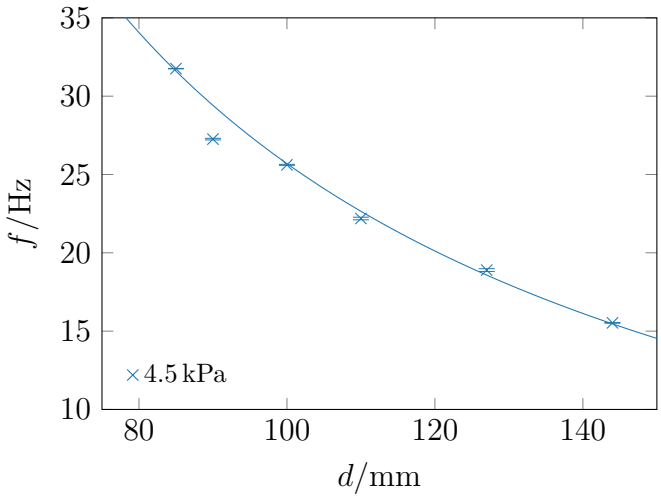

Figure 3.16: *Exemplary Fit for Phantoms with $G = 4.5\,\mathrm{kPa}$: In order to test the hypothesis of eq. 3.3, a hyperbola was fitted to the $f(d)$ data for $G = 4.5\,\mathrm{kPa}$ shown in fig. 3.15. When considering that the errors are underestimated since the spread due to the different phantom realizations is not fully accounted for and the statistic for each data point is quite low, the fit represents the data reasonably well.*

with a coefficient $\gamma > 0$. The data presented in fig. 3.15 does not contradict this prediction which can be seen exemplary in fig. 3.16, where $f(d) = p_1 \cdot 1/d + p_2$ has been fitted to the frequency data for phantoms with the shear modulus $G = 4.5\,\mathrm{kPa}$. When considering that the errors are underestimated since the spread of the different phantom realizations is not fully accounted for and the statistic for each data point is quite low, the fits represent the data reasonably well (cf. fig. 3.13 and 3.14).

In order to investigate the influence of the shear modulus of the phantom material, the frequencies can also be plotted against the modulus which is shown in fig. 3.17 for the six different container sizes. Again the weighted mean frequency over the different phantom realization is used. The error of the shear modulus results from uncertainties in the cooking procedure (cf. sec. 2.2.2.1). It can be observed that the frequency increases with the shear modulus which is expected.

In this plot the unexpected behavior in the smallest container ($d = 85\,\mathrm{mm}$) becomes very evident when the frequency for shear moduli above $G = 4.5\,\mathrm{kPa}$ reaches a plateau at about $f = 32\,\mathrm{Hz}$ and when the frequencies for the $d = 90\,\mathrm{mm}$ phantoms exceed those for the smaller phantom for $G = 5.6\,\mathrm{kPa}$ and $G = 6.37\,\mathrm{kPa}$.

From systems and geometries for which an analytical solution exist (cf. [117]) and from dimensional considerations it can be deduced that the frequency f should be proportional to the square root of the shear modulus G:

$$f \propto \sqrt{G}. \tag{3.4}$$

The data measured - except for the 85 mm-container - roughly follows this behavior. For the container size of $d = 110\,\mathrm{mm}$ the relation of eq. 3.4 to the data is shown in fig. 3.18. It should be again kept in mind that errors for the frequency might be underestimated and that the estimation of the shear modulus G is based on the reliability of Hall's equation 2.2.

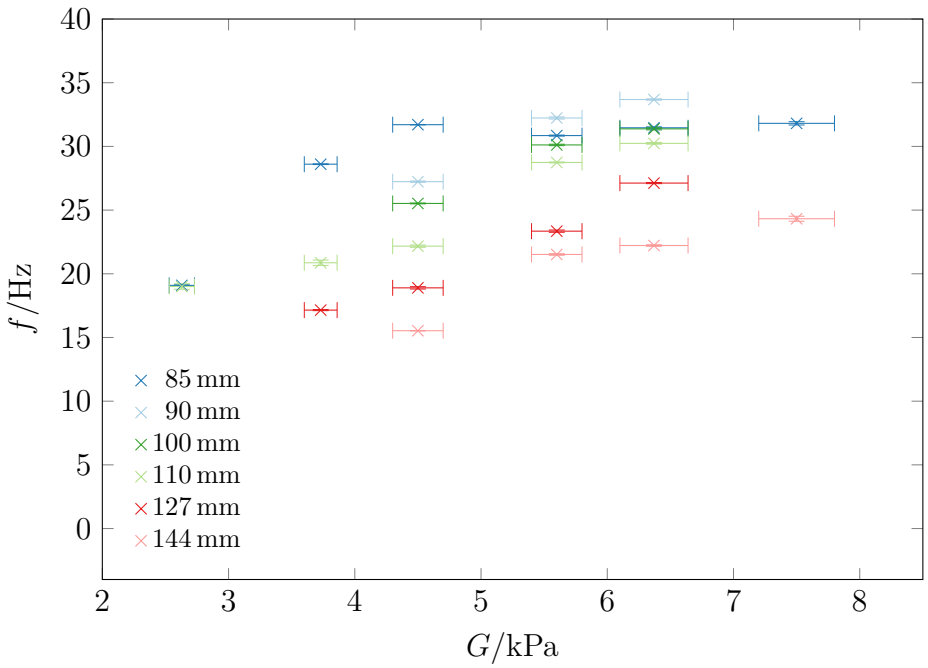

Figure 3.17: *Mean Frequency vs. Shear Modulus:*
The weighted mean of the frequency is calculated over the different phantom realizations and plotted against the shear modulus for six container sizes. For higher shear moduli the frequency increases. For the smallest phantom size the frequencies level out around $f \approx 32\,\mathrm{Hz}$. Overall, larger phantoms have lower frequencies. (In parts already published in [62].)

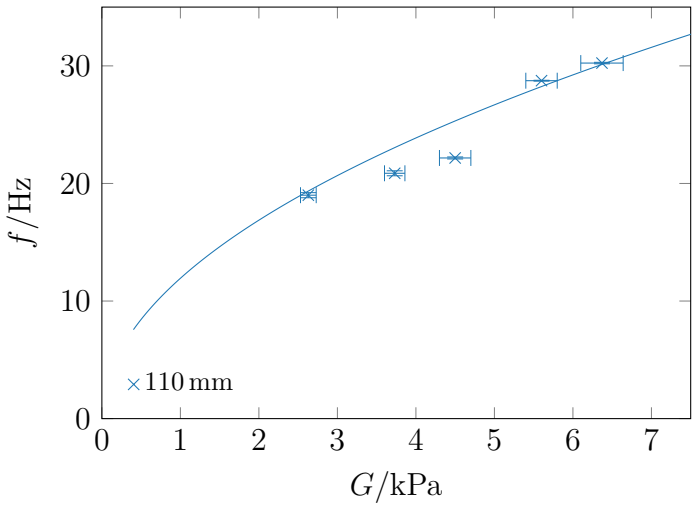

Figure 3.18: *Exemplary Fit for Phantoms with $d = 110\,\mathrm{mm}$:*
In order to test the hypothesis of eq. 3.3 a root function was fitted to the $f(G)$ data for $d = 110\,\mathrm{mm}$ shown in fig. 3.17. As described in fig. 3.16, the errors are underestimated. Thus, the fit does not contradict the data.

3.1.3 Influence of boundary conditions

With the measurements presented in the previous section it could be shown that both the size and the shear modulus - which is contingent upon the agar concentration - influence the frequency extracted form the oscillation in the relative phase. It is presumed that the basic of these findings can be transfered later on to *in vivo* measurements on human brains.

Before considering a comparison, however, the boundary conditions should be taken into account. The brain tissue is coupled to the skull via complicated layers of meninges (cf. sec. 1.3.1.1, fig. 1.19), while up to now the agar hydrogel representing the brain tissue in the phantoms was coupled directly to the container wall representing the skull (cf. sec. 2.2.2).

In order to investigate whether and what kind of influence an intermediate layer could have on the behavior of the relative phase $\Delta\phi$, several realizations of six phantoms with different kind of sponges as an intermediate layer were used (phantoms λ_1 to ν_2, cf. table 2.6). Since the inner diameter of the container outlaid with the sponge is $d = 108\,\mathrm{mm}$ and the hydrogel used had a shear modulus of $G_1 = 5.6\,\mathrm{kPa}$ and $G_2 = 6.37\,\mathrm{kPa}$ respectively, these λ, μ and ν phantoms are compared to δ_5 and δ_6 phantoms with a diameter of $d = 110\,\mathrm{mm}$ and a shear modulus of $G_1 = 5.6\,\mathrm{kPa}$ and $G_2 = 6.37\,\mathrm{kPa}$ respectively as well.

When comparing the relative phase data plotted against τ for the phantoms with interlining, eight out of 14 phantom realizations showed a disturbed behavior (comparable to those displayed in fig. 3.7) for $\tau \geq 40\,\mathrm{ms}$. In the undisturbed time frame, there were always two extrema located. For the λ_1 and all the phantoms with shear modulus G_2 actually no phantom realization showed data that was undisturbed for a longer time τ. This is not totally unexpected, since the boundary layer allows for additional degrees of freedom, which might influence the behavior of the phantom material.

For this reason, only the first two extrema were used for all phantoms - also for the δ phantoms used for comparison - to estimate the frequency in order to increase the comparability. Otherwise the frequency and its error was determined as described previously (cf. sec. 3.1.1) and the results are plotted in fig. 3.19 comparing the δ phantoms without interlining to the three phantoms with different types of interlayer.

On the left are the frequencies for the softer phantoms with $G = 5.6\,\mathrm{kPa}$ and on the right those for the slightly stiffer ones with $G = 6.37\,\mathrm{kPa}$. It can be observed that for both shear moduli the additional interlayer seems to increase the frequency. For $G = 5.6\,\mathrm{kPa}$ the coarsely pored rubber sponge (phantom λ_5) shows a significantly higher increase in the frequency than both the other two interlayers, while for $G = 6.37\,\mathrm{kPa}$ all three interlayers had a similar influence.

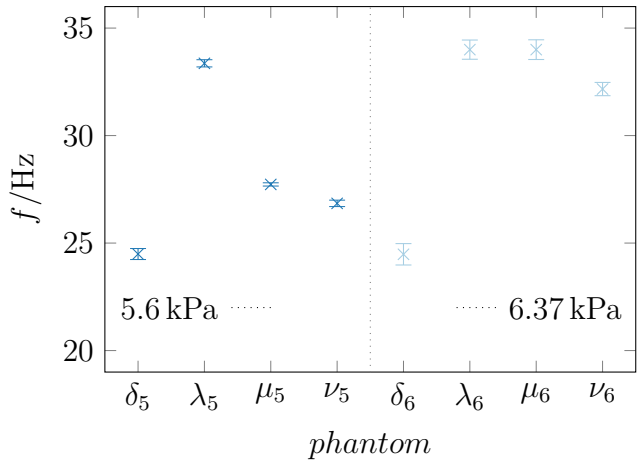

Figure 3.19: *Influence of Boundary Conditions:*
Four different boundary conditions for two different shear moduli are compared. The mean frequency of a δ phantom (direct connection between hydrogel and container, $d = 110\,\mathrm{mm}$) is compared to the frequencies of λ, μ and ν phantoms (phantoms with sponge interlayer (coarsely, fine and medium pored sponges)) for $G_1 = 5.6\,\mathrm{kPa}$ (left) and $G_2 = 6.37\,\mathrm{kPa}$ (right). For both shear moduli, it seems that all interlayers increase the frequency.

3.2 Inhomogeneous Phantoms

After it could be shown that the stiffness and size of homogeneous phantoms influence their response to a shock excitation in the previous section, in this section results from inhomogeneous phantoms are described with the aim to asses possible contrasts inside a phantom as well as the spatial resolution.

For that, three phantoms (ϑ_1 to ϑ_3) with two layers, a phantom η with two cubic hydrogel inclusions with a stiffness different than the surrounding material, and a phantom κ with a cystic inclusion were investigated.

3.2.1 Two Layered Phantoms

Three phantoms were investigated which were fabricated as described in sec. 2.2.2.2 and consisted of two parts of hydrogel with different agar concentrations. A time series over 120 ms was acquired for each phantom and the images were processed as described in sec. 2.3.

In the figures 3.20, 3.23, and 3.26 seven exemplary phase images for different τ-values are shown per phantom (***(b)-(h)***) as well as one corresponding magnitude image ***(a)*** in which the two layers can be clearly distinguished. In the phase images for $\tau = 0\,\mathrm{ms}$ ***(b)***, the two halves cannot be distinguished as the phase is homogeneous over the whole phantom. In the phase images for larger τ-values, an oscillation can again be observed as could be for the homogeneous phantoms (cf. fig. 3.1). For the two layered phantoms, however, a discrete oscillation in each of the halves emerges through which the two parts become distinguishable from each other for the values of τ depicted here. Apart from this signature, in multiple phase images unwrapping artifacts are visible (cf. fig. 3.20e, 3.23f or 3.26d).

For further analysis, two plots are shown for each phantom. In the figures 3.21, 3.24, 3.27 the relative phase $\Delta\phi$ along a line cutting horizontally through the middle of each phantom is shown for selected values of τ (cf. fig. 3.4 for homogeneous phantoms).

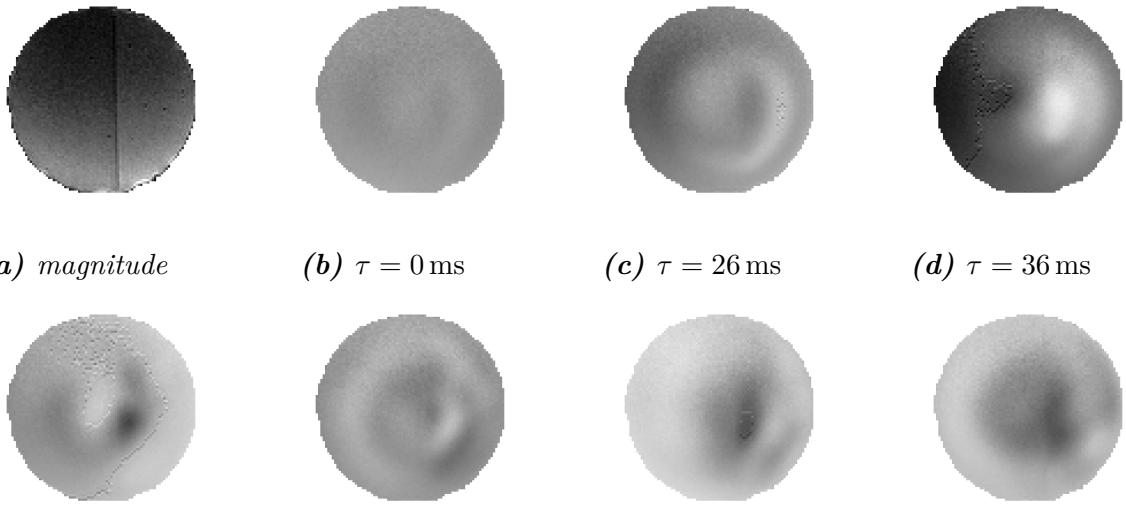

(a) *magnitude* **(b)** $\tau = 0\,\text{ms}$ **(c)** $\tau = 26\,\text{ms}$ **(d)** $\tau = 36\,\text{ms}$

(e) $\tau = 48\,\text{ms}$ **(f)** $\tau = 58\,\text{ms}$ **(g)** $\tau = 86\,\text{ms}$ **(h)** $\tau = 116\,\text{ms}$

Figure 3.20: *Two Layered ϑ_1 Phantom - Exemplary Magnitude and Phase Images: (a) shows a magnitude image. The two halves can be clearly distinguished with the right side ($G_1 = 3.73\,\text{kPa}$) appearing lighter than the stiffer left side ($G_2 = 5.6\,\text{kPa}$). For $\tau = 0\,\text{ms}$ (b) the phase has a homogeneous phase and the two sides cannot be distinguished. For larger τ-values ((c) - (h)) a discrete oscillation in each of the halves emerges and a distinction between the layers is possible. In (d), (e) and (g) unwrapping artifacts can be seen.*

The border between the two halves is indicated with a black dotted line in each plot.

In the figures 3.22, 3.25, 3.28 the relative phase for one voxel in each layer is plotted against τ. The voxels were all chosen to lie ten voxels away from the border between the two halves on the horizontal line through middle of the phantom.

When considering the cuts through the middle of the phantoms, different behavior can be observed. The plots of the ϑ_1 phantom in fig. 3.21 show not much similarity with the cuts through the homogeneous phantom in fig. 3.4. For $\tau = 26\,\text{ms}$ and $\tau = SI48\text{ms}$ the endpoints show a significant asymmetry. The border between the two layers (indicated by the dotted line) cannot easily be inferred from the data, although, when considering the global phase information presented in the phase images in fig. 3.20 there the distinction is possible.

For the ϑ_2 phantom the plots in fig. 3.24 show on the right side a high resemblance to the homogeneous phantom in a way that this side seems to perform a discrete oscillation. The left half on the other hand shows mostly a lot less dynamic, apart from $\tau = 72\,\text{ms}$ where an inverse oscillation compared to the right layer can be observed. For this phantom the position of the border could have been estimated from the data.

It can be seen that the phase in fig. 3.27 for the ϑ_3 phantom (the only one where the left side is softer than the right side) shows a different behavior than the other two phantoms. For one, both sides - but especially the softer left side - show a much higher

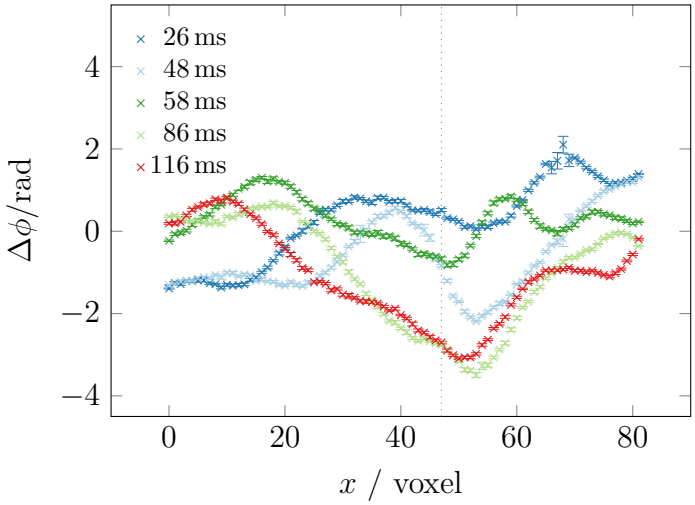

Figure 3.21: *Two Layered ϑ_1 Phantom - $\Delta\phi$ vs. Voxel:*
The relative phase $\Delta\phi$ along horizontal cuts through the phantom is plotted for selected τ-values. The data shows a distinctly different behavior from what could be observed in the homogeneous phantoms (cf. fig. 3.4). In these plots the border between the two layers is indicated by the dotted line but cannot be easily inferred from the data.

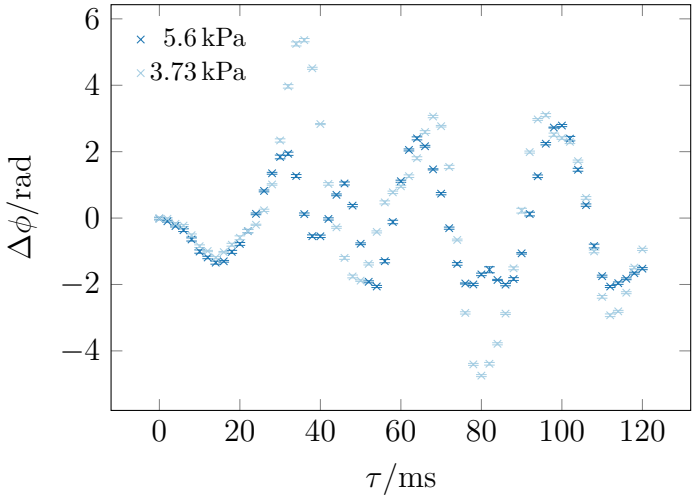

Figure 3.22: *Two Layered ϑ_1 Phantom - Time Series for Two Voxels:*
$\Delta\phi$ is plotted versus τ for one voxel in each layer. The voxels were chosen to lie ten voxels away from the border between the tow halves. Each voxel shows an oscillation over time with quite similar frequency. The data for the stiffer $G_2 = 5.6\,\mathrm{kPa}$ side, however, shows a slightly disturbed oscillation with lower amplitude.

dynamic range. Also, the division between the two layers is much more pronounced (in some cases the phase changes for more than 2π) and can be determined from this data very precisely. However, after the measurements it was verified that the two layers were still attached to each other.

When considering the time series for the two selected voxels inside the different layers for the ϑ_1 phantom in fig. 3.22, contradictory to what was expected from the cuts in fig. 3.21, an oscillation can be observed in both halves of the phantom. Here, the frequencies lie in each others margins of error ($f_{5.6} = 15.2 \pm 0.4\,\mathrm{Hz}$, $f_{3.73} = 14.9 \pm 0.5\,\mathrm{Hz}$). In this figure, the both halves can be distinguished for some τ-values mostly by the difference in the amplitude of the oscillation.

Fig. 3.25 shows the time series for the ϑ_2 phantom where the oscillations are more disturbed than in the ϑ_1 phantom. Especially the stiffer $G_2 = 4.5\,\mathrm{kPa}$ half shows a very low dynamic and no clear oscillation, but also the beginning of the $G_1 = 3.73\,\mathrm{kPa}$ half the time series is more disturbed than in the ϑ_1 phantom. A frequency estimation for the stiffer left side seems not justifiable. The frequency for the softer right side of

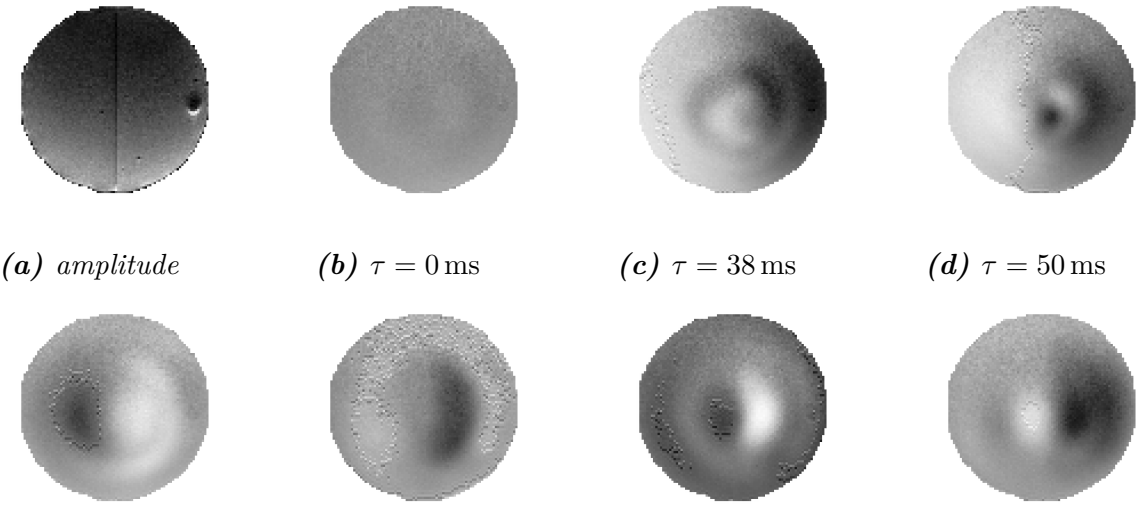

(a) *amplitude* **(b)** $\tau = 0\,\mathrm{ms}$ **(c)** $\tau = 38\,\mathrm{ms}$ **(d)** $\tau = 50\,\mathrm{ms}$

(e) $\tau = 72\,\mathrm{ms}$ **(f)** $\tau = 90\,\mathrm{ms}$ **(g)** $\tau = 102\,\mathrm{ms}$ **(h)** $\tau = 116\,\mathrm{ms}$

Figure 3.23: *Two Layered ϑ_2 Phantom - Exemplary Magnitude and Phase Images: (a) shows a magnitude image. The two halves can be clearly distinguished with the right side ($G_1 = 3.73\,\mathrm{kPa}$) appearing lighter than the stiffer left side ($G_2 = 4.5\,\mathrm{kPa}$). Additionally, an air bubble can be seen on the far left. It has, however, no significant effect on the phase. For $\tau = 0\,\mathrm{ms}$ (b) the phase has a homogeneous phase and the two sides cannot be distinguished. For larger τ-values ((c) - (h)) a discrete oscillation in each of the halves emerges and a distinction between the layers is possible. In all of these phase images for τ 0 ms there are unwrapping artifacts present.*

3.73 kPa leads to $f_{3.73} = 15.2 \pm 0.5\,\mathrm{Hz}$.

On the other hand - as noted above - the ϑ_3 phantom shows oscillations with a much higher dynamic, notably in both layers (cf. fig. 3.28). Here, the frequencies of the softer $G_2 = 2.63\,\mathrm{kPa}$ side is somewhat lower than the one for the stiffer side ($f_{2.63} = 14.5 \pm 0.1\,\mathrm{Hz}$, $f_{3.73} = 15.1 \pm 0.3\,\mathrm{Hz}$). The relative phase of the two selected voxels differs from each other for almost every τ-value after $\tau = 36\,\mathrm{ms}$. For all three phantoms it can be observed that in the beginning of the time series the two chosen voxel show the same behavior.

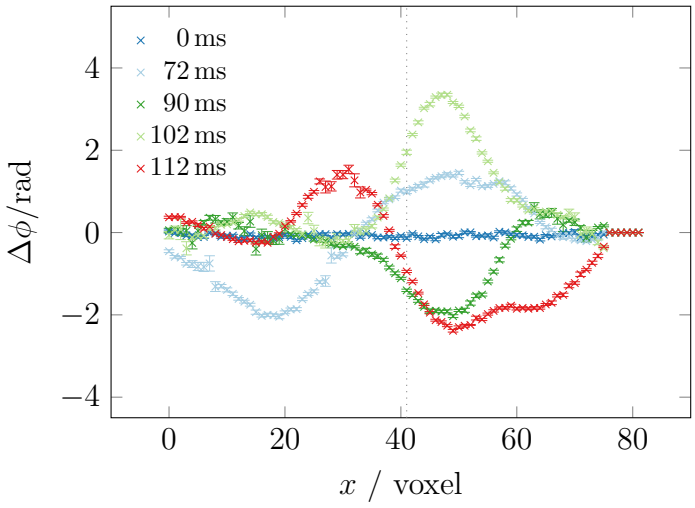

Figure 3.24: *Two Layered ϑ_2 Phantom - $\Delta\phi$ vs. Voxel:*
The relative phase Deltaϕ along horizontal cuts through the phantom is plotted for selected τ-values. The right side shows a distinct oscillation similar to the one observed in homogeneous phantoms. The stiffer left side, however, shows mostly a lot less dynamic than the right side (apart from $\tau = 72\,\mathrm{ms}$). It would be possible to roughly infer the border between the two layers from the data, which is indicated by the dotted line.

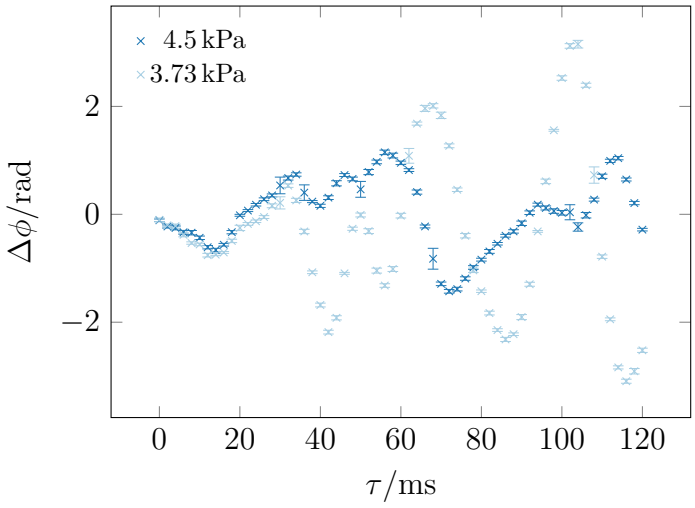

Figure 3.25: *Two Layered ϑ_2 Phantom - Time Series for Two Voxels:*
$\Delta\phi$ is plotted versus τ for one voxel in each layer. The voxels were chosen to lie ten voxels away from the border between the tow halves. The stiffer side shows a much lower dynamic than the voxel in the softer side. A frequency determination does not seem justifiable. For the voxel in the $G_1 = 3.73\,\mathrm{kPa}$ side the data at the beginning of the time series seems more distorted than for the ϑ_1 phantom.

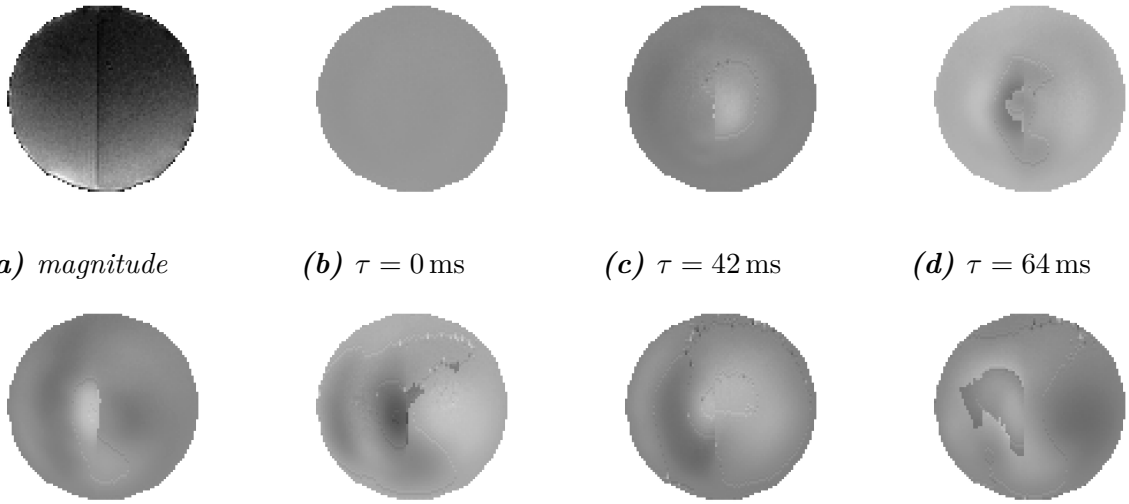

(a) *magnitude* **(b)** $\tau = 0\,\mathrm{ms}$ **(c)** $\tau = 42\,\mathrm{ms}$ **(d)** $\tau = 64\,\mathrm{ms}$

(e) $\tau = 80\,\mathrm{ms}$ **(f)** $\tau = 96\,\mathrm{ms}$ **(g)** $\tau = 104\,\mathrm{ms}$ **(h)** $\tau = 112\,\mathrm{ms}$

Figure 3.26: *Two Layered ϑ_3 Phantom - Exemplary Magnitude and Phase Images: (a) shows a magnitude image. The two halves can be clearly distinguished with the right side ($G_1 = 3.73\,\mathrm{kPa}$) appearing darker than the softer left side ($G_2 = 2.63\,\mathrm{kPa}$). For $\tau = 0\,\mathrm{ms}$ (b) the phase has a homogeneous phase and the two sides cannot be distinguished. For larger τ-values ((c) - (h)) a discrete oscillation in each of the halves emerges and a distinction between the layers is possible. In all of these phase images for $\tau\,0\,\mathrm{ms}$ there are unwrapping artifacts present.*

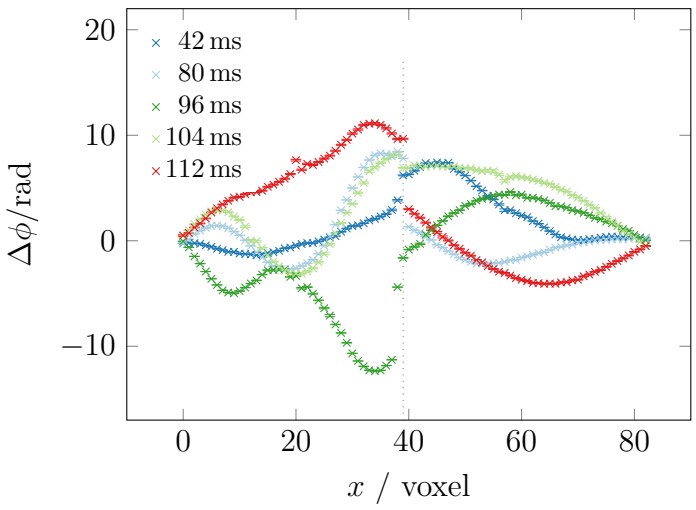

Figure 3.27: *Two Layered ϑ_3 Phantom - $\Delta\phi$ vs. Voxel: The relative phase $\Delta\phi$ along horizontal cuts through the phantom is plotted for selected τ-values. The two sides show a distinctly different behavior form each other. In each half an oscillation can be observed, with the softer left side having a much higher dynamic range. The border between the two layers - indicated by the dotted line - can be nicely inferred from the data.*

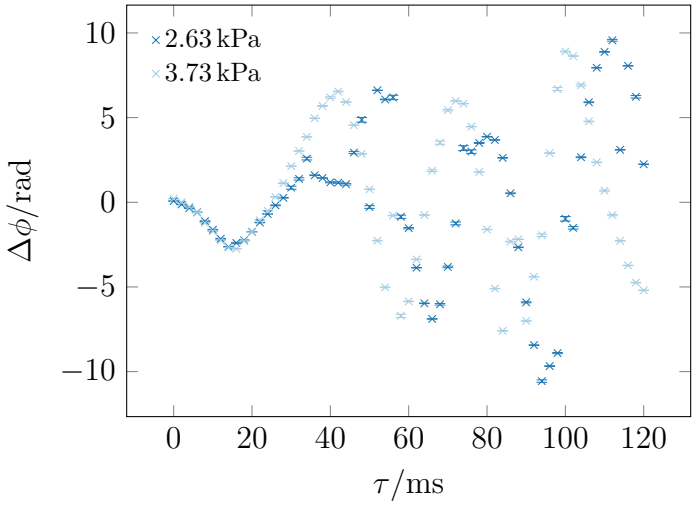

Figure 3.28: *Two Layered ϑ_3 Phantom - Time Series for Two Voxels:*
$\Delta\phi$ is plotted versus τ for one voxel in each layer. The voxels were again chosen to lie ten voxels away from the border between the two halves. Both voxels show an oscillation with a high dynamic range. The data for the $G_2 = 2.63\,\mathrm{kPa}$ side shows an unusual behavior up to about $\tau \approx 45\,\mathrm{ms}$.

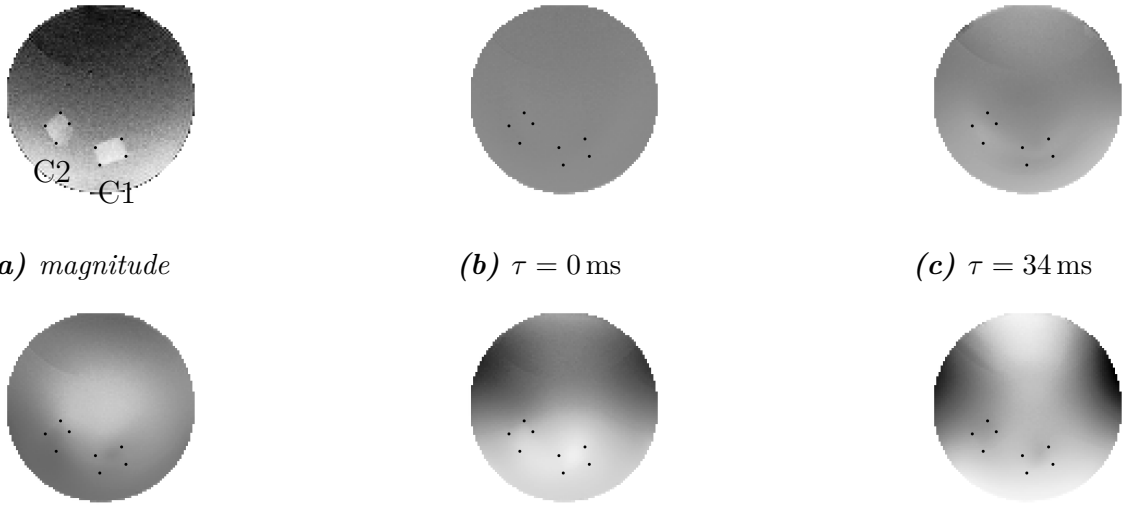

(a) *magnitude* ***(b)*** $\tau = 0\,\mathrm{ms}$ ***(c)*** $\tau = 34\,\mathrm{ms}$

(d) $\tau = 44\,\mathrm{ms}$ ***(e)*** $\tau = 90\,\mathrm{ms}$ ***(f)*** $\tau = 100\,\mathrm{ms}$

Figure 3.29: *Phantom η with Two Cubic Inclusions - Exemplary Magnitude and Phase Images:*
In (a) the magnitude image shows the position of the two softer cubic inclusions very clearly. Their corners are marked with black dots which are also shown in the phase images to guide the eye. In the upper half a semi circular dark shadow can be seen which results form a ghosting artifact. The phase image for $\tau = 0\,\mathrm{ms}$ (b) shows a homogeneous gray value. In the phase images for larger τ-values ((c) - (f)) the cubes cannot be distinguished clearly, but sometimes slight local variations in the shade of gray can be observed.

3.2.2 Cubic Inclusion

In order to show the possibility of creating a spatially resolved contrast based on the mechanical properties in phantoms, phantom η with two cubic inclusions was investigated. The properties of the phantom are described in table 2.4. Again a time series over 120 ms was acquired and the images were processed as described in section 2.3.

In fig. 3.29 an amplitude image (a) is shown in which the two cubes are clearly visible. In the five exemplary phase images for different τ-values ((b) to (f)) the position of the cubes are indicated with black dots at their corners. In the phase images the cubes cannot be distinguished clearly, but sometimes slight local variations in the shade of gray can be observed. Further data processing was done to explore whether a clear signature of the cubes can be achieved.

Correspondingly to fig. 3.4 the relative phase along a line through each of the cubes, respectively, was calculated and plotted for different τ-values in fig. 3.30. The position of each cube is indicated in the two figures with dotted lines, in fig. 3.30a for the lower, right cube **C1** and in fig. 3.30b for the upper, left one **C2**. An oscillation comparable to the one observed in homogeneous phantoms is present here, too. For some τ-values

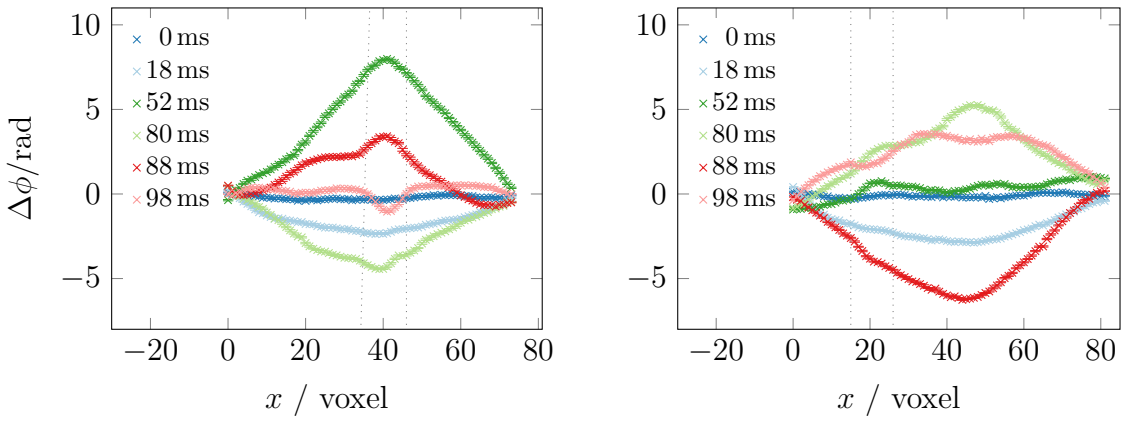

(a) *Cube* ***C1*** ***(b)*** *Cube* ***C2***

Figure 3.30: *Phantom η - Cuts Through the Middle of Each Cube:*
The relative phase Δφ along a line through the middle of each cube for several τ-values is plotted. The positions of the cubes are indicated by the dotted lines, in (a) for cube ***C1*** *and in (b) for cube* ***C2****. The overall form of the cuts show a similar characteristic to the one found for homogeneous phantoms. For some τ-values, however, a deviation can be seen at the location of the cube (most prominently for* ***C1*** *at τ = 98 ms). The signatures of the cubes are more prominent for* ***C1*** *than for* ***C2****.*

a deviation from the expected behavior can be seen at the location of the cube, most prominently for **C1** at $\tau = 98\,\text{ms}$. In some cases the boundaries of the cubes can be deduces quite accurately from the extent of the deviation (e.g. the left boundary of **C2** at $\tau = 98\,\text{ms}$) while at other times a clear distinction of the boundaries is not possible even when the cube leaves a signature (e.g. right boundary of **C1** at $\tau = 88\,\text{ms}$).

The line chosen for fig. 3.30 was a line through the middle of the cube. In fig. 3.31 horizontal cuts through the phantom at different y-values (from line 57 to line 87) are shown for $\tau = 100\,\text{ms}$. The maximal horizontal extend of both cubes is indicated, while cube **C1** extends vertically between $77 \leq y \leq 86$ and **C2** between $63 \leq y \leq 77$. Especially for **C1** at $y = 72$ (maybe even at $y = 67$) it can be observed that the cube leaves a signature above its real position. **C2** also shows a wide signature at $y = 62$, even though its upper corner lies as $y = 63$ (cf. the location of the cubes in fig. 3.29a). On the other hand, there is no significant signature in the cuts below the cubes ($y = 87$ for **C1** and $y = 82$ for **C2**).

Since the signatures of the cubes in the phase images and therefore also in the cut plots is predominated by the effect of the global oscillation the gradient of the phase was calculated, which we call phase strain ϵ_ϕ. This was done by smoothing the post processed phase data using a Gaussian filter with a standard deviation for the Gaussian kernel of $\sigma = 0.1$ and then calculating the absolute value of the phase gradient in y-direction (the main direction of the movement) using central differences:

$$|\epsilon_\phi| = \left|\frac{\partial \phi}{\partial y}\right|. \tag{3.5}$$

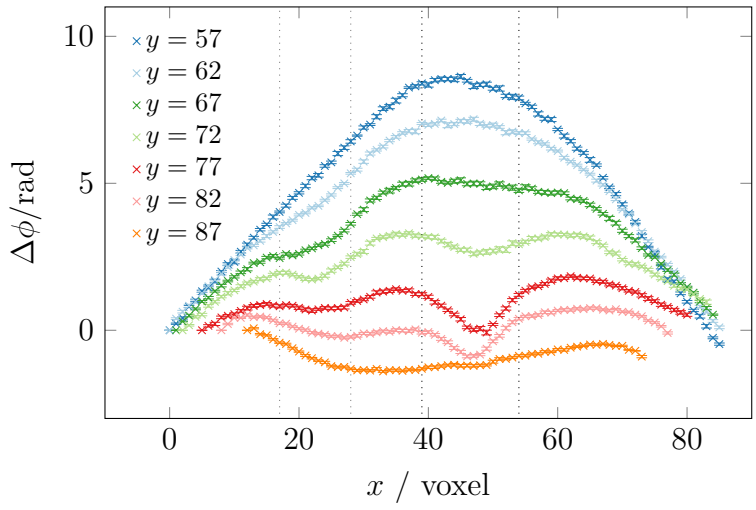

Figure 3.31: *Phantom η - $\Delta\phi$ vs. Voxels at Different y-values:*
For $\tau = 100\,\mathrm{ms}$ the $\Delta\phi$ is plotted along different horizontal lines for $57 \leq y \leq 87$. The maximal horizontal extend of the cubes is indicated by the dotted lines. ***C1*** *in the middle extends vertically between $77 \leq y \leq 86$ and* ***C2*** *between $63 \leq y \leq 77$.*

In fig. 3.32 a series of phase strain images of the phantom for different τ-values is shown. In these images blue indicates a low, red a high absolute phase strain. The corners of the cubes are again marked by black dots. In these images the cubes leave a much clearer signature of higher $|\epsilon_\phi|$-values than in the phase images (cf. fig. 3.29). While not always both cubes are visible altogether, when they are the borders are very well defined.

Additionally to the signatures of the cubes some other features are visible in the phase strain images, which result from artifacts. In all images parts of a semi circle with apparently higher phase strain values in the upper part of the phantom can be seen. This is the result of a ghosting artifact and can also be observed to a lesser degree in the amplitude and phase images in fig. 3.29. In other images, lines (especially in the lower part of the phantom) are visible. These are residuals of phase unwrapping artifacts.

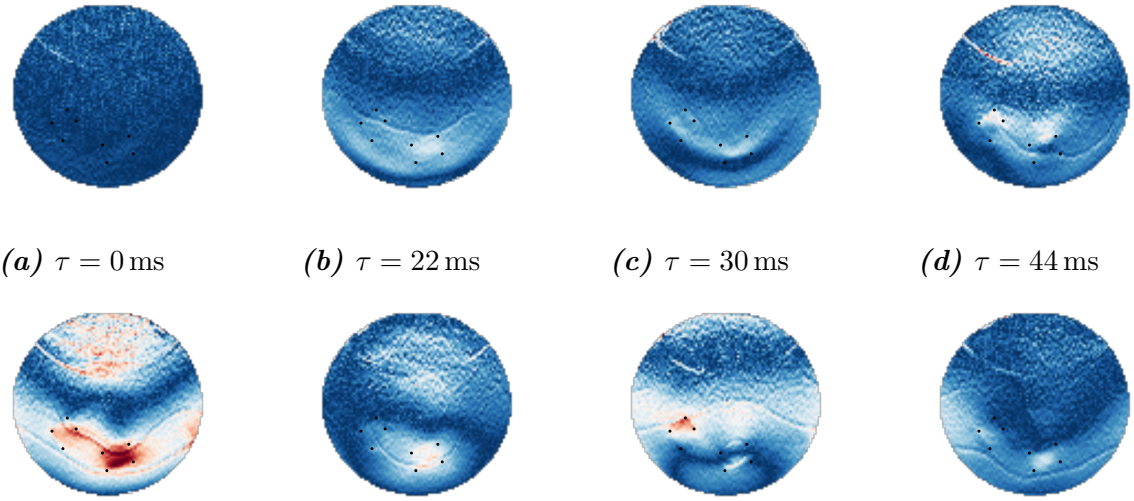

(a) $\tau = 0\,\mathrm{ms}$ ***(b)*** $\tau = 22\,\mathrm{ms}$ ***(c)*** $\tau = 30\,\mathrm{ms}$ ***(d)*** $\tau = 44\,\mathrm{ms}$

(e) $\tau = 54\,\mathrm{ms}$ ***(f)*** $\tau = 70\,\mathrm{ms}$ ***(g)*** $\tau = 90\,\mathrm{ms}$ ***(h)*** $\tau = 120\,\mathrm{ms}$

Figure 3.32: *Phantom η - Exemplary Absolute Phase Strain Images:*
In the phase strain images blue indicates a low, red a high absolute phase strain $|\epsilon_\phi|$. The corners of the cubes are again marked by black dots. In these images the cubes leave a much clearer signature of higher $|\epsilon_\phi|$-values. Additionally to the signatures of the cubes some features resulting from artifacts can be seen. The semicircle in the upper half of the phantom results from a ghosting artifact, while the lines mostly present in the lower half of the phantom result from unwrapping artifacts.

(a) *magnitude* **(b)** *phase image* **(c)** *phase strain image*

Figure 3.33: *Phantom κ with Fluid Filled Inclusion:*
In the magnitude image (a) the fluid filled inclusion is visible very well. In the phase image (b) taken at $\tau = 50\,\mathrm{ms}$ the lower part of the inclusion is also visible as a darker area, while the upper part is not visible so well. The lighter line in the upper part and the darker line in the lower part result from unwrapping artifacts. In the phase strain image (c) the inclusion is again very prominently visible as a dark blue area. Dark blue indicates a very low phase strain, which is comprehensible due to the incompressibility of water.

3.2.3 Fluid Filled Inclusion

After exploring the signature of a hydrogel inclusion in the previous section, the feasibility of detecting a cystic, fluid filled inclusion is investigated here. To mimic this, phantom κ (a water filled balloon inside a $G = 4.9\,\mathrm{kPa}$ hydrogel phantom - cf. sec. 2.2.2.2) was investigated. Here, in contrast to the previous studies however, only a measurement with ten averages at $\tau = 50\,\mathrm{ms}$ was taken.

The magnitude, phase and the absolute phase strain image are displayed in figure 3.33. The fluid filled inclusion is readily visible in the magnitude image (a) due to the much higher T_1- and T_2-values of water (cf. table 1.1). In the phase image (b), the inclusion is also visible, especially in the lower part. The two lines in the phase image are phase unwrapping artifacts. In the phase strain image (c) the inclusion is again visible much more clearly than in the phase image. Since dark blue colors refer to low and red to high $|\epsilon_\phi|$-values, it can be seen very nicely that due to the incompressibility of water and the fact that it has no room to flow the inclusion exhibits also a very low phase strain. As in the phase images two lines resulting from phase unwrapping artifacts are prominent.

In fig. 3.34 the relative phase along horizontal cuts through the phantom is plotted for different y-values. The maximal horizontal extent of the inclusion is indicated by the dotted lines, while it extents vertically between $40 \leq y \leq 62$. It can be seen, that for the cuts through the inclusion ($y = 45$, 49, and 55) $\Delta\phi$ shows a very clear signature as it remains virtually constant. This is a different behavior than for the cubic inclusions (cf. fig. 3.31) where the signature is more dent like. Additionally, no influence of the inclusion can be detected for the cuts directly above ($y = 39$) and below ($y = 63$) the inclusion.

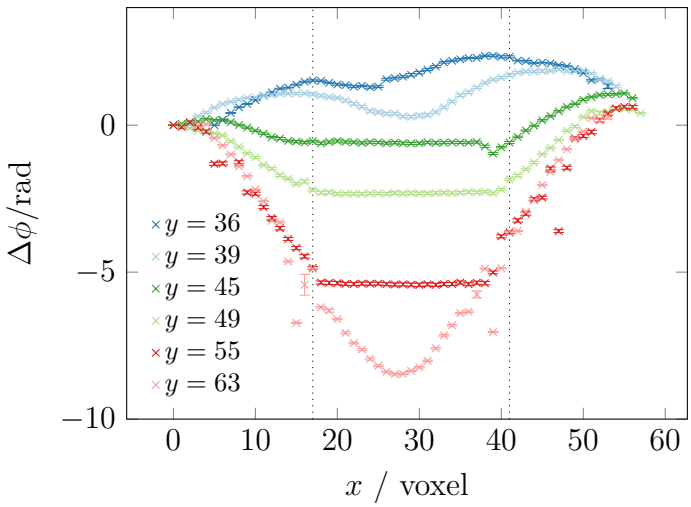

Figure 3.34: *Phantom κ - $\Delta\phi$ vs. Voxel at Different y-values: The relative phase $\Delta\phi$ is plotted along six lines with different y-values through the phantom. The maximal extend of the inclusion in x-direction is indicated by the dotted lines, while it extents vertically between $40 \leq y \leq 62$. For the cuts through the inclusion ($y = 45, 49, 55$) $\Delta\phi$ shows a very clear signature as it remains virtually constant. However, there is no signature of the inclusion in the cuts directly above ($y = 39$) or below ($y = 63$) the inclusion. In the plot for $y = 55$ and $y = 63$ phase unwrapping artifacts are present.*

3.3 Human Volunteers

During the investigation of the homogeneous and inhomogeneous phantoms different concepts of analyzing the phase data have been utilized. Examining the oscillation of the relative phase of the voxels and their frequencies seems to provide a measure for the bulk properties (cf. sec. 3.1.2). The relative phase along a line or phase strain images, on the other hand, have turned out to be feasible approaches to investigate local structures (cf. sec. 3.2).

In this section these concepts are transfered to the measurements of healthy human volunteers which were taken according to the description in sec. 2.2.1. In order to keep the scan time short, the time domain was sampled more coarsely than for the phantoms (cf. tables 2.1 and 2.2). The images were processed as described in sec. 2.3. First the results for the gradient setting with $\delta = 5.36\,\text{ms}$, $\delta\Delta = 40\,\text{ms}$ and $G = 25.4\,\text{mT}\,\text{m}^{-1}$ are presented in the sections 3.3.1 to 3.3.3 and later compared to the second gradient setting in section 3.3.5. From the magnitude images the dimensions of the brains in the chosen slice were determined. This data is shown in the appendix A.1.

3.3.1 Phase images

In fig. 3.35 a high resolution magnitude image (a) and seven phase images for different τ-values (b - h) for volunteer **id09** are displayed to show the general behavior of a human brain to the shock excitation. Similar to the behavior observed in phantoms (cf. fig. 3.1, 3.20 or 3.29) the phase image for $\tau = 0\,\text{ms}$ (b) displays an almost homogeneous gray value. Over time an oscillatory behavior can be observed, however, the two

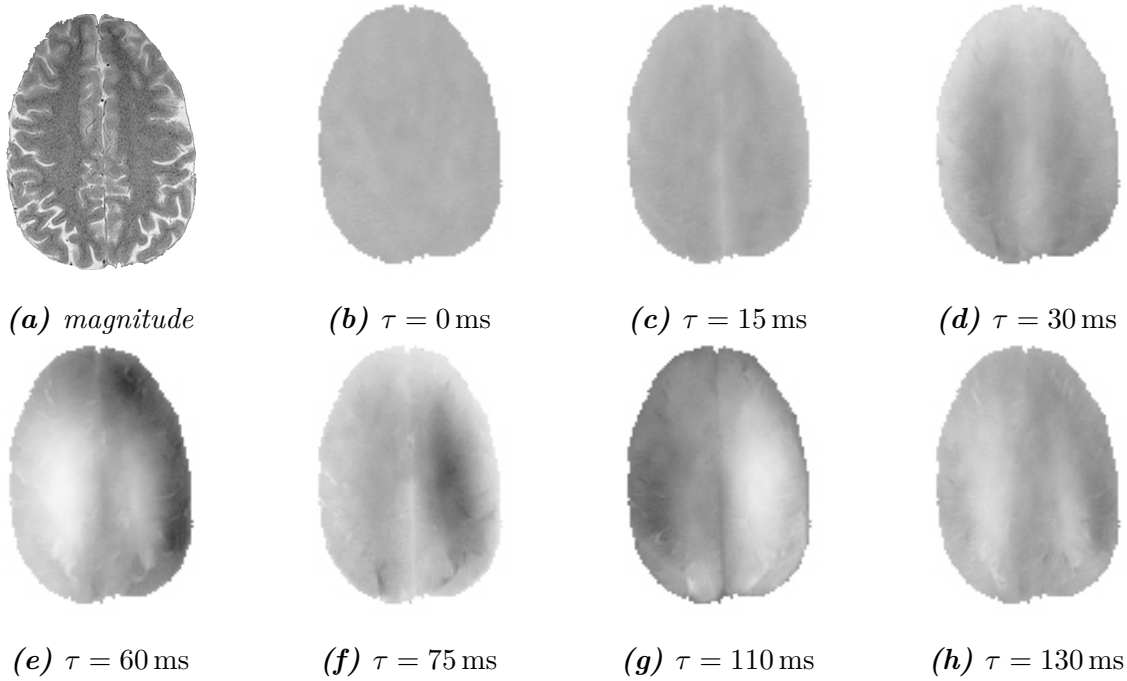

(a) *magnitude* ***(b)*** $\tau = 0\,\text{ms}$ ***(c)*** $\tau = 15\,\text{ms}$ ***(d)*** $\tau = 30\,\text{ms}$

(e) $\tau = 60\,\text{ms}$ ***(f)*** $\tau = 75\,\text{ms}$ ***(g)*** $\tau = 110\,\text{ms}$ ***(h)*** $\tau = 130\,\text{ms}$

Figure 3.35: *Exemplary Magnitude and Phase Images:*
*(a) shows a high resolution magnitude image, while (b) - (h) show phase images for different τ-values for volunteer **id09**. For $\tau = 0\,\text{ms}$ (b) the phase image displays an almost homogeneous gray value. Similar to the behavior observed in phantoms, the brain reacts to the shock excitation at higher τ-values with an oscillatory behavior, though, with a distinct oscillation in each hemisphere. The falx cerebri between the hemispheres can be distinguished and especially for later τ-values some sulci that can also be seen in the magnitude image become visible in the phase images. (In parts already published in [62].)*

hemispheres (cf. sec. 1.3.1) can be distinguished from each other with the devision along the falx cerebri (cf. sec. 1.3.1.1) and a distinct oscillatory behavior of the gray value for each hemisphere clearly becoming visible. Especially at later τ-values some sulci (primarily in the posterior region) that can be seen in the magnitude image become visible in the phase images as well.

In fig. 3.36 the phase images for $\tau = 60\,\text{ms}$ for all volunteers are displayed. Two volunteers (**id01** and **id08**) were measured twice on different days. The gray scale in each image is adjusted to the maximum phase value measured over all τ-values for the respective volunteer, so the windowing varies. While certain features - like the falx cerebri and the distinction between the two hemispheres through different oscillatory behavior - are visible in almost all images, there are also distinct differences. The image for volunteer **id04** (e) for example shows no clear signature of the falx cerebri, but some sulci (especially in the anterior region) are clearly visible, while for volunteer **id02** the falx cerebri is nearly the only feature in an otherwise almost homogeneous phase image. The two images each for volunteers **id01** and **id08** show also different characteristics, with the phase images of **id01b** (b) and **id08a** (i) for example depicting more small

scale features. This leads to the conclusion that phase images at a specific τ-value seem not to be directly comparable, possibly due to differences in the actual anatomy (which means that size and shape and thus the boundary conditions of the brain tissue vary) and possibly also due to differences in the excitation (due to different weights of the volunteers' heads and different weight distributions on the shell). Analyzing the data further, it is investigated how far the measurements of human brains can be compared to each other.

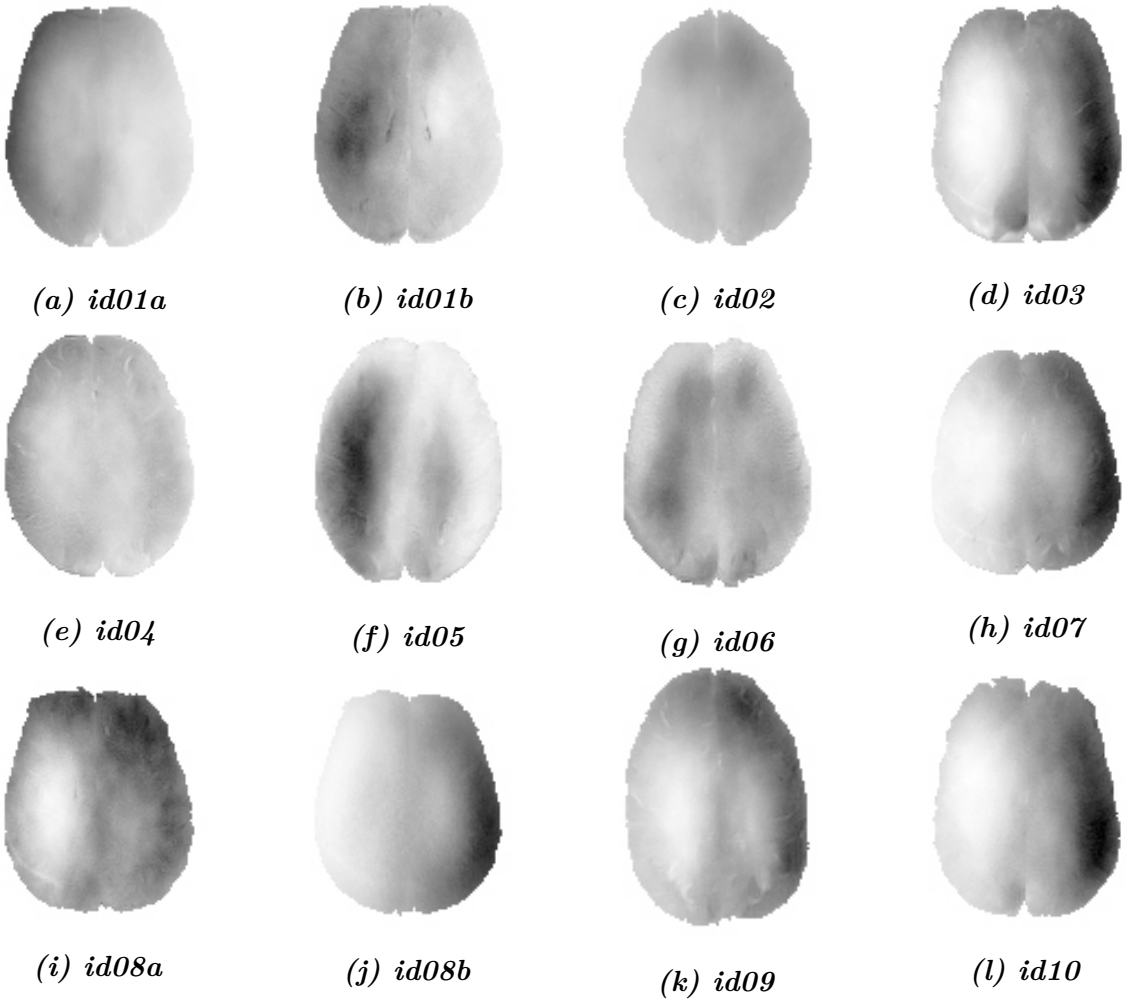

(a) id01a ***(b) id01b*** ***(c) id02*** ***(d) id03***

(e) id04 ***(f) id05*** ***(g) id06*** ***(h) id07***

(i) id08a ***(j) id08b*** ***(k) id09*** ***(l) id10***

Figure 3.36: *Phase Images for All Volunteers at* $\tau = 60\,\mathrm{ms}$*:*
While certain features - like the falx cerebri and the distinction between the two hemispheres through a different oscillatory behavior - are visible in almost all images there are also distinct differences. The image for volunteer ***id04*** *(e) for example shows no clear signature of the falx cerebri, but some sulci are clearly visible, while for volunteer* ***id02*** *the falx cerebri is nearly the only feature in an otherwise almost homogeneous phase image. The two images each for volunteers* ***id01*** *and* ***id08*** *show also different characteristics, with the phase images of* ***id01b*** *(b) and* ***id08a*** *(i) for example depicting more small scale features.*

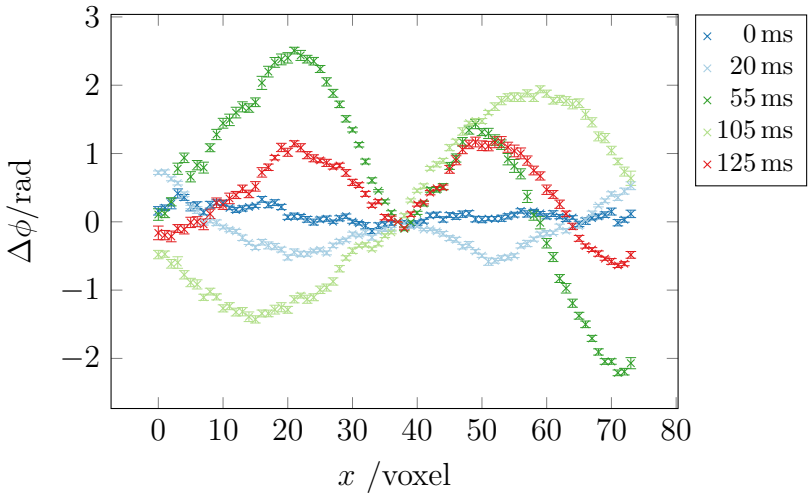

Figure 3.37: *Relative Phase $\Delta\phi$ vs. Voxel for Volunteers:*
*$\Delta\phi$ is plotted on a horizontal cut through the middle of the brain of volunteer **id09** for several τ-values. A separate oscillation for each hemisphere can be observed, which can be in phase for both hemispheres or in phase opposition (as for $\tau = 55\,\text{ms}$). (In parts already published in [62].)*

3.3.2 Relative Phase and Frequency

In a next step, the relative phase $\Delta\phi$ was calculated (cf. eq. 3.1). As a point of reference the phase of the voxel in the middle of the falx cerebri was chosen, because there lies a septum of the dura mater which stabilizes the brain tissue and it is, thus, expected to move less than the rest of the brain (cf. sec. 1.3.1.1). Additionally, the voxel lying in the middle of the falx cerebri is a point easily and reproducible found in each brain.

In fig. 3.37 $\Delta\phi$ is plotted along a horizontal cut through the middle of the brain for volunteer **id09** for five τ-values. For $\tau = 0\,\text{ms}$ the relative phase is almost constant as expected, while for higher τ-values a separate oscillation for each hemisphere can be observed. This separate oscillation can be in phase for both hemispheres (as for $\tau = 20\,\text{ms}$, $55\,\text{ms}$ or $125\,\text{ms}$) or in phase opposition (as for $\tau = 105\,\text{ms}$).

In fig. 3.38a a time series of $\Delta\phi$ for volunteer **id09** is plotted for four voxels, two in each hemisphere, with one being positioned in the center - both vertically and horizontally - of the hemisphere and the other lying in the lower quadrant but not inside a sulcus. The position of the voxels chosen is indicated in a magnitude image (cf. fig. 3.38b) together with the voxel inside the falx cerebri used as a point of reference for calculating $\Delta\phi$.

In fig. 3.38a the relative phase for each voxel shows an oscillatory behavior similar to the one observed in phantoms (cf. fig. 3.5). Comparing respectively the two left and the two right voxels with each other, it can be observed that they display a very similar behavior to their counterpart in the same hemisphere. The behavior in the two hemispheres, however, deviates from each other significantly after $\tau = 50\,\text{ms}$.

Here, volunteer **id09** serves as an example of a typical, well evaluable measurement. In fig. 3.39 two examples of problematic time series are shown. In fig. 3.39a, the time series for volunteer **id02** is with $\tau_{max} = 90\,\text{ms}$ shorter than the normal measurements and exhibits only one distinct maximum after the transient part ($\tau > 40\,\text{ms}$). Another

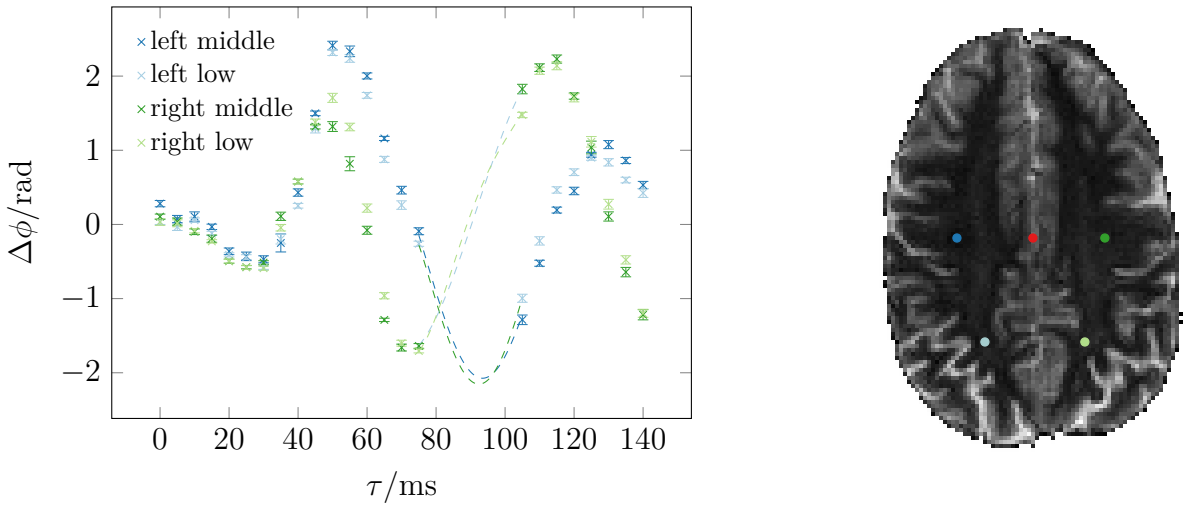

(a) *Time series* ***(b)*** *Overview of voxel used*

Figure 3.38: *Time Series of the Relative Phase for Volunteer* ***id09****:*
For four selected voxel the relative phase $\Delta\phi$ is plotted against τ (a). The positions of the four voxel and the voxel in the falx cerebri used as the reference voxel for calculating $\Delta\phi$ are marked in a magnitude image (b).
For each voxel $\Delta\phi$ shows an oscillatory behavior similar to the one observed in phantoms (cf. fig. 3.4). Comparing respectively the two left and the two right voxels with each other, it can be observed that they display a very similar behavior to their counterpart in the same hemisphere. The behavior in the two hemispheres, however, deviates from each other significantly after $\tau = 50\,\mathrm{ms}$.
Since no data was collected for $75\,\mathrm{ms} \leq \tau \leq 105\,\mathrm{ms}$ the corresponding spline is plotted in fig. a for these τ-values to guide the eye. (Already published in [62].)

minimum can be estimated (however, with some uncertainty) to lie at $\tau \approx 70\,\mathrm{ms}$. On a side note it can be observed that for this measurement, all four voxel in both hemisphere are very much in phase. As a second example of a problematic time series, in fig. 3.39b, the time series for volunteer **id08a** is displayed. Here, it can be observed that the dynamic for the right hemisphere is much lower than for the left one and no real oscillation can be discerned in it.

In order to compare the measurements of the different volunteers more quantitatively with each other, the frequency of the oscillation in each hemisphere is calculated from the time series. Corresponding to the approach described in sec. 3.1.1 a weighted spline was used to interpolate the data and from the spline's extrema the frequency of the oscillation was estimated. In fig. 3.38a the corresponding spline is plotted as an example for the missing data points $75\,\mathrm{ms} \leq \tau_{missing} \leq 105\,\mathrm{ms}$.

From the spline interpolating the data points in the center of each hemisphere a frequency for each hemisphere was calculated for each volunteer. The results are depicted in fig. 3.40. For two volunteers (**id07** and **id08a**) the oscillation data in the right hemisphere was too distorted to reconstruct a frequency, hence, only one data point is shown for each (cf. fig. 3.39b for the time series of volunteer **id08a**).

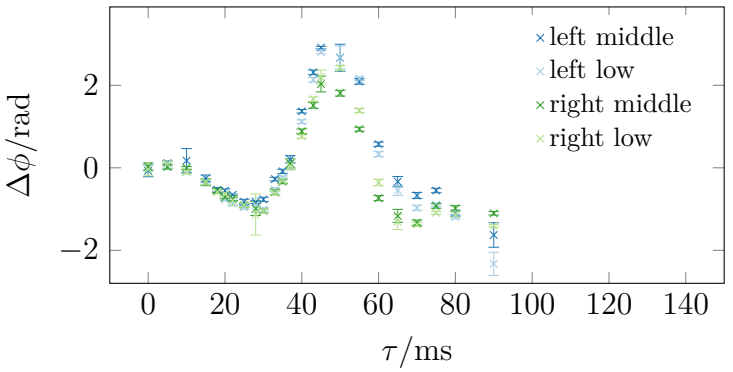

(a) id02

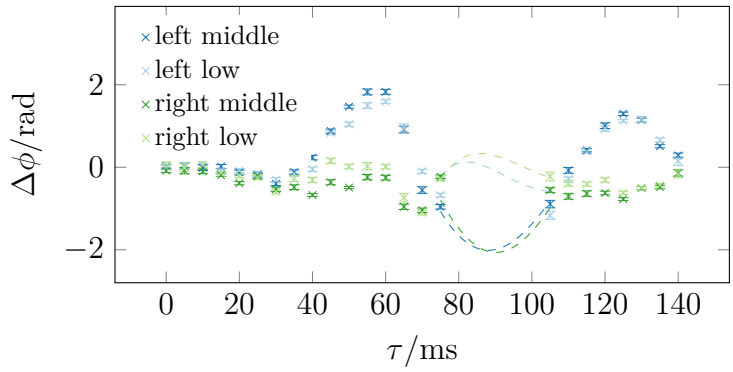

(b) id08a

Figure 3.39: *Examples of Disturbed Phase Oscillations:*
(a) shows the data for volunteer ***id02****. Here, a shorter time series as for the other volunteers was acquired with only one distinct extrema at* $\tau \approx 50\,\text{ms}$ *after the initial dip. A second, much less distinct extrema can be approximated at* $\tau \approx 70\,\text{ms}$*. (b) shows the data for volunteer* ***id08a****. While the data for both left voxels are comparable to the data presented in 3.38a, both right voxels show much less dynamic and extracting a frequency was not justifiable.*

The error for the frequency was propagated from the errors in $\Delta\phi$ as in sec. 3.1.1 using a parametric bootstrap procedure with 1500 bootstrap samples. All frequencies measured aside form the ones for volunteer **id02** lie between 10 Hz and 18 Hz. The data for volunteer **id02** appears to be an outlier which might be attributed to the fact, that the time series for the corresponding measurement was shorter than for the other measurements and with a maximal $\tau_{max} = 90\,\text{ms}$ too short to extract a reliable frequency (cf. fig. 3.39a).

The differences between the hemispheres in each volunteer are probably not a sign of differences in the mechanical properties between the hemispheres but the result of an uneven excitation. This is discussed later in sec. 3.3.4 (cf. fig. 3.42).

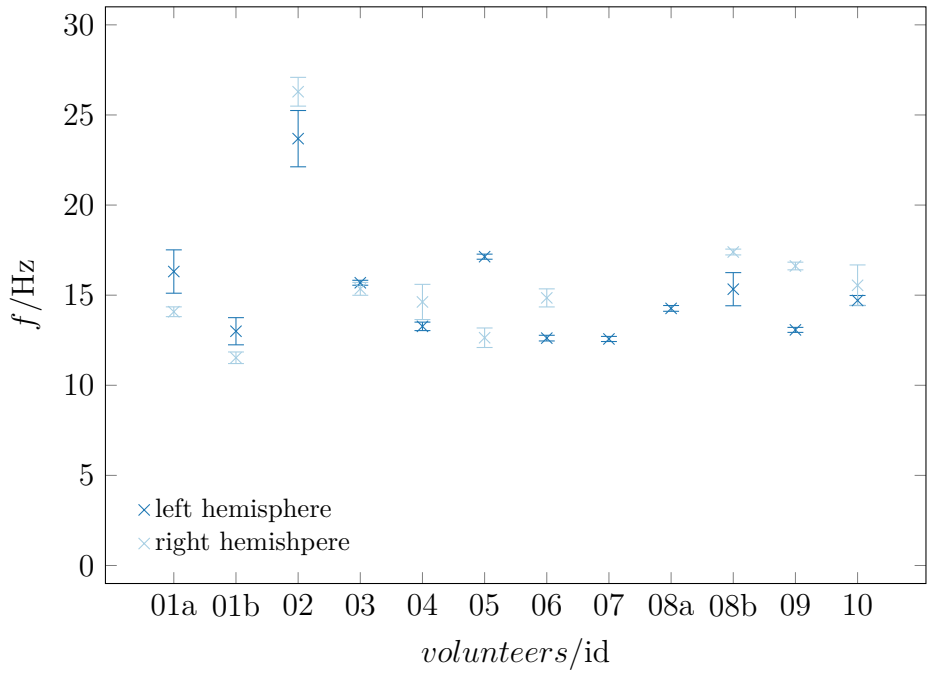

Figure 3.40: *Comparison of Frequency for Volunteers:*
For each volunteer - except for volunteer ***id07*** *and* ***id08a****, where the oscillation data in the right hemisphere was too distorted to evaluate - a frequency for each hemisphere is plotted. All frequencies measured aside from the ones for volunteer* ***id02*** *lie between* 10 Hz *and* 18 Hz*. The data for volunteer* ***id02*** *appears to be an outlier which might be attributed to the fact, that the time series for the corresponding measurement was shorter than for the other measurements.*

3.3.3 Strain Images

Similar to what has been done for the phantoms with cubic and fluid filled inclusions in sec. 3.2.2 and 3.2.3 the absolute phase strain $|\epsilon_\phi|$ (cf. eq. 3.5) was calculated for all volunteers. For the data presented here, a Gaussian filter with $\sigma = 0.7$ was used to smooth the phase images before calculating $|\epsilon_\phi|$. The value for σ was chosen differently from the one used for phantoms because of the higher noise in the volunteer measurements.

In fig. 3.41 a phase strain image for every volunteer is displayed. The τ-value chosen to display in each case was the τ-value of the first maximum of each time series of $\Delta\phi$ (cf. fig. 3.38). In order to compare the structures visible in the phase strain images to anatomical structures, the phase strain images are superimposed to a high resolution magnitude image. Here, dark blue indicates low $|\epsilon_\phi|$-values, while red indicates high ones.

Some of the high strain features in these images correspond to anatomical features like sulci while others show no obvious correlation. In most images ((a), (d), (g), (h), (i) or (k)) there is considerable higher phase strain in the anterior brain region than in the posterior one. This might be an effect of the boundary condition of the surrounding

skull. The image for volunteer **id02** (c) shows on average a higher phase strain than the other volunteers, while volunteer **id01** shows a comparably low overall phase strain in their second measurement (b) compared to the first one (a). The images for the two measurements of volunteer **id08** show also differences.

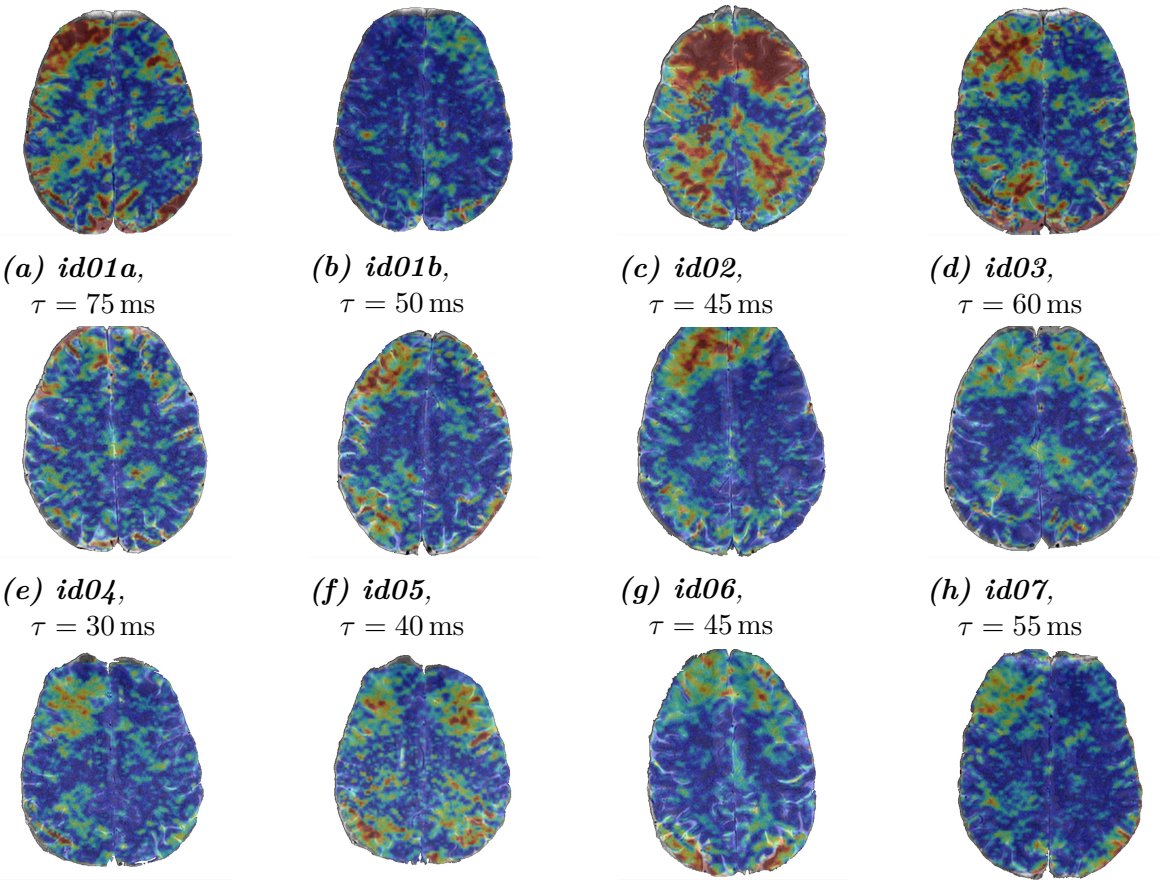

(a) id01a, $\tau = 75\,\text{ms}$ ***(b) id01b***, $\tau = 50\,\text{ms}$ ***(c) id02***, $\tau = 45\,\text{ms}$ ***(d) id03***, $\tau = 60\,\text{ms}$

(e) id04, $\tau = 30\,\text{ms}$ ***(f) id05***, $\tau = 40\,\text{ms}$ ***(g) id06***, $\tau = 45\,\text{ms}$ ***(h) id07***, $\tau = 55\,\text{ms}$

(i) id08a, $\tau = 60\,\text{ms}$ ***(j) id08b***, $\tau = 75\,\text{ms}$ ***(k) id09***, $\tau = 50\,\text{ms}$ ***(l) id10***, $\tau = 60\,\text{ms}$

Figure 3.41: *Absolute Phase Strain Images for All Volunteers at First Maximum: The phase strain images are superimposed to high resolution magnitude images. Dark blue indicates low $|\epsilon_\phi|$-values, wile red indicates high values. Some of the high strain features correspond to anatomical features like sulci while other show no obvious correlation. In most images ((a), (d), (g), (h), (i) or (k)) there is considerable higher phase strain in the anterior brain region than in the posterior one. This might be an effect of the boundary condition of the surrounding skull.*

3.3.4 Excitation Profile

At this point of research the differences in the measurements cannot be sufficiently explained but it is probably an effect of differences in the excitation. In fig. 3.42 the signal of the optical positioning system (cf. sec. 2.1.2.2) is displayed for both **id08a** (a) and **id08b** (b). The signals displayed are for different τ-values, however, since the excitation is quite stable over time, this is not problematic. It can be observed that for the first measurement (a) both the left and the right side reach their first minimum at nearly the same time as the superior position (at around $t = 0\,\mathrm{ms}$). The superior signal shows then one small additional oscillation before leveling out while the left and right signals show at least two additional oscillations. This can be interpreted as the three points of the shell landing at the same time. The part at the neck (measuring points left and right) bounces back while the superior part of the shell comes to rest quite easily. In the case of the second measurement (b), however, the superior signal has its first minimum 10 ms after both the other signals and has at least one additional prominent maximum while the left and right signal show - in contrast to the first measurement - only one additional maximum before leveling out. Here, the superior part of the shell comes to rest much later than the inferior part.

The corresponding time series are shown in fig. 3.43. It can be seen that, though both are from the same volunteer, they differ significantly from each other. In fig. 3.43a there is no distinct oscillation in the right hemisphere.

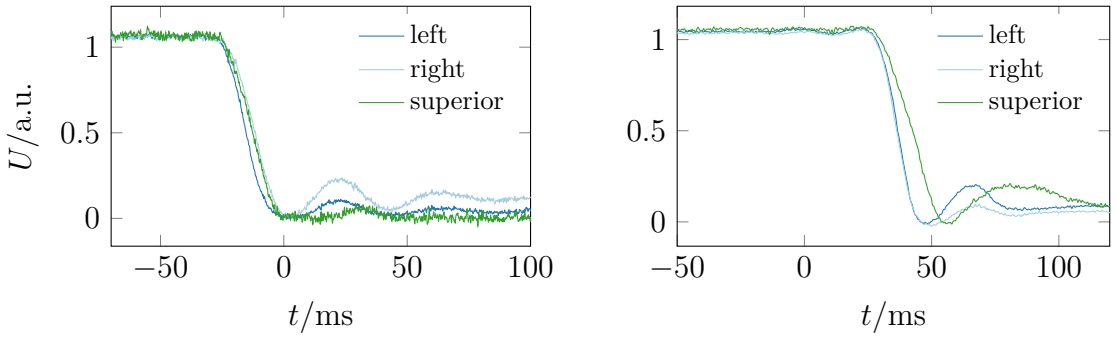

(a) id08a ***(b) id08b***

Figure 3.42: *Comparison of Excitation Profiles:*
Data from the optical positioning system at the three points of the shell are shown for the two measurements of volunteer ***id08****. It can be observed that at the first measurement (a) both the left and the right side reach their first minimum at nearly the same time as the superior position (at around $t = 0\,\mathrm{ms}$). The superior signal shows then one small additional oscillation before leveling out while the left and right signals show at least two additional oscillations. In the case of the second measurement (b), however, the superior signal has its first minimum 10 ms after both the other signals and has at least one additional prominent maximum while the left and right signal show - in contrast to the first measurement - only one additional maximum before leveling out.*

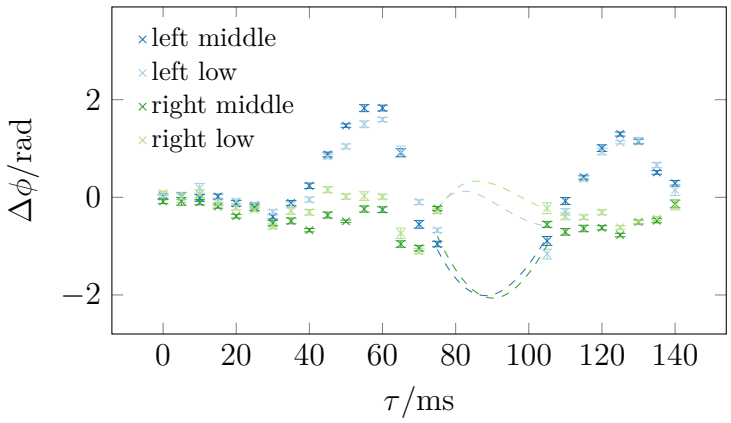

(a) id08a

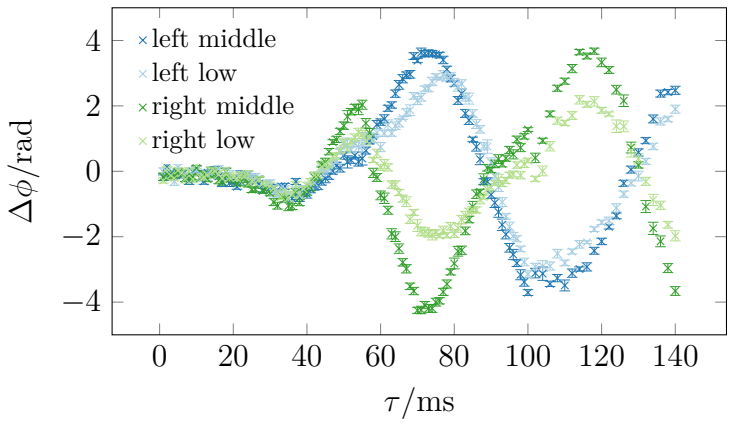

(b) id08b

Figure 3.43: *Comparison of Time Series:*
The time series correspond to the two excitation profiles shown in fig. 3.42 for volunteer ***id08****. It is clearly visible that the measurements differ from each other. This is probably a result of the different excitation.*

3.3.5 Second Gradient Setting

Using the second gradient set ($\delta = 10.36\,\text{ms}$, $\delta\Delta = 40\,\text{ms}$, $G = 17.3\,\text{mT}\,\text{m}^{-1}$) similar measurements to the first gradient setting were taken for volunteers **id03** to **id10** with volunteer **id08** only measured once. Due to time constrains less different τ-values have been sampled in the measurements.

In the single phase images no significant difference could be found compared to the ones acquired with the first gradient set. As before a frequency for each hemisphere was also determined for each volunteer, except for volunteers **id04** and **id07**, where the oscillation data in the right hemisphere was too distorted to evaluate. The results are plotted in fig. 3.44 and can be compared to the ones in fig. 3.40. Here, the frequencies for all volunteers except for volunteer **id05** lie in a similar range between 10 Hz and

17 Hz. Volunteer **id05** showed an average frequency for the first gradient set and the deviation for this measurement cannot be readily explained, except for the fact that for this gradient set there were generally fewer data points available, increasing the risk of undersampling of the oscillation and thus misconstruction of the frequency. Phase strain images (cf. sec. 3.3.3) were calculated for the second gradient set as

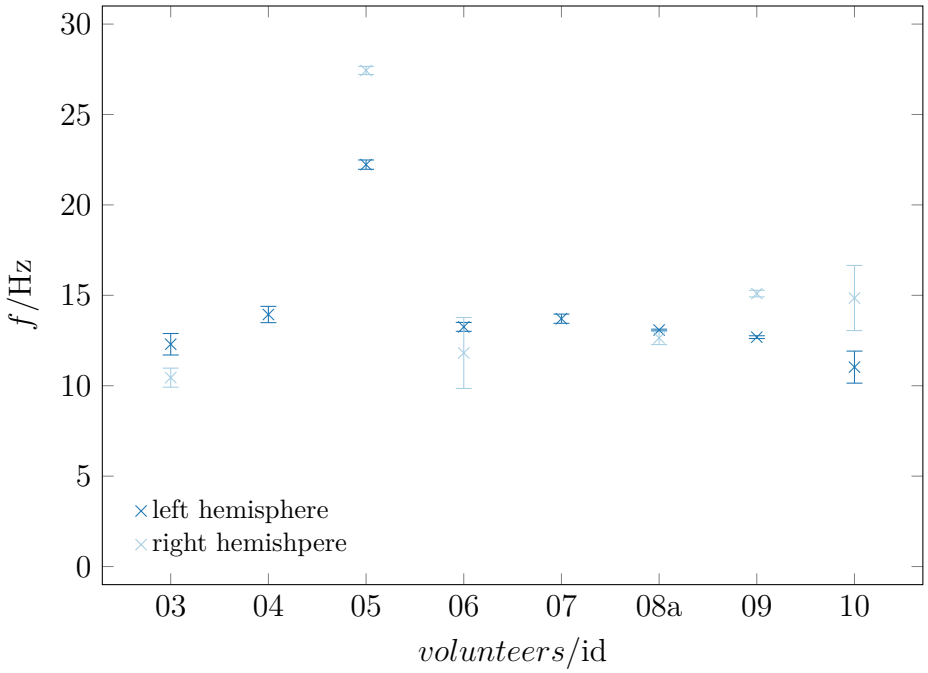

Figure 3.44: *Comparison of Frequency for Volunteers for Second Gradient Set: For each volunteers **id03** to **id10** - except for volunteer **id04** and **id07**, where the oscillation data in the right hemisphere was too distorted to evaluate - a frequency for each hemisphere is plotted. All frequencies measured aside from the ones for volunteer **id05** lie between* 10 Hz *and* 17 Hz *which is comparable to the results from the first gradient set (cf. fig. 3.40).*

well and the ones for the τ-value of the first maximum of each time series of $\Delta\phi$ are displayed in fig. 3.45 (again superimposed to a high resolution magnitude image). They show similar characteristics as the ones displayed in fig. 3.41 as some structures (sulci) show a higher strain (depicted from blue to red) as the surrounding tissue. Overall, it can be seen that the longer, but lower gradients have no significant influence on the results presented here. It can be assumed, however, that time sensitive information is increasingly blurred through the longer gradients.

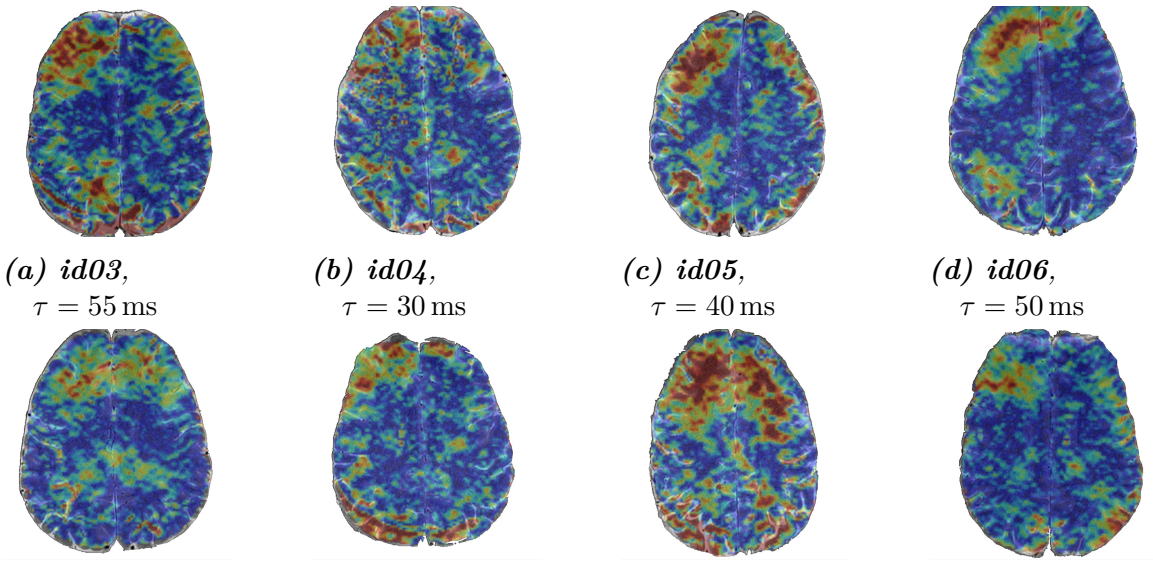

(a) id03, $\tau = 55\,\text{ms}$ ***(b) id04***, $\tau = 30\,\text{ms}$ ***(c) id05***, $\tau = 40\,\text{ms}$ ***(d) id06***, $\tau = 50\,\text{ms}$

(e) id07, $\tau = 60\,\text{ms}$ ***(f) id08a***, $\tau = 50\,\text{ms}$ ***(g) id09***, $\tau = 60\,\text{ms}$ ***(h) id10***, $\tau = 65\,\text{ms}$

Figure 3.45: *Absolute Phase Strain Images for All Volunteers at First Maximum for Second Gradient Set:*
Compared to the phase strain images for the first gradient setting displayed in fig. 3.41 the longer, but lower gradients seem to have no significant effect on the phase strain. Here too, some sulci show a higher phase strain than the surrounding tissue.

4 Discussion and Conclusion

In this chapter the previously presented results are discussed and put into a more general context.

The aim of this thesis has been to conduct first systematic MRR measurements, test the lifting device introduced in [65] outside laboratory conditions and to develop methods of analysis to compare measurements without the need to calculate the physical trajectory from the phase.

The phantom measurements showed that using phase and phase strain images as well as phase cuts, substructures (different layers, cubes or fluid filled inclusions) can be spatially resolved in inhomogeneous phantoms. The introduction of the relative phase allowed to compare different measurements and analyze the temporal behavior of the phantoms. The frequency extracted from the observed oscillation in the relative phase showed a dependency on the size and stiffness of the phantoms that is consistent with qualitative theoretical considerations and may, thus, serve as an indicator for the bulk properties of the material under investigation.

Similarly for *in vivo* measurements on human volunteers, the frequency could be extracted for each hemisphere of the brain. The results for the ten volunteers measured showed mostly comparable values with an outlier for one volunteer, indicating that the frequency can be used as an indicator for the bulk properties of the brain tissue as well. Local structures like sulci on the other hand could - to some extent - be resolved both on phase and phase strain images.

Even though there is room to improve the reproducibility of both the phantom production and the form of the excitation over different measurements, the promising results from the phantoms and the volunteers indicate that MRR can be an interesting tool to investigate brain tissue noninvasively and suggest that certain pathologies should be detectable using this method. A promising first study on meningiomas (a kind of brain tumor arising from the meninges) using MRR has been conducted by Theilenberg which showed that the tumors have a distinct and spatially correct signature in the phase strain images as well as that tumors with different consistency vary in their phase strain distribution [62, 118].

In the following sections the results are discussed according to the analysis approach applied.

4.1 Phase Images

Phase images are the basic data format exported from the MR scanner and can give an easy access to the acquired information without the need of much post-processing.

Their value in MRR is discussed below.

As assumed, in response to the shock excitation the phase images for the homogeneous phantoms in figure 3.1 (section 3.1.1) showed an oscillatory behavior with the center experiencing a higher phase shift than the border regions connected to the container. This can be translated into the interpretation that the center of the phantom moves more in relation to the border regions. This is to be expected since the border regions of the phantom are hindered in their movement by the friction due to their connection to the container wall.

The measurements of the three two-layered phantoms ϑ_1, ϑ_2 and ϑ_3 in section 3.2.1 showed that it is also possible to distinguish between layers of different stiffness inside a phantom from the temporal behavior of the phase depicted in the phase images. In the images in the figures 3.20, 3.23 and 3.26 the differences between the two layers were visible for all phantoms. Even the smallest differences in stiffness of $\Delta G = 0.77\,\mathrm{kPa}$ in phantom ϑ_2 could be resolved.

The cubic inclusions in the η phantom presented in figure 3.29 (section 3.2.2) were visible in some phase images but their signature was not very distinct. On the other hand, the fluid filled inclusion in the κ phantom described in section 3.2.3 was easily visible in the phase image in figure 3.33b, even though the temporal behavior was not measured but only one point in time.

For the human volunteers in section 3.3.1, the observations made for the phantoms could be transferred. The different images for a single volunteer in figure 3.35 showed in both hemispheres, which are separated by the falx cerebri (cf. sec. 1.3.1.1), an individual, global oscillation as did the homogeneous phantoms (cf. fig. 3.1). Additionally, various smaller structures - which could be identified as sulci (cf. sec. 1.3.1) - can be observed at different τ-values, which is a characteristic that could also be observed in the η phantom with the cubic inclusions (cf. fig. 3.29). These two observations hold true for all volunteers (cf. fig. 3.36), though the phase images on their own are not comparable directly - neither for the same volunteers measured twice (cf. fig. 3.36a vs. 3.36b and 3.36i vs. 3.36j) nor among the different volunteers.

4.1.1 Conclusion

Aside from phase unwrapping, a baseline correction and averaging no further post-processing was used for the phase images (cf. sec. 2.3). In some images, phase unwrapping artifacts (motion artifacts prominent e.g. in the figures 3.20, 3.23, 3.26, or 3.33b) disturbed the image and could in the worse case corrupt it beyond use. That is one reason to use low motion encoding gradients, so that not too many phase jumps (each with a risk of leaving an unwrapping artifact) manifest in the image. Nonetheless, valuable information could be extracted readily from these images - both for phantom and volunteer measurements. A time series of images with different τ-values was helpful, since different features manifest at different τ-values. Phase images alone, however, do not suffice to fully analyze the measurements.

4.2 Phase Strain Images

In order to reduce the global oscillation visible in the phase images and to concentrate more on local effects, absolute phase strain images were used.

For the cubic inclusions in the η phantom it could be shown that, though the cubes were also only visible for certain τ-values in the phase strain images, the borders were well defined and they matched the positions of the cubes extracted form the magnitude image (cf. fig. 3.32).

The fluid filled inclusion in the κ phantom was also very well visible in the phase strain image in figure 3.33c. This image is, however, also an example that artifacts are emphasized when using the phase strain.

The images for the human volunteers in the figures 3.41 and 3.45 for the two different gradient settings were also useful to examine localized structures. For both gradient settings smaller structures were visible, some of which can be identified as sulci. Other structures have no obvious anatomical source, but the heterogeneity of these images should be further investigated. It may originate from the influence of the complex boundary conditions in the brain. But it would also be interesting whether other anatomical features beside sulci (differences between gray and white matter, nuclei, different brain regions (cf. sec. 1.3.1) or pathological features) can be distinguished on phase strain images. The slices used here were, however, not chosen to include many additional features.

4.2.1 Conclusion

Images depicting the absolute phase strain provide an interesting approach for investigating small scale structures. Using these, localizing features is easy and precise. The dimensions of the smallest structures visible here were in the order of $200\,\mathrm{mm}^2$ in the slice (both the cubic inclusions and the sulci). The difference in shear modulus for the cubic inclusion was $\Delta G = 1.86\,\mathrm{kPa}$. It will depend on the motion encoding gradient setting as well as on the excitation profile up to which dimensions and ΔG structures can be resolved.

Further research should also concern itself with the question of how to compress the temporal and the spatial information of a time series of phase strain images. In order to compare the volunteers in this thesis, the image for the τ-value at the first maximum of $\Delta\phi$ was chosen. However, maybe other methods are more useful, for example an integrated absolute phase strain.

4.3 Relative Phase Cuts

In order to better observe the behavior of the phase, $\Delta\phi$ was plotted along a horizontal line through the phantoms and the brains.

For the homogeneous phantoms it could be shown that through phase cuts (ϕ vs. voxel) the oscillation could be better observed (cf. fig. 3.2). The phase offset (probably

due to the macroscopic movement of the whole container) could be successfully reduced by calculating the relative phase $\Delta\phi$. This allowed to better compare the measurements for different τ-values.

For both the phantoms and the volunteers the statistical errors on the phase resulting from averaging over the ten repeated measurements were small, proving that the induced movement and its measurement in the phase images is reproducible during one measuring session in the MRI. It thus confirms the laboratory measurement of the reproducibility of the induced movement using a lead weight presented by Ulucay [65]. Other statistical fluctuations are well under controll as well.

For the two layered ϑ phantoms, it was expected, that the two layers should leave a signature in the relative phase cuts. The distinction between the layers was, however, sometimes ambiguous. For the ϑ_1 phantom (cf. fig. 3.21) a not well explainable behavior could be observed in both layers and the border could not be easily inferred. For ϑ_2 and ϑ_3 (cf. fig. 3.24 and 3.27) the expected behavior of an oscillation in every half could be observed and it was possible to infer the borders.

For the η phantom, figure 3.30 depicted the cuts through the middle of the two hydrogel inclusions. They showed that these cubic inclusions left a quite distinct deviation from the global oscillation for some τ-values. The borders of the inclusion, however, could not always be inferred from these deviations accurately. The deviations themselves showed also a kind of localized oscillation. It might be possible in the future - when the influence of size and boundary conditions on the oscillation are better understood - to extract quantitative information about the cube's material properties from this.

The cuts along different horizontal lines for the η phantom shown in fig. 3.31 showed that the cubes induced an effect even above their position. This observation can be explained when considering that the cubes are made of a softer hydrogel than the surrounding material. This means that the cube suffers a greater displacement that the material below it and, thus, allows for a greater displacement of the overlying material as well. The precise determination of the position of the cubes from the phase cuts seems to be error prone.

The relative phase cuts through the fluid filled inclusion in the κ phantom in fig. 3.34 showed on the other hand an almost constant phase inside the inclusion, since the water inside is incompressible and has no room to flow. Here, contrary to the measurements on the cubic inclusions, the borders can be determined accurately and no clear influence above or below the inclusion can be observed.

The concept of the relative phase cuts worked for the human volunteers as well, here with a reference point in the falx cerebri (cf. fig. 3.37). The errors on $\Delta\phi$ are in the same order of magnitude as for the phantoms, which indicates that for compliant volunteers - they were asked beforehand to try and relax their shoulder and neck muscles as not to influence the induced movement of the shell - the measuring technique is reproducible during one measuring session.

As expected from the phase images and the phantom measurements, the distinct oscillation in each hemisphere was easily visible. For some τ-values the hemispheres were in phase, for others they are in phase opposition.

4.3.1 Conclusion

Plotting $\Delta\phi$ along a horizontal cut through a probe provides a deeper insight into the spatial distribution of the relative phase. The oscillation and the different behavior of differently structured substructures becomes better observable.

4.4 Time Series

Using $\Delta\phi$, the temporal behavior of a single voxel can also be observed. As expected, each voxel responds with an oscillatory behavior to the excitation.

When looking more closely, though, for both phantoms (cf. fig. 3.5) and volunteers (cf. fig. 3.38) the time series showed a transient part before the oscillation starts. This can be an effect of the two-stage excitation (cf. sec. 2.1.1): The fall took - in the case of the homogeneous phantom in fig. 3.5 - about 30 ms which coincided with the first minimum of the time series. After that, the system is exposed to the second excitation due to the landing and the response of the system can develop from thereon undisturbed. As it is the aim to characterize the oscillation through a frequency (cf. fig. 3.6), it would be helpful to automatically determine the length of the transient. Up to now, however, the length has to be determined manually for every time series. On the one hand, because the fall time is not constant for all measurements and on the other hand because determining $\tau = 0\,\text{ms}$ is up to now also done manually. Björn Schemmann has worked in the course of his diploma thesis on the automating of this process but it has not yet been implemented.

For the two layered ϑ phantoms the examination of the time series indicated that they might be an interesting tool on their own, since a correlation between amplitude and stiffness could be hinted at (cf. fig. 3.22, 3.25 and 3.28). In order to confirm this correlation, however, more experience and a clearer understanding of the influence of the form of the excitation are necessary.

Before concentrating on the frequency extracted from the time series, the two aspects of the correlation between phase and spatial oscillation (cf. sec. 4.4.1) and of disturbed time series (cf. sec. 4.4.2) need to be discussed.

4.4.1 Phase and Spatial Oscillation

It has, however, to be kept in mind that the oscillations described above are oscillations of the phase and not spatial oscillations. Both are connected via equation 1.12, which describes the relation between the phase and the spatial trajectory dependent on the magnetic field gradients (cf. sec. 1.1.2.8). In section 3.1.1.2 the relation between spatial and phase oscillation was investigated with the means of two examples using the gradient setting applied in the phantom measurements and in the first part of the volunteer measurements.

Considering the form of equation 1.12 is similar to a convolution, it can be deduced that the frequency spectrum of the phase oscillation is a multiplication of both the frequency spectrum of the spatial oscillation and of the magnetic field gradients.

Thanks to a broad frequency spectrum of the trapezoidal gradients used, it can be expected that the phase and the spatial oscillation do not differ significantly from each other. This is supported by the examples in figures 3.8 and 3.9.

As we have explained in [62], however, it has to be kept in mind that the gradient frequency spectrum has zeros at $1/\delta$ and $1/(\delta + \delta\Delta)$ and corresponding higher harmonics. This means that certain spatial frequencies will be suppressed in the phase representation. For the gradient settings used for the phantoms this concerns $f_1^* = 1/\delta = 1/5\,\mathrm{ms} = 200\,\mathrm{Hz}$ and $f_2^* = 1/(\delta + \delta\Delta) = 1/45\,\mathrm{ms} = 22\,\mathrm{Hz}$. While f_2^* indeed lies in a relevant frequency range, it should be considered that the phantom material is lossy and that a total signal loss due to the gaps in the gradient spectrum is not expected. Nonetheless, it would be interesting to calculate the true trajectory from the phase and examine the spatial oscillation directly. This would allow also for the examination of the amplitude of the oscillation since the decay of the amplitude should be linked to the viscous parameter of the material. More detailed work concerning the relation between spatial trajectory and phase has been done by Theilenberg in the course of his dissertation [118].

4.4.2 Disturbed Time Series

In the course of this thesis, several disturbed time series were observed, which did impede the frequency reconstructions (cf. fig. 3.7 and 3.39). Two explanations for the deviations are conceivable.

On the one hand, it should be considered that through the excitation oscillations with a multitude of frequencies are excited. Higher frequencies die out quicker than lower ones and up to now it is assumed in the data analysis that only the lowest frequency remains. It is, however, also possible that in the time series a superposition of higher frequencies is measured. This possibility could be addressed by applying a Fourier analysis to the spatial oscillation (which would have to be calculated beforehand).

On the other hand, it is probable that the form of the excitation itself can cause a disturbed measurement since disturbances could also be observed in one of the repeated measurements in volunteers (cf. sec. 3.3.4). However, up to now it cannot be predicted which excitation profile would lead to optimal results and which might cause a disturbed measurement.

4.4.3 Conclusion

Using the relative phase $\Delta\phi$ the temporal behavior of a single voxel could be examined and the effect of the two-staged excitation be observed. These time series might proof beneficial in the future to compare materials when examining the amplitude of the oscillation. For that, however, it might be necessary to calculate the spatial trajectory and understand the dependency of the time series on the precise form of the excitation better. To achieve that, the excitation profile should be measured in physical and quantitative units (like acceleration) in the future. Additionally, a higher statistic of measurements is needed to draw more sound conclusions.

4.5 Frequency

The frequency extracted from the time series $\Delta\phi(\tau)$ was used to quantify and compare measurements.

For the phantom measurements it could be shown that the value of the frequency is relatively stable over the volume of the phantom apart from the border regions near the container, which is expected since there the boundary conditions predominate the behavior of the hydrogel (cf. sec. 3.1.1.3). For the human volunteers it could also be shown that different voxels inside one hemisphere show a remarkably similar behavior (cf. fig. 3.38 and 3.39). This is promising, as it supports the assumption that the frequency is a measure for the bulk properties of the system investigated and that measurements can be compared even if the frequency was extracted from different voxels.

Since the phase was sampled only for discrete τ-values it was necessary to interpolate the data, which worked reasonably well for both the phantoms and the human volunteers with a sparser sampling.

In the following sections the results based on the frequency are discussed separately for the measurements on phantoms (cf. sec. 4.5.1) and for the ones on the human volunteers (cf. sec. 4.5.2).

4.5.1 Frequency in Phantoms

In sec. 3.1.2 it was shown from the comparison of the measurements of phantoms with different container sizes and stiffness of the hydrogels that the frequency indeed works as an indicator of these two properties as can be seen in figures 3.15 and 3.17. In these two figures the mean frequency f over the realizations of the different kind of phantoms behaved mostly as expected: f decreases for higher diameter and increases with stiffness. An exception is the data for $d = 85\,\mathrm{mm}$. This were, however, also the only phantom where the diameter exceeds the hight of the phantom. Whether this is a crucial characteristic has to be determined in further studies. The curve fits shown in figures 3.16 and 3.18 were a test and only illustrated that the data does not contradict the qualitative theoretical predictions stated in equations 3.3 and 3.4. However, they showed a promising tendency. Yet, more data points with a higher statistic would be needed to evaluate the conclusion.

In figures 3.13 and 3.14 it could be observed that for a single type of phantom the frequencies can vary up to $\Delta f = 4.8 \pm 0.8\,\mathrm{Hz}$ (α_5 phantoms). This has to be kept in mind for further frequency comparisons. A factor for the frequency spread could be a variance in the hydrogel properties. Even though all phantoms were produced using the same cooking protocol (cf. sec. 2.2.2.1) it could not be ruled out that there were deviations in the mechanical properties of the hydrogel, since for example the amount of evaporated water (which influences the agar concentration) could not be measured for every phantom and was extrapolated from a series of measurements. For the future, it would be desirable to have an independent access to the mechanical properties of the hydrogel to verify the properties or rather their spread. Another factor for the

frequency spread might be the reproducibility of the excitation which will be discussed in section 4.6.1.

In figure 3.19 the influence of different boundary conditions was investigated with means of different spongy layers around the hydrogel (λ, μ and ν phantoms). It could be seen that all the different interlayer indeed change the frequencies. From these results - even though these are preliminary tests - it can be suggested that the complex coupling between brain tissue and skull (cf. sec. 1.3.1.1) might have to be taken into account when comparing *in vivo* measurements to phantom measurements. A more complex and soft coupling might, however, also offer the possibility to change the sensitivity of the measurement technique since the two shear moduli investigated here were indistinguishable in their frequency for the configuration without an interlayer (δ_5 and δ_6 phantoms), while for the interlayer configurations μ and ν the frequencies differ significantly from each other.

For the two layered phantoms frequencies were extracted for every layer from the time series shown in the figures 3.22, 3.25 and 3.28, except for the $G_2 = 4.5\,\mathrm{kPa}$ layer in the ϑ_2 phantom. For the ϑ_1 phantom the frequencies for the two sides lay inside each other's margins of error ($\Delta f_{\vartheta_1} = 0.3 \pm 0.9\,\mathrm{Hz}$), while for the ϑ_3 phantom the slight difference between the layers was $\Delta f_{\vartheta_3} = 0.6 \pm 0.4\,\mathrm{Hz}$. Here, the frequency provided no useful information. In further studies it should, however, be investigated whether this holds true for these kind of phantoms in general or if further considerations have to be included into the analysis. For example, it should be investigated to what extend the two layers influence each other.

4.5.2 Frequency in Human Volunteers

The frequencies calculated for the human volunteers for the two gradient settings used are plotted in figures 3.40 and 3.44. They lay mostly in a range between 10 to 18 Hz for the first gradient setting (with one outlier for **id02**, probably due to a too small τ_{max}-value) and 10 to 17 Hz for the second one (with one outlier for **id05**, maybe due to a too scarce sampling). No significant effect of the choice of the gradients can be observed. The frequency range is very similar for both and it is likely that the differences for each volunteer can be attributed to the different sampling (cf. tables 2.1 and 2.2) or different excitations. Further studies should, however, investigate these assumptions. For the single volunteers, the frequencies in each hemisphere differed from each other by maximal 5 Hz (for both gradient setting volunteer **id05** showed the highest difference).

Regarding the deviations between different volunteers, several factors can be considered aside from differences in the excitation. On the one hand, it could be learned from the phantom measurements that the size of the brain should influence the frequency. However, the brain dimensions extracted from the measured slices do not show any deviations that correlate with the deviations in the frequency (cf. fig. A.1). It would be interesting in the future how a more precise determination of the size of the whole brain volume would influence this interpretation. Secondly, it is to be expected that brain tissue exhibits a natural variance in its mechanical properties. How great this

influence is on the frequencies could be investigated in the future as well.

4.5.3 Conclusion

The frequency results of the homogeneous phantom measurements showed that the phase frequency can be used as a measure for the bulk properties of the probe. This concept could successfully be transfered to human brains and offered a means to quantify the measurements.

The variances observed can result from different effects. Generally speaking, more measurements should be performed in the future to achieve a better statistic for both phantoms and volunteers and a better estimate for the errors of the measurements which might overall be underestimated. For healthy volunteers it could also be investigated whether the observation of some MRE studies regarding the influence of age and gender [91, 119] can be reproduced.

4.6 Technical Realization

In this final part of he discussion, two aspects that have already been mentioned in the previous sections are discussed in more detail - the technical realization of the excitation and the influence of the resulting excitation profile on the measurements (cf. sec. 4.6.1) as well as the influence of the measuring protocols implemented (cf. sec. 4.6.2).

4.6.1 Influence of the Excitation Profile

The repeated measurements on the two volunteers **id01** and **id08** for the first gradient setting showed deviations between $\Delta f = 1.1 - 3.3\,\mathrm{Hz}$, while also in the phantoms a frequency spread for each phantom configuration can be observed (as discussed in section 4.5.1).

Apart from the factors discussed above, an additional influence for both the phantoms and the volunteers, however, is probably also the excitation profile, which could explain the differences in the repeated measurements. In figure 3.42 the differences in the two excitation profiles used for the two comparative measurements of volunteer **id08** are shown. Even though a quantitative analysis of the height of the fall or the acceleration is not possible from this data, it can be seen that the excitations are not equal. This could also be observed for the phantom measurements.

The idea behind the construction of the lifting device (cf. sec. 2.1.2.1) was that the shell is lifted to a stable upper position well defined by the stoppers through the high pressure. By adjusting the throttle and regulating valves in the low pressure circuit the fall trajectory should be controlled (cf. sec. 2.1.2.3).

A limitation discussed by Björn Schemmann in his diploma thesis is, however, that the pneumatic control elements could not be adjusted independently from each other over a sufficient range for the measurements performed for this thesis. The high

pressure could not be adjusted such that both in measurements with phantoms and with volunteers the shell was always in the same, stable upper position. Thus, the upper position was dependent on the distribution of weight on the shell. The low pressure circuit could not be adjusted sufficiently to accurately reproduce the fall trajectory. The final part of the excitation consists of the bouncing after the landing. This part was also influenced by the weight distribution. Though the phantom containers fitted precisely in the shell, the sandbags used to weigh them down could not be placed fully reproducible, thus changing the weight distribution between different measuring settings. This also applies for the volunteers: the heads fixated using the vacuum cushion could not always be positioned reproducible in the shell.

Unfortunately, in contrast to the conclusion drawn by Ulucay in [65] from laboratory tests it must also be deduced that the shell is not stiff enough or the stabilization through the flat springs (cf. sec. 2.1.2.1) not stable enough to prevent a rotation in the transversal plane. If such a rotation were prevented, in figure 3.42 the positioning curves for the left and for the right would either be identical for all times or not be identical at all during one measurement. Here, however, they show an identical behavior during the initial fall but later a different bouncing behavior. This rotation might be a contributing factor to the variance of the frequency between the two hemispheres.

4.6.2 Measuring Protocols

In the course of this thesis different measuring protocols regarding the temporal sampling ($\Delta\tau$, τ_{max}, $\tau_{missing}$) and the motion encoding gradients were used (cf. tables 2.1, 2.2 and sec. 2.2.2.2).

Regarding the temporal sampling, it should be noted that especially with probes for which a low frequency is expected, τ_{max} should be high enough so that a sufficient number of extrema are present from which to extract the frequency. For most measurements (both phantoms and volunteers) a sampling interval of $\Delta\tau = 2 - 5\,\text{ms}$ seems adequate to reconstruct the frequency precisely enough from $\Delta\phi$. The interval $\Delta\tau = 10\,\text{ms}$ used for the second gradient setting for the volunteers was borderline, so that these frequencies are not as reliable. For most volunteers (especially for the first gradient setting), the $\tau_{missing}$ chosen did not hinder the frequency reconstruction. A more precise value would be obtained, if the temporal behavior was sampled continuously providing the measuring time is not a concern.

If one would want to reconstruct the spatial trajectory, a smaller sampling interval might be needed. Additionally, for further analysis the measurement of the whole brain volume with motion encoding in all three spatial directions is probably needed at some point.

All this would lead to increased measuring time and means to speed up the measurement process would be required. One limiting factor right now is the long repetition time of $T_R = 3000\,\text{ms}$ which was chosen this long in order to have no additional excitation when the shell stopped abruptly in the upper position. Complementary damping for the upper shell position and a pneumatic system allowing for higher

pressure may permit to reduce T_R and thus reduce the measuring time. Alternatively, a more advanced control mechanism (microprocessor controls) for the high pressure valves that would allow for an initial high pressure to lift the shell quickly but then decelerate the upward motion to reduce the excitation at the highest point could be used to reduce the lifting time. Another approach to reduce the measuring time for 3D measurements would be the implementation of a multi slice sequence.

Regarding the choice of motion encoding gradients two contradictory demands had to be balanced. On the one hand, stronger and longer gradients raise the sensitivity of the motion encoding and should lead to a higher phase contrast [65]. On the other hand, the higher contrast leads to more phase jumps and, thus, to a higher risk of artifacts after the phase unwrapping, potentially rendering the image too distorted to evaluate. Additionally, operating strong gradients can induce a vibration in the MR table resulting in a - for these measurements - unwanted excitation [94]. While gradients with a low amplitude and long duration also increase the sensitivity, applying long gradients also means averaging the phase offset over a longer time and potential loosing temporal resolution. For the two gradient settings used for the volunteers, no significant difference could be observed.

4.6.3 Conclusion

Examining the capabilities of the lifting device and its components (like the pneumatic system) in practical applications revealed that some modifications are needed to make the excitation more reproducible for different measurement sets. In the pneumatic system the valves need to be able to work in a wider range and the system needs to be powerful enough to lift the shell always to the upper position determined by the stoppers. The lifting device should be adapted to provide more independence from the weight distribution. An additional stabilization (like in the form of additional flat springs) at the superior part of the shell may help to prevent the rotations. In order to reduce the effects of the not well controllable bouncing of the shell after the initial landing, the addition of a dampening material was conceived but not implemented in time for the measurements of this thesis (preliminary work on this was done by Roberto Correa Schragen in the course of his bachelor thesis). It would also be beneficial to gauge the optical positioning system to interpret the excitation more quantitatively. A quite different variation of the lifting device is conceived by Jakob Bindl [120]. It is controlled not by a pneumatic system but a stepping motor and might provide more reproducible and flexible excitations.

In order to extract a more reliable frequency, the measuring protocol should also be adjusted in the future. Especially with probes for which a low frequency is expected a longer time series should be measured. The sampling interval $\Delta\tau$ should be chosen intelligently to balance both the accuracy and the measuring time.

Summary

In this thesis first systematic measurements using magnetic resonance rheology (MRR) have been presented.

MRR is a novel technique designed to image the mechanical properties of human brain tissue by performing a creep relaxation experiment inside an magnetic resonance imaging (MRI) scanner. Using a lifting device inside the head coil the head is basically dropped a distance of approximately 1 mm. The response of the brain tissue to this shock excitation is then measured using motion sensitive phase imaging.

Hydrogels with varying stiffness inside PMMA containers with different sizes were used as phantoms emulating the soft brain tissue inside the hard skull to investigate the response to the excitation. In order to remove the influence of the macroscopic fall movement and to evaluate and compare the measurements without calculating the physical trajectory from the phase, the relative phase $\Delta\phi$ was introduced. The temporal behavior of $\Delta\phi$ showed that oscillations are excited by the shock excitation. The frequencies f extracted from this phase showed a reasonably even distribution over the volume of the phantom. From measurements of different phantoms it was investigated how f depends on the stiffness and the diameter of the phantom. The frequency increased with rising stiffness and decreased with rising diameter, as would be expected from qualitative, theoretical considerations, indicating that the frequency can be used as a measure for the bulk properties of the material. A preliminary investigation on the influence of a different coupling between the phantom material and the container walls was also performed.

Additionally to homogeneous phantoms, different kinds of inhomogeneous phantoms were investigated. For phantoms consisting of two layers of differently stiff hydrogel even the smallest differences in stiffness investigated ($\Delta G = 0.77\,\mathrm{kPa}$) could be resolved in the phase images while other analyzing techniques provided not always a distinct result. Using phase strain images and relative phase cuts it could be shown that cubic hydrogel and fluid filled inclusions can be resolved as well.

Additionally, ten healthy volunteers were measured and showed a response expected from the phantom measurements. From the distinct oscillations in each hemisphere a frequency could be extracted which showed mostly comparable values over the ten volunteers. In both the phase and phase strain images similar localized features were visible, some corresponding to anatomical structures like sulci.

These results show that *in vivo* MRR measurements of the human brain are feasible and comparable and though there is room for improvement concerning the reproducibility of the excitation between different measurement sets, MRR appears to be an interesting tool to investigate human brain tissue.

A Appendix

A.1 Brain Sizes

The dimensions of the brain of each volunteer has been extracted from a high resolution magnitude image. The extent in the anterior - posterior direction and in left - right direction was measured at the widest location in the measured slice using the ImageJ measure option [112, 113]. The data is plotted in fig. A.1. All data points lie in the range of 147-167 mm for AP and 117-133 mm for LR. It has to be kept in mind that this data gives just an estimate of the brain dimensions since neither different shapes nor the vertical extension of the brain is taken into account.

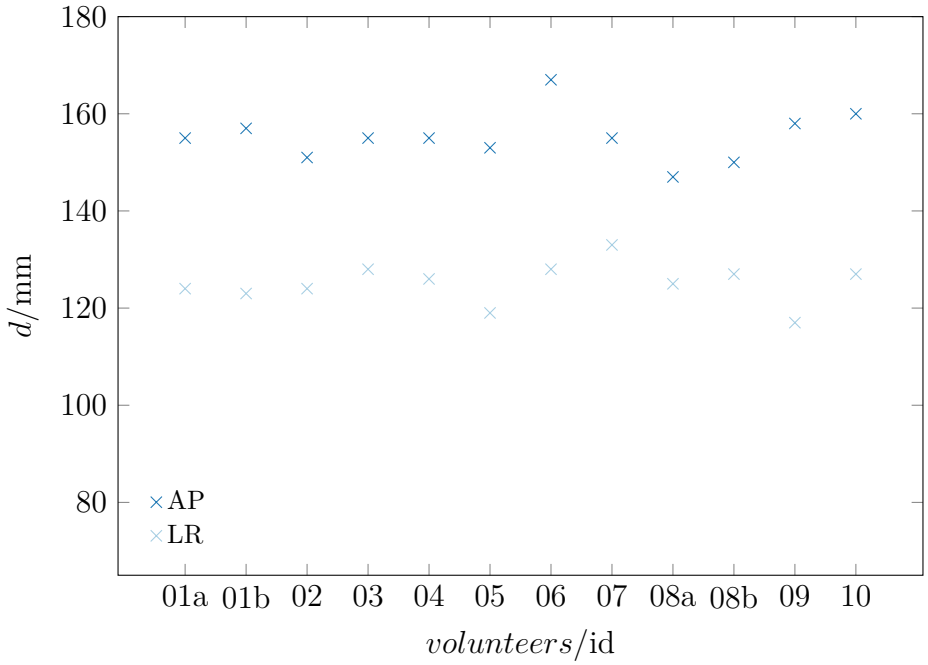

Figure A.1: *Brain dimensions:*
The extension of the brains of the volunteers at its widest location is plotted for the anterior - posterior (AP) and the left - right (LR) direction. All data points lie in the range of 147-167 mm for AP and 117-133 mm for LR.

Bibliography

[1] K. J. Parker, M. M. Doyley, and D. J. Rubens. "Imaging the elastic properties of tissue: the 20 year perspective". In: *Physics in medicine and biology* 56.1 (2011), R1–R29. ISSN: 1361-6560. DOI: 10.1088/0031-9155/56/1/R01 (cit. on pp. 1 sq.).

[2] R. M. Lerner et al. "Sono-Elasticity: Medical Elasticity Images Derived from Ultrasound Signals in Mechanically Vibrated Targets". In: *Acoustical Imaging: Proceedings of the Sixteenth International Symposium, June 10–12, 1987*. Ed. by L. W. Kessler. Vol. 16. Boston and MA: Springer US, 1988, pp. 317–327. ISBN: 978-1-4613-0725-9. DOI: 10.1007/978-1-4613-0725-9_31. URL: http://dx.doi.org/10.1007/978-1-4613-0725-9%5C_31 (cit. on p. 1).

[3] D. Berger. "A brief history of medical diagnosis and the birth of the clinical laboratory: Part 1 - Ancient times through the 19th century". In: *MLO Med Lab Obs* 31.7 (1999), pp. 28–30 (cit. on p. 1).

[4] K. Stern. *The pillar of fire*. New York: Harcourt, Brace and Company, 1951 (cit. on p. 1).

[5] R. Porter. *The Cambridge illustrated history of medicine*. Cambridge illustrated history. Cambridge and New York: Cambridge University Press, 1996. ISBN: 0-521-44211-7 (cit. on p. 1).

[6] Wells, P. N. T. and H.-D. Liang. "Medical ultrasound: imaging of soft tissue strain and elasticity". In: *J. R. Soc. Interface* 8 (2011), pp. 1521–1549. DOI: 10.1098/rsif.2011.0054 (cit. on pp. 1 sq.).

[7] A. Stanton. "Wilhelm Conrad Röntgen on a new kind of rays: Translation of a paper read before the Würzburg Physical and Medical Society, 1895". In: *Nature* 53 (1896), pp. 274–276. ISSN: 0028-0836 (cit. on p. 1).

[8] J. J. Wild and J. M. Reid. "Application of Echo-Ranging Techniques to the Determination of Structure of Biological Tissues". In: *Science* 115.2983 (1952), pp. 226–230. ISSN: 0036-8075. DOI: 10.1126/science.115.2983.226 (cit. on p. 1).

[9] D. H. Howry and W. R. Bliss. "Ultrasonic visualization of soft tissue structures of the body". In: *The Journal of laboratory and clinical medicine* 40.4 (1952), p. 579 (cit. on p. 1).

[10] I. Donald, J. Macvicar, and T. G. Brown. "Investigation of abdominal masses by pulsed ultrasound". In: *The Lancet* 271.7032 (1958), pp. 1188–1195 (cit. on p. 1).

[11] G. Watts. “John Wild”. In: *BMJ* 339 (2009). ISSN: 0959-8138. DOI: 10.1136/bmj.b4428. URL: http://www.bmj.com/content/339/bmj.b4428 (cit. on p. 1).

[12] S. Webb and M. A. Flower. *Webb's physics of medical imaging*. 2nd ed. Series in medical physics and biomedical engineering. Boca Raton: Taylor & Francis, 2012. ISBN: 0750305738 (cit. on pp. 1, 5).

[13] G. Ansell and J. Rotblat. “Radioactive Iodine as a Diagnostic Aid for Intrathoracic Goitre”. In: *The British Journal of Radiology* 21.251 (1948), pp. 552–558. ISSN: 0007-1285. DOI: 10.1259/0007-1285-21-251-552 (cit. on p. 1).

[14] M. E. Phelps et al. “Application of Annihilation Coincidence Detection to Transaxial Reconstruction Tomography”. In: *Journal of Nuclear Medicine* 16.3 (1975), pp. 210–224. URL: http://jnm.snmjournals.org/content/16/3/210.short (cit. on p. 1).

[15] G. L. Brownell. “A history of positron imaging”. In: *Physics Research Laboratory, Massachusetts General Hospital, MIT* (1999) (cit. on p. 1).

[16] G. N. Hounsfield. “Computerized transverse axial scanning (tomography): Part 1. Description of system”. In: *The British Journal of Radiology* 46.552 (1973), pp. 1016–1022. ISSN: 0007-1285. DOI: 10.1259/0007-1285-46-552-1016 (cit. on p. 1).

[17] J. Ambrose. “Computerized transverse axial scanning (tomography): Part 2. Clinical application*”. In: *The British Journal of Radiology* 46.552 (1973), pp. 1023–1047. ISSN: 0007-1285. DOI: 10.1259/0007-1285-46-552-1023 (cit. on p. 1).

[18] E. C. Beckmann. “CT scanning the early days”. In: *The British Journal of Radiology* 79 (2006), pp. 5–8. DOI: 10.1259/bjr/29444122 (cit. on p. 1).

[19] I. R. Young. “Significant events in the development of MRI”. In: *Journal of Magnetic Resonance Imaging* 20 (2004), pp. 183–186. DOI: 10.1002/jmri.20123 (cit. on pp. 1, 5).

[20] P. C. Lauterbur. “Image Formation by Induced Local Interactions: Examples Employing Nuclear Magnetic Resonance”. In: *Nature* 242 (1973), pp. 190–191. ISSN: 0028-0836 (cit. on pp. 1, 5).

[21] R. Damadian. “Tumor Detection by Nuclear Magnetic Resonance”. In: *Science* 171.3976 (1971), pp. 1151–1153. ISSN: 0036-8075. DOI: 10.1126/science.171.3976.1151. URL: http://science.sciencemag.org/content/171/3976/1151 (cit. on pp. 1, 5).

[22] M. M. Doyley and K. J. Parker. “Elastography”. In: *Ultrasound Clinics* 9.1 (2014), pp. 1–11. ISSN: 1556858X. DOI: 10.1016/j.cult.2013.09.006 (cit. on p. 1).

[23] H. L. Oestreicher. "Field and impedance of an oscillating sphere in a viscoelastic medium with an application to biophysics". In: *The Journal of the Acoustical Society of America* 23.6 (1951), pp. 707–714 (cit. on p. 1).

[24] von Gierke, H. E. et al. "Physics of vibrations in living tissues". In: *Journal of applied physiology* 4.12 (1952), pp. 886–900 (cit. on p. 1).

[25] R. J. Dickinson and C. R. Hill. "Measurement of soft tissue motion using correlation between A-scans". In: *Ultrasound in Medicine & Biology* 8.3 (1982), pp. 263–271. ISSN: 03015629. DOI: 10.1016/0301-5629(82)90032-1 (cit. on p. 1).

[26] L. S. Wilson and D. E. Robinson. "Ultrasonic measurement of small displacements and deformations of tissue". In: *Ultrasonic Imaging* 4.1 (1982), pp. 71–82. DOI: 10.1016/0161-7346(82)90006-2 (cit. on p. 1).

[27] T. A. Krouskop, Dougherty, F. S. Vinson, et al. "A pulsed Doppler ultrasonic system for making noninvasive measurements of the mechanical properties of soft tissue". In: *J Rehabil Res Dev* 24.2 (1987), pp. 1–8 (cit. on p. 1).

[28] J. Ophir et al. "Elastography: A Quantitative Method for Imaging the Elasticity of Biological Tissues". In: *Ultrasonic Imaging* 13.2 (1991), pp. 111–134. DOI: 10.1177/016173469101300201 (cit. on p. 2).

[29] A. P. Sarvazyan et al. "Shear wave elasticity imaging: a new ultrasonic technology of medical diagnostics". In: *Ultrasound in Medicine & Biology* 24.9 (1998), pp. 1419–1435. ISSN: 03015629. DOI: 10.1016/S0301-5629(98)00110-0 (cit. on p. 2).

[30] S. Catheline, F. Wu, and M. Fink. "A solution to diffraction biases in sonoelasticity: The acoustic impulse technique". In: *The Journal of the Acoustical Society of America* 105.5 (1999), p. 2941. ISSN: 00014966. DOI: 10.1121/1.426907 (cit. on p. 2).

[31] J. J. Dahl et al. "4K-5 Shear Wave Velocity Estimation Using Acoustic Radiation Force Impulsive Excitation in Liver In Vivo". In: *2006 IEEE Ultrasonics Symposium*, pp. 1156–1160. DOI: 10.1109/ULTSYM.2006.298 (cit. on p. 2).

[32] T. Sugimoto, S. Ueha, and K. Itoh. "Tissue hardness measurement using the radiation force of focused ultrasound". In: *IEEE Symposium on Ultrasonics*. 4-7 Dec. 1990, pp. 1377–1380. DOI: 10.1109/ULTSYM.1990.171591 (cit. on p. 2).

[33] J. Bercoff, M. Tanter, and M. Fink. "Supersonic shear imaging: a new technique for soft tissue elasticity mapping". In: *IEEE Transactions on Ultrasonics, Ferroelectrics and Frequency Control* 51.4 (2004), pp. 396–409. ISSN: 0885-3010. DOI: 10.1109/TUFFC.2004.1295425 (cit. on p. 2).

[34] K. R. Nightingale et al. "On the feasibility of remote palpation using acoustic radiation force". In: *The Journal of the Acoustical Society of America* 110.1 (2001), p. 625. ISSN: 00014966. DOI: 10.1121/1.1378344 (cit. on p. 2).

[35] R. Muthupillai et al. “Magnetic resonance elastography by direct visualization of propagating acoustic strain waves”. In: *Science* 269.5232 (1995), pp. 1854–1857. ISSN: 0036-8075. DOI: 10.1126/science.7569924 (cit. on pp. 2, 26).

[36] R. Muthupillai et al. “Magnetic resonance imaging of transverse acoustic strain waves”. In: *Magnetic Resonance in Medicine* 36.2 (1996), pp. 266–274. ISSN: 07403194. DOI: 10.1002/mrm.1910360214 (cit. on p. 2).

[37] M. Radicke et al. “New image contrast method in magnetic resonance imaging via ultrasound”. In: *HFI/NQI 2007*. Ed. by A. Pasquevich et al. Berlin and Heidelberg: Springer Berlin Heidelberg, 2008, pp. 541–546. ISBN: 978-3-540-85319-0. DOI: 10.1007/978-3-540-85320-6_85 (cit. on p. 2).

[38] N. McDannold and S. E. Maier. “Magnetic resonance acoustic radiation force imaging”. In: *Medical Physics* 35.8 (2008), p. 3748. ISSN: 00942405. DOI: 10.1118/1.2956712 (cit. on p. 2).

[39] J. Mende et al. “Acoustic radiation force contrast in MRI: Detection of calcifications in tissue-mimicking phantoms”. In: *Medical Physics* 37.12 (2010), p. 6347. ISSN: 00942405. DOI: 10.1118/1.3512806 (cit. on p. 2).

[40] M. Radicke et al. “Acoustic Radiation Contrast in MR Images for Breast Cancer Diagnostics - Initial Phantom Study”. In: *Ultrasound in Medicine & Biology* 37.2 (2011), pp. 253–261. ISSN: 03015629. DOI: 10.1016/j.ultrasmedbio.2010.11.005 (cit. on p. 2).

[41] U. Zaleska-Dorobisz et al. “Ultrasound elastography - review of techniques and its clinical applications”. In: *Advances in clinical and experimental medicine : official organ Wroclaw Medical University* 23.4 (2014), pp. 645–655. ISSN: 1899-5276 (cit. on p. 2).

[42] Y. K. Mariappan, K. J. Glaser, and R. L. Ehman. “Magnetic resonance elastography: a review”. In: *Clinical anatomy (New York, N.Y.)* 23.5 (2010), pp. 497–511. ISSN: 1098-2353. DOI: 10.1002/ca.21006 (cit. on pp. 2, 26).

[43] K. J. Glaser, A. Manduca, and R. L. Ehman. “Review of MR elastography applications and recent developments”. In: *Journal of magnetic resonance imaging : JMRI* 36.4 (2012), pp. 757–774. ISSN: 1522-2586. DOI: 10.1002/jmri.23597 (cit. on pp. 2, 26).

[44] L. Xu et al. “Magnetic Resonance Elastography of the Human Brain: A Preliminary Study”. In: *Acta radiologica* 48.1 (2007), pp. 112–115. DOI: 10.1080/02841850601026401 (cit. on pp. 2, 26).

[45] S. A. Kruse et al. “Magnetic resonance elastography of the brain”. In: *NeuroImage* 39.1 (2008), pp. 231–237. ISSN: 1095-9572. DOI: 10.1016/j.neuroimage.2007.08.030 (cit. on pp. 2, 26).

[46] L. Xu et al. “Magnetic Resonance Elastography of Brain Tumors: Preliminary Results”. In: *Acta radiologica* 48.3 (2007), pp. 327–330. DOI: 10.1080/02841850701199967 (cit. on p. 2).

[47] M. C. Murphy et al. “Preoperative assessment of meningioma stiffness using magnetic resonance elastography”. In: *Journal of Neurosurgery* 118.3 (2013), pp. 643–648. ISSN: 0022-3085. DOI: 10.3171/2012.9.JNS12519 (cit. on p. 2).

[48] M. Reiss-Zimmermann et al. “High Resolution Imaging of Viscoelastic Properties of Intracranial Tumours by Multi-Frequency Magnetic Resonance Elastography”. In: *Clinical Neuroradiology* 25.4 (2015), pp. 371–378. ISSN: 1869-1439. DOI: 10.1007/s00062-014-0311-9 (cit. on p. 2).

[49] K.-J. Streitberger et al. “High-Resolution Mechanical Imaging of Glioblastoma by Multifrequency Magnetic Resonance Elastography”. In: *PLoS ONE* 9.10 (2014), e110588. ISSN: 1932-6203. DOI: 10.1371/journal.pone.0110588 (cit. on p. 2).

[50] J. Wuerfel et al. “MR-elastography reveals degradation of tissue integrity in multiple sclerosis”. In: *NeuroImage* 49.3 (2010), pp. 2520–2525. ISSN: 1095-9572. DOI: 10.1016/j.neuroimage.2009.06.018 (cit. on p. 2).

[51] K.-J. Streitberger et al. “Brain Viscoelasticity Alteration in Chronic-Progressive Multiple Sclerosis”. In: *PLoS ONE* 7.1 (2012), e29888. ISSN: 1932-6203. DOI: 10.1371/journal.pone.0029888 (cit. on p. 2).

[52] M. C. Murphy et al. “Decreased brain stiffness in Alzheimer’s disease determined by magnetic resonance elastography”. In: *Journal of magnetic resonance imaging : JMRI* 34.3 (2011), pp. 494–498. ISSN: 1522-2586. DOI: 10.1002/jmri.22707 (cit. on p. 2).

[53] A. Lipp et al. “Cerebral magnetic resonance elastography in supranuclear palsy and idiopathic Parkinson’s disease”. In: *NeuroImage: Clinical* 3 (2013), pp. 381–387. ISSN: 22131582. DOI: 10.1016/j.nicl.2013.09.006 (cit. on p. 2).

[54] K.-J. Streitberger et al. “In vivo viscoelastic properties of the brain in normal pressure hydrocephalus”. In: *NMR in Biomedicine* (2010), n/a. ISSN: 09523480. DOI: 10.1002/nbm.1602 (cit. on p. 2).

[55] F. B. Freimann et al. “Alteration of brain viscoelasticity after shunt treatment in normal pressure hydrocephalus”. In: *Neuroradiology* 54.3 (2012), pp. 189–196. ISSN: 0028-3940. DOI: 10.1007/s00234-011-0871-1 (cit. on p. 2).

[56] M. M. Doyley. “Model-based elastography: a survey of approaches to the inverse elasticity problem”. In: *Physics in medicine and biology* 57.3 (2012), R35–73. ISSN: 1361-6560. DOI: 10.1088/0031-9155/57/3/R35 (cit. on pp. 2, 27).

[57] J. B. Weaver et al. “Brain mechanical property measurement using MRE with intrinsic activation”. In: *Physics in medicine and biology* 57.22 (2012), pp. 7275–7287. ISSN: 1361-6560. DOI: 10.1088/0031-9155/57/22/7275 (cit. on pp. 2, 26 sq.).

[58] R. J. Okamoto et al. “Comparison of MR Elastography Inversion Methods on High-Resolution Measurements in the Human Brain”. In: *Proceedings of the Joint Annual Meeting ISMRM-ESMRMB*. 2014, p. 4269 (cit. on p. 2).

[59] S. Chatelin, A. Constantinesco, and R. Willinger. “Fifty years of brain tissue mechanical testin: From in vitro to in vivo investigations”. In: *Biorheology* 47.5 (2010), pp. 255–276. DOI: 10.3233/BIR-2010-0576 (cit. on pp. 2, 25 sq.).

[60] A.-L. Kofahl et al. “MR-Rheology - A feasibility study with phantoms”. In: *Proceedings of the Joint Annual Meeting ISMRM-ESMRMB*. 2014, p. 1689 (cit. on pp. 2, 29).

[61] S. Theilenberg et al. “Magnetic Resonance Rheology of the human brain”. In: *Proceedings of the Joint Annual Meeting ISMRM-ESMRMB*. 2014, p. 1690 (cit. on pp. 2, 29).

[62] A.-L. Kofahl et al. “Combining rheology and MRI: Imaging healthy and tumorous brains based on mechanical properties”. In: *Magnetic resonance in medicine* (2016), n/a–n/a. ISSN: 0740-3194. DOI: 10.1002/mrm.26477. URL: http://dx.doi.org/10.1002/mrm.26477 (cit. on pp. 2 sq., 50, 58, 60, 75, 78 sq., 89, 94).

[63] P. V. Bayly et al. “Deformation of the Human Brain Induced by Mild Acceleration”. In: *Journal of Neurotrauma* 22.8 (2005), pp. 845–856. ISSN: 0897-7151. DOI: 10.1089/neu.2005.22.845 (cit. on p. 2).

[64] E. A. Zerhouni et al. “Human heart: tagging with MR imaging–a method for noninvasive assessment of myocardial motion”. In: *Radiology* 169.1 (1988), pp. 59–63. ISSN: 0033-8419. DOI: 10.1148/radiology.169.1.3420283 (cit. on p. 2).

[65] D. Ulucay. “Rheologie im Kopf”. PhD thesis. Bonn: Rheinische Friedrich-Wilhelms-Universität, 2015. URL: http://hss.ulb.uni-bonn.de/2015/3925/3925.pdf (visited on 08/05/2015) (cit. on pp. 2, 29, 31, 34, 89, 92, 98 sq.).

[66] I. I. Rabi et al. “A New Method of Measuring Nuclear Magnetic Moment”. In: *Phys. Rev.* 53.4 (1938), p. 318. DOI: 10.1103/PhysRev.53.318. URL: http://link.aps.org/doi/10.1103/PhysRev.53.318 (cit. on p. 5).

[67] F. Bloch, W. Hansen, and M. Packard. “Nuclear Induction”. In: *Physical Review* 69.3-4 (1946), p. 127. ISSN: 0031-899X. DOI: 10.1103/PhysRev.69.127 (cit. on p. 5).

[68] E. Purcell, H. Torrey, and R. Pound. “Resonance Absorption by Nuclear Magnetic Moments in a Solid”. In: *Physical Review* 69.1-2 (1946), pp. 37–38. ISSN: 0031-899X. DOI: 10.1103/PhysRev.69.37 (cit. on p. 5).

[69] C. Kittel. *Einführung in die Festkörperphysik*. 14., überarb. und erw. Aufl. München [u.a.]: Oldenbourg, 2006. ISBN: 3486577239 (cit. on p. 5).

[70] E. Fukushima and Roeder, S. B. W. *Experimental pulse NMR: A nuts and bolts approach*. Reading and Mass.: Addison-Wesley Pub. Co., Advanced Book Program, 1981. ISBN: 9780201104035 (cit. on p. 5).

[71] M. T. Vlaardingerbroek and J. A. Boer. *Magnetresonanzbildgebung: Theorie und Praxis*. Berlin [u.a.]: Springer, 2004. ISBN: 9783540200284 (cit. on p. 5).

[72] M. A. Bernstein, K. F. King, and X. J. Zhou. *Handbook of MRI pulse sequences*. Amsterdam and Boston: Academic Press, 2004. ISBN: 9781281038135 (cit. on pp. 5, 13 sq., 35).

[73] O. Dössel. *Bildgebende Verfahren in der Medizin: Von der Technik zur medizinischen Anwendung*. Berlin: Springer, 2000. ISBN: 9783540660149 (cit. on p. 5).

[74] S. Theilenberg. *Figure: Magnetization*. Ed. by A.-L. Kofahl. 2015 (cit. on p. 7).

[75] D. Weishaupt, V. D. Köchli, and B. Marincek. *Wie funktioniert MRI? Eine Einführung in Physik und Funktionsweise der Magnetresonanzbildgebung ; mit 9 Tabellen*. 6. Aufl. Heidelberg: Springer, 2009. ISBN: 3540895728 (cit. on p. 9).

[76] C. W. Macosko. *Rheology: Principles, measurements, and applications*. Advances in interfacial engineering series. New York: VCH, 1994. ISBN: 0471185752 (cit. on p. 15).

[77] M. Pahl, W. Gleißle, and H.-M. Laun. *Praktische Rheologie der Kunststoffe und Elastomere*. Kunststofftechnik. Düsseldorf: VDI-Verlag, op. 1991. ISBN: 9783182341550 (cit. on pp. 15–23).

[78] H. Giesekus. *Phänomenologische Rheologie: Eine Einführung*. Berlin and New York: Springer-Verlag, 1994. ISBN: 9780387575131 (cit. on p. 15).

[79] S. D. Gertz, M. Schünke, and M. Liebman. *Basiswissen Neuroanatomie: Leicht verständlich - knapp - klinikbezogen*. 4., unveränd. Aufl. Stuttgart [u.a.]: Thieme, 2003. ISBN: 9783131144041 (cit. on p. 23).

[80] N. Ulfig. *Kurzlehrbuch Neuroanatomie: 50 Tabellen*. Stuttgart [u.a.]: Thieme, 2008. ISBN: 9783131429513 (cit. on p. 23).

[81] H. Gray and W. H. Lewis. *Anatomy of the human body*. 20th ed. Philadelphia: Lea & Febiger, 1918. ISBN: 1-58734-102-6 (cit. on pp. 24 sq.).

[82] R. L. Drake, W. Vogl, and Mitchell, A. W. M. *Gray's Anatomie für Studenten*. 1. Aufl. München [u.a.]: Elsevier, Urban & Fischer, 2007. ISBN: 3437412310 (cit. on p. 24).

[83] M. A. Patestas and L. P. Gartner. *A textbook of neuroanatomy*. Malden and MA: Blackwell Pub., 2006. ISBN: 1444309072 (cit. on p. 24).

[84] K. Miller. *Biomechanics of the brain*. Biological and medical physics, biomedical engineering. New York: Springer, 2011. ISBN: 1441999973 (cit. on pp. 25 sqq.).

[85] M. Trepel. *Neuroanatomie: Struktur und Funktion ; [Online-Zugang + interaktive Extras]*. 4., neu bearb. Aufl. StudentConsult. München and Jena: Elsevier, Urban & Fischer, 2008. ISBN: 3437412981 (cit. on p. 25).

[86] G. T. Fallenstein, V. D. Hulce, and J. W. Melvin. "Dynamic mechanical properties of human brain tissue". In: *Journal of Biomechanics* 2.3 (1969), pp. 217–226. ISSN: 00219290. DOI: 10.1016/0021-9290(69)90079-7 (cit. on p. 25).

[87] J. E. Galford and J. H. McElhaney. “A viscoelastic study of scalp, brain, and dura”. In: *Journal of Biomechanics* 3.2 (1970), pp. 211–221. ISSN: 00219290. DOI: 10.1016/0021-9290(70)90007-2 (cit. on p. 25).

[88] S. Cheng, E. C. Clarke, and L. E. Bilston. “Rheological properties of the tissues of the central nervous system: a review”. In: *Medical engineering & physics* 30.10 (2008), pp. 1318–1337. ISSN: 1350-4533. DOI: 10.1016/j.medengphy.2008.06.003 (cit. on pp. 25 sq.).

[89] M. Scholz et al. “Current status of intraoperative real-time vibrography in neurosurgery”. In: *Ultraschall in der Medizin (Stuttgart, Germany : 1980)* 28.5 (2007), pp. 493–497. ISSN: 0172-4614. DOI: 10.1055/s-2006-927359 (cit. on p. 26).

[90] P. Schiavone et al. “In vivo measurement of human brain elasticity using a light aspiration device”. In: *Medical image analysis* 13.4 (2009), pp. 673–678. ISSN: 1361-8423. DOI: 10.1016/j.media.2009.04.001 (cit. on p. 26).

[91] I. Sack et al. “The impact of aging and gender on brain viscoelasticity”. In: *NeuroImage* 46.3 (2009), pp. 652–657. ISSN: 1095-9572. DOI: 10.1016/j.neuroimage.2009.02.040 (cit. on pp. 26, 97).

[92] M. A. Green, L. E. Bilston, and R. Sinkus. “In vivo brain viscoelastic properties measured by magnetic resonance elastography”. In: *NMR in biomedicine* 21.7 (2008), pp. 755–764. ISSN: 0952-3480. DOI: 10.1002/nbm.1254 (cit. on p. 26).

[93] J. Braun et al. “High-resolution mechanical imaging of the human brain by three-dimensional multifrequency magnetic resonance elastography at 7T”. In: *NeuroImage* 90 (2014), pp. 308–314. ISSN: 1095-9572. DOI: 10.1016/j.neuroimage.2013.12.032 (cit. on p. 26).

[94] D. Gallichan et al. “TREMR: Table-resonance elastography with MR”. In: *Magnetic resonance in medicine* 62.3 (2009), pp. 815–821. ISSN: 0740-3194. DOI: 10.1002/mrm.22046. URL: http://dx.doi.org/10.1002/mrm.22046 (cit. on pp. 26, 99).

[95] W. Barber, J. Brockway, and L. Higgins. “The density of tissue in and about the head”. In: *Acta Neurol. Scandinav.* 46 (1970), pp. 85–92 (cit. on p. 26).

[96] G. Franceschini et al. “Brain tissue deforms similarly to filled elastomers and follows consolidation theory”. In: *Journal of the Mechanics and Physics of Solids* 54.12 (2006), pp. 2592–2620. ISSN: 00225096. DOI: 10.1016/j.jmps.2006.05.004 (cit. on pp. 26 sq.).

[97] van Dommelen, J. A. W., M. Hrapko, and G. W. M. Peters. “Constitutive Modelling of Brain Tissue for Prediction of Traumatic Brain Injury”. In: *Neural Tissue Biomechanics*. Ed. by L. E. Bilston. Vol. 3. Studies in Mechanobiology, Tissue Engineering and Biomaterials. Berlin and Heidelberg: Springer Berlin Heidelberg, 2011, pp. 41–67. ISBN: 978-3-642-13889-8. DOI: 10.1007/8415_2010_16 (cit. on p. 27).

[98] Van Houten, E. E. W. et al. "An overlapping subzone technique for MR-based elastic property reconstruction". In: *Magnetic resonance in medicine* 42.4 (1999), pp. 779–786. ISSN: 0740-3194. DOI: 10.1002/(SICI)1522-2594(199910)42:4<779::AID-MRM21>3.0.CO;2-Z (cit. on p. 27).

[99] Van Houten, E. E. W. et al. "Three-dimensional subzone-based reconstruction algorithm for MR elastography". In: *Magnetic Resonance in Medicine* 45.5 (2001), pp. 827–837. ISSN: 07403194. DOI: 10.1002/mrm.1111 (cit. on p. 27).

[100] P. R. Perriñez et al. "Magnetic resonance poroelastography: an algorithm for estimating the mechanical properties of fluid-saturated soft tissues". In: *IEEE transactions on medical imaging* 29.3 (2010), pp. 746–755. ISSN: 1558-254X. DOI: 10.1109/TMI.2009.2035309 (cit. on p. 27).

[101] J. Finsterbusch. *SE-EPI 2D DIFF*. 2009-2015 (cit. on p. 34).

[102] N. Yoganandan et al. "Physical properties of the human head: mass, center of gravity and moment of inertia". In: *Journal of Biomechanics* 42.9 (2009), pp. 1177–1192. ISSN: 00219290. DOI: 10.1016/j.jbiomech.2009.03.029 (cit. on p. 39).

[103] U. Hamhaber et al. "Comparison of quantitative shear wave MR-elastography with mechanical compression tests". In: *Magnetic resonance in medicine* 49.1 (2003), pp. 71–77. ISSN: 0740-3194. DOI: 10.1002/mrm.10343 (cit. on pp. 39 sq.).

[104] E. E. Konofagou and K. Hynynen. "Localized harmonic motion imaging: theory, simulations and experiments". In: *Ultrasound in Medicine & Biology* 29.10 (2003), pp. 1405–1413. ISSN: 03015629. DOI: 10.1016/S0301-5629(03)00953-0 (cit. on p. 39).

[105] T. Z. Pavan et al. "Nonlinear elastic behavior of phantom materials for elastography". In: *Physics in Medicine and Biology* 55.9 (2010), pp. 2679–2692. ISSN: 0031-9155. DOI: 10.1088/0031-9155/55/9/017 (cit. on p. 39).

[106] C. L. Johnson et al. "Magnetic resonance elastography of the brain using multishot spiral readouts with self-navigated motion correction". In: *Magnetic resonance in medicine* 70.2 (2013), pp. 404–412. ISSN: 0740-3194. DOI: 10.1002/mrm.24473 (cit. on p. 39).

[107] M. Lahaye and C. Rochas. "Chemical structure and physico-chemical properties of agar". In: *International Workshop on Gelidium*. Ed. by J. A. Juanes, B. Santelices, and J. L. McLachlan. Dordrecht: Springer Netherlands, 1991, pp. 137–148. ISBN: 978-94-010-5601-4. DOI: 10.1007/978-94-011-3610-5_13 (cit. on p. 39).

[108] T. Fujii et al. "Scaling Analysis of the Concentration Dependence on Elasticity of Agarose Gel". In: *Bioscience, Biotechnology, and Biochemistry* 64.8 (2014), pp. 1618–1622. ISSN: 0916-8451. DOI: 10.1271/bbb.64.1618 (cit. on p. 40).

[109] M. Tokita and K. Hikichi. "Mechanical studies of sol-gel transition: Universal behavior of elastic modulus". In: *Physical Review A* 35.10 (1987), pp. 4329–4333. ISSN: 0556-2791. DOI: 10.1103/PhysRevA.35.4329 (cit. on p. 40).

[110] T. J. Hall et al. "Phantom materials for elastography". In: *IEEE Transactions on Ultrasonics, Ferroelectrics and Frequency Control* 44.6 (1997), pp. 1355–1365. ISSN: 0885-3010. DOI: 10.1109/58.656639 (cit. on p. 40).

[111] UHU GmbH & Co. KG. *Data sheet: 47853 - UHU Poly Max® Glasklar Express Kartuschehe 300 g DE/FR/IT - 47855*. URL: http://www.uhu-profi.de/uploads/tx%5C_ihtdatasheets/TDS%5C_UHU%5C_Poly%5C_Maxr%5C_Glasklar%5C_Express%5C_Kartusche%5C_300%5C_g%5C_DE%5C_FR%5C_IT%5C_%5C_G.PDF (visited on 04/29/2016) (cit. on p. 41).

[112] W. S. Rasband. *ImageJ*. Bethesda, Maryland, and USA, 1997-2014. URL: http://imagej.nih.gov/ij/ (visited on 08/18/2015) (cit. on pp. 44, 103).

[113] C. A. Schneider, W. S. Rasband, and K. W. Eliceiri. "NIH Image to ImageJ: 25 years of image analysis". In: *Nature Methods* 9.7 (2012), pp. 671–675. ISSN: 1548-7091. DOI: 10.1038/nmeth.2089 (cit. on pp. 44, 103).

[114] S. Theilenberg. *PyMRR*. 2015. URL: https://github.com/theilen/PyMRR (visited on 08/28/2015) (cit. on p. 44).

[115] D. C. Ghiglia and M. D. Pritt. *Two-dimensional phase unwrapping: Theory, algorithms, and software*. New York: Wiley, 1998. ISBN: 0471249351 (cit. on p. 44).

[116] R. M. Goldstein, H. A. Zebker, and C. L. Werner. "Satellite radar interferometry: Two-dimensional phase unwrapping". In: *Radio Science* 23.4 (1988), pp. 713–720. ISSN: 00486604. DOI: 10.1029/RS023i004p00713 (cit. on p. 44).

[117] W. Stephan and R. Postl. *Schwingung elastischer Kontinua*. Vol. 72. Leitfäden der angewandten Mathematik und Mechanik. Stuttgart: Teubner, 1995. ISBN: 3-519-02377-6 (cit. on pp. 58 sq.).

[118] S. Theilenberg. "Dissertation: To be published". PhD thesis. Bonn: Rheinische Friedrich-Wilhelms-Universität, 2017 (cit. on pp. 89, 94).

[119] A. Arani et al. "Measuring the effects of aging and sex on regional brain stiffness with MR elastography in healthy older adults". In: *NeuroImage* 111 (2015), pp. 59–64. ISSN: 1095-9572. DOI: 10.1016/j.neuroimage.2015.02.016 (cit. on p. 97).

[120] J. Bindl et al. "Using a controlled acceleration of the head to access viscoelastic properties of brain tissue". In: *Proceedings of the Fourteenth International Tissue Elasticity Conference*. 2015, p. 055 (cit. on p. 99).

Acknowledgment

"Manchmal erlischt in uns das Feuer und wird erst durch einen Funken, der von einem anderen Menschen auf uns überspringt, wieder entfacht. Jeder von uns sollte mit größter Dankbarkeit derer gedenken, die die Flamme in uns neu entzündet haben."

— Albert Schweitzer

Eine Dissertation zu verfassen ist kein Prozess, der in einem Vakuum stattfindet. Viele Menschen haben ihren Anteil zum Gelingen dieses Projektes beigetragen - sei es in wissenschaftlicher oder organisatorischer Hinsicht oder indem sie in mir erneut die Flamme der Neugier und Motivation entzündet haben, wenn diese einmal erloschen war. Aus diesem Grund möchte ich an dieser Stelle folgenden Menschen danken:

An erster Stelle danke ich meinen Beteuern Herrn Prof. Dr. Carsten Urbach und Herrn Prof. Dr. Karl Maier, die es mir ermöglicht haben auf diesem spannenden und vielseitigen Projekt zu promovieren.

Herr Urbach hat mich durch fruchtbare Diskussionen und kritische Fragen immer wieder auf neue Ansätze gebracht, mir aber auch viel Freiheit zur selbständigen Forschung gegeben. Außerdem hat er unter anderem mit seiner Begeisterung für den Roman "Berlin Alexanderplatz" auch dazu beigetragen meinen kulturellen Horizont zu erweitern. Herrn Maier danke ich für seine ungebremste Begeisterung zu forschen und zu lehren, an der ich immer wieder teilhaben durfte. Auch abseits der Physik habe ich viel von ihm lernen können - zum Beispiel wie man gute 20 Portionen echter schwäbischer Käsespätzle zubereitet.

Frau PD Dr. Elisabeth Soergel danke ich für ihre Mitwirkung als fachnahes Mitglied der Prüfungskommission, ihren motivierenden Einsatz und Zuspruch sowie für die gute Zusammenarbeit in der Lehre.

Herrn Prof. Dr. Arne Lützen danke ich für seine freundliche Bereitschaft in der Prüfungskommission als fachfremdes Mitglied mitzuwirken.

Herrn Prof. Dr. Klaus Lehnertz danke ich für die Organisation des Forschungsseminars und die vielen lehrreichen Diskussionen sowie dafür, dass er in seinen Vertiefungsvorlesungen für mich die Tür zur Medizinphysik aufgestoßen hat.

Herrn Prof. Dr. Bernd Weber und dem gesamten Life & Brain-Team - insbesondere Herrn Bartling, Herrn Becker, Frau Broicher, Frau Mahlow, Frau Schinabeck und Herrn Dr. Trautner - danke ich für das Ermöglichen der Messzeiten am MRT, die praktischen Hilfestellungen bei der Organisation und beim Bedienen des Scanners sowie die netten Gespräche während den Messzeit.

Den Personen, die sich freundlicherweise als Probanden zur Verfügung gestellt haben und die hier aus Datenschutzgründen anonym bleiben, danke ich für ihre Bereitschaft, an diesem Experiment teilzunehmen um meine Arbeit zu unterstützen, ihre Geduld während der Messungen und für ihre Neugier.

Dr. Jürgen Finsterbusch vom UKE in Hamburg danke ich für die Bereitstellung und mehrfachen Verbesserungen der Sequenz und den tollen Support, sei es aus Hamburg oder auch schon mal aus dem fernen Bhutan.

Der Bonn-Cologne Graduate School for Physics and Astronomy danke ich für die finanzielle Unterstützung, die es mir ermöglicht hat, an lehrreichen und interessanten Konferenzen teilzunehmen.

Ich bedanke mich auch bei den Mitarbeitern des HISKPs. Den Mitarbeitern der Feinmechanik-Werkstatt danke ich für ihre Unterstützung beim Bau der Versuchsapparatur und bei der Herstellung der Phantombehälter. Besonders Herr Eichler und Herr Klaes standen auch immer für kurzfristige Fragen zur Verfügung, aber auch wenn ich nur auf der Suche nach den passenden Schrauben war. Ebenso danke ich Herrn D'Hein, Herrn Kerp und Herrn Wolf vom Elektronik-Labor für ihre schnelle Hilfe bei elektronischen Fragestellungen jeder Art, sowie allen Mitarbeitern des Zyklotrons, die man immer ansprechen konnte, wenn man z.B. auf der Suche nach Pneumatik-Bauteilen war.

Unseren langjährigen Labornachbarn vom Isotopenseparator Albert Dahl, Siegfried Hinderlich und Cornelia Noll danke ich für die schöne Zeit und ihre Hilfsbereitschaft, besonders Conny für das Bereitstellen der Präzisionswaage. Unserem neuen Labornachbarn Marius Arenz danke ich für die freundliche Aufnahme in seinem kleinen Reich.

Den Mitarbeitern und Mitarbeiterinnen in der Verwaltung des HISKPs, Frau Anderson, Frau Balci, Frau Kehr, Frau Kraus, Frau Paus, Herrn Peithmann und Frau Ruland danke ich für ihre freundlich Art und die Unterstützung be organisatorischen Problemen verschiedenster Art. Vielen Dank auch an unseren Hausmeister Herrn Leiendecker.

Michael Kortmann vom Wolfgang-Paul-Hörsaal, den ich durch die von ihm und Prof. Dr. Herbi Dreiner geleitete - und für mich als Studentin sehr motivierende, lehrreiche und lustige - Physikshow kennen lernen durfte, danke ich für seine Bereitschaft schnell und unkompliziert Gerätschaften auszuleihen, von denen man denkt, "die könnte doch der Micha in der Sammlung haben".

Allen aktuellen und ehemaligen Mitgliedern der Arbeitsgruppe und den Kollegen aus den Nachbarbüros danke ich für eine unvergessliche Arbeitsatmosphäre und die schönen Stunden, die wir neben der Arbeit mit angeregten Diskussionen, Tagungen, historischen Symposien, Quizzen, Sonne-vor-dem-Institut-Genießen, Ausflügen oder Kuchen-Essen verbracht haben. Sie haben immer wieder Funken auf mich überspringen lassen.

Insbesondere danke ich allen Mitstreitern der MR-Projekte Deniz, Jakob, Judith, Sebastian, Alexandra, Birgit, Björn, Simon, Saskia, Steffi, Sylvia, Timo, Elisabeth,

Hanna, Johanna, Julius, Lino, Max, Niko, Roberto, Simon, Stephan und Herrn Habenstein. Mit vielen von ihnen habe ich mir unzählige Nächte beim Messen um die Ohren geschlagen und vor allem mit meinen Mitdoktoranden Deniz, Jakob, Judith und Sebastian habe ich viele fruchtbare fachliche Diskussionen führen dürfen.

Sebastian Theilenberg danke ich speziell für die Entwicklung und den Support der Auswertungssoftware (vor allem wenn noch schnell ein klitze-kleines Paket gebraucht wurde), die Hilfe bei Python, LaTeX und Ti*k*Z und die lange, kraftraubende, aber schlussendlich erfolgreiche Zusammenarbeit bei der Veröffentlichung des Papers. Ihm und Judith Wild danke ich auch herzlich für das Korrekturlesen dieser Arbeit.

Sylvia Napiletzki danke ich für die Anfertigung des Vakuumkissens, in das alle Probanden sicher verpackt wurden - ihre Nähkünste kamen genau zur richtigen Zeit.

Niels Räth danke ich für seine kompetente Arbeit als Netzwerkadministrator der Gruppe und dafür, dass er sich auch bei technischen Beratungen in allen anderen Bereichen immer viel Zeit genommen hat.

Einen wichtigen Beitrag zum guten Gruppenklima hat Frau Maier mit ihrer Herzlichkeit, Gastfreundschaft und fürstlicher Bewirtung geleistet - alles keine Selbstverständlichkeiten.

Während meines Studiums habe ich einige wundervolle Kommilitonen gehabt, die im Laufe der Jahre zu wichtigen Freunden geworden sind und mit denen ich gerne durch die schönen aber auch durch die anstrengen Zeiten gegangen bin. Ich danke Christian, Elke, Frank, Judith, Karsten, Kati, Max, Nicki, Simone, Stefan und Peter für eine tolle Zeit mit viel motivierendem Funkensprühen - nicht nur in der Physikshow. Judith danke ich besonders für die gemeinsame Zeit - von den ersten Vorlesungen, Übungen und Praktika über unser gemeinsames Abdriften in die Medizinphysik, wo ich bis heute nicht nur ein Büro, sondern auch viele Freuden und Sorgen mit ihr teilen darf.

Meiner Familie und Freunden danke ich für Begleitung und Aufmunterung, wenn es mal schwierig wurde. Meinen Eltern danke ich, dass sie mich bedingungslos unterstützen und lieben. Bei meinem Bruder Daniel bedanke ich mich dafür, dass er mir mit seiner eigenen Promotion ein Ansporn und Weggenosse am Familientisch war und ich mit ihm so leidenschaftlich über Wissenschaft diskutieren kann - sei es Ernährungssoziologie oder Physik.

Zu guter Letzt bedanke ich mich bei meinem Mann und besten Freund Peter, der mich in den vergangen Jahren mit unglaublicher Geduld, Liebe und Vertrauen unterstützt hat. Mit der Verlockung von vielen leckeren Abendessen hat er dafür gesorgt, dass ich nicht zu viele Nächte gearbeitet habe. Aber beim Essen konnten wir auch manchmal über physikalische Probleme diskutieren, was für mich ein Privileg war. Ich freue mich auf viele weitere gemeinsame Abenteuer und Herausforderungen, ruhige Stunden und Momente voller Lachen mit dir.